Algorithms for Next Generation Coherent Optical Networks

Thesis

Presented in Partial Fulfillment of the Requirements for the Degree of Doctor of Philosophy

Graduate Department of Electrical and Computer Engineering

University of Ottawa

by

Ahmad Abdo

Notation and abbreviations

ACPR	Adjacent Channel Power Ratio
ADC	Analogue to digital convertor
ASE	Amplified spontaneous emission
ASIC	Application specific integrated circuit
AWGN	Additive white Gaussian noise
AWG	Arrayed waveguide grating
BER	Bit error rate
CD	Chromatic dispersion
CMA	Constant modulus algorithm
CMOS	Complementary metal-oxide-semiconductor
DAC	Digital to Analog Converter
DBP	Digital backpropagation
DD	Decision directed
DFB	Distributed feedback
DGD	Differential group delay
DP	Dual polarization
DSP	Digital signal processing
DNL	Differential non-linearity
EDFA	Erbium doped fibre amplifier
EM	Electro-magnetic
FEC	Forward error correction
FIR	Finite impulse response

GBaud	Giga baud
GbE	Gigabit Ethernet
GVD	Group velocity dispersion
INL	Integral non-linearity
IM-DD	Intensity modulation-direct detection
ISI	Inter-symbol interference
LMS	Least mean squares
LO	Local oscillator
LUT	Look-up table
MMA	Multi-Modulus Algorithm
MC	Media Channel
ML	Maximum likelihood
MSE	Mean square error
MZM	Mach-Zehnder modulator
NMC	Network Media Channel
NLSE	Non-linear Schrodinger equation
NRZ	Non-return to zero
OPGW	OPtical ground wire
OSNR	Optical signal to noise ratio
PDM	Polarization division multiplexed
PDL	Polarization dependent loss
PLL	Phase locked loop
PI	Phase Interpolator
PMD	Polarization mode dispersion

PSK	Phase shift keying
QAM	Quadrature amplitude modulation
QPSK	Quadrature phase shift keying
ROADM	Reconfigurable Optical Add Drop Multiplexer
ROSNR	Required-Optical Signal to Noise Ratio
RLS	Recursive least squares
Rx	Receiver
RZ	Return-to-zero
SE	Spectral efficiency
SerDes	Serializer De-serializer
SNR	Signal-to-noise ratio
SOP	State of Polarization
SiPh	Silicon Photonics
SPM	Self-Phase Modulation
SSFM	Split-Step Frequency Method
Tx	Transmitter
WDM	Wavelength division multiplexing
WSS	Wavelength Selective Switch
XPM	Cross Phase Modulation

Abstract

With the technological shift towards big data, internet of things (IoT), 5G applications and cloud computing, the demand for high capacity networks is dramatically increasing. To avoid congestion and saturation, content and service providers are re-designing their network (backbone, metro and data-centers interconnects) connectivity using gridless optical line systems along with programmable coherent transponders. The latter are expected to transmit data at different data rates up to 400 Gb/s. In 2008, the first coherent receiver was commercially available [1]. By means of high-speed analog to digital converters and adaptive digital signal processing (DSP) algorithms, such revolution in modern optical communication was possible. That allowed a better spectral efficiency using higher order modulation formats and further signal reach by means of compensating both linear and nonlinear impairments. Another key development was leveraging light polarization-diversity, that permits to double the data rate at the expense of receiver complexity. To further increase the capacity of fiber links, gridless DWDM networks are being developed for deployment in the next few years. The key idea is to allow variable bandwidth signals to be allocated on optical links and by performing the appropriate network layer optimization improved throughput can be achieved. These innovations are driving new types of challenges for routing and assignment methods, as well, DSP algorithms such as clock recovery and compensation of fiber non-linearity.

This thesis is organized as a collection of contributions and composed of five major parts. The first part, consisting of chapters 2 and 3. Chapter 4 deals with tracking of fast state of polarization transient, i.e. dynamic aspect of optical channels, in presence of polarization dependent loss (PDL) and filtering effects due to reconfigurable optical add-drop multiplexers (ROADMs). Chapters 5 and 6 study the impact of filtering effects, quasi-static effects in optical links and transponders, represented by ROADMs in fixed-grid and Silicon Photonics (SiPh) modulators in flexible-grid networks, respectively. Chapters 7, 8 and 9, are related to clock recovery in digital coherent receivers. They cover mitigation of jitter in gridless applications, improving jitter when deploying phase interpolators (PI) and jitter injection as a test-mean to evaluate performance.

We start with introduction to the area of optical links and the coherent transponders. This part is intended to address a wide audience by mean of gathering of information and representative figures. We provide a quick tour of the history of fiber optics communication and the current/future

trends. Then we discuss the propagation of light, along with the associated linear and non-linear impairments. We focused on the impairments that we will be dealing with in our algorithms and methods. The concept of coherent detection covering the optical front-end, then analog/digital signal processing components all the way to the Forward Error Correction (FEC) block are all introduced.

In chapter 4, we analyze the performance of adaptive filtering in the context of dual-polarization coherent optical software-defined transceivers. We investigate the ability of different adaptive algorithms to track fast state-of-polarization (SOP) transients in the presence of colored noise. Colored noise exists due to the concatenation of Wavelength Selective Switches (WSSs) and polarization dependent loss (PDL) which can be considered as spatially-dependent noise. We consider the use of different modulation formats and the practical limitation of error signal feedback delay in decision directed adaptive filters is also taken into account. The back-to-back required signal to noise ratio (RSNR) penalty that can be tolerated determines the maximum SOP rate of change that can be tracked by the adaptive filters as well as the filter's adaptive step-size. We show that the recursive least squares algorithm, using the covariance matrix as an aggressive "step size" has a much better convergence speed compared to the least mean squares (LMS), normalized LMS (NLMS) and multi-modulus (MMA) algorithms in the presence of colored noise in the fiber. However, the three algorithms have similar tracking capabilities in the absence of colored noise.

In chapter 5, we are proposing an adaptive joint pre- and post- compensation to correct the filtering effects caused by cascading optical reconfigurable optical add drop multiplexers (ROADMs). The improvement is achieved without using additional hardware (HW) on the link or within the signal processor in the transponders. Using Monte Carlo simulations, the gradient-descent based method provided an improvement of 0.6 dB and 0.3 dB in required optical signal-to-noise ratio (ROSNR) versus post-compensation only and pre-compensation only respectively. We experimentally verified the method with lab measurements in presence of heavy filtering and optical impairments. We observed a gain of 0.15 dB and up to 0.4 dB compared to pre-compensation only and post-compensation only, respectively.

In chapter 6, we study the impact of bandwidth loss of silicon photonics (SiPh) modulators in coherent receivers. We propose a new approach to compensate for the steep roll-off in frequency response. We show that our proposed minimum mean-square error gradient-descent based

method provides 0.5 dB of ROSNR reduction for 60GHz channel when decay of modulator TF is 6 dB at 30 GHz. We present system benefits of not doing full pre-compensation at the Tx signal processor on the design of coherent transponders. As well, we show that when squeezing channels in gridless networks, using joint compensation provides a reduction of 0.1 dB to the probe channel when squeezing both neighbors by 2 GHz.

Allowing for tight channel spacing in gridless networks is an important issue to be tackled in future DWDM (dense wavelength division multiplexing) links. In chapter 7, we propose and experimentally study a new methodology and system to optimize the spacing between optical channels, using excess bandwidth as a mean to extract clock information, in gridless networks. By improving the mitigation of jitter of high-speed optical transponders, the method will exploit spectral efficiency by enabling the channels to operate on super-Nyquist DWDM (dense wavelength division multiplexing). We are describing a new clock recovery scheme, as an example, allowing decoupling the contribution of high-jitter noise sources from the clock recovery loop and an algorithm to optimize clock recovery settings to gain up to 2 GHz in spacing per pair of channels in the Media Channel (MC). The latter is defined in International Telecommunication Union (ITU) standard as a form of super-channel that includes sub-channels propagating from same node to same destination in an optical link.

In chapter 8, we propose a novel circuit and technique to measure and pre-compensate for the differential and integral non-linearities (DNL and INL) of phase interpolators (PI). Laboratory experiment shows that the solution enabled a reduction in system total jitter.

Finally, in chapter 9, we present a novel low-power circuit built into wireline transceivers that can be used in characterizing both modems and channels. The novelty is in properly controlling a phase interpolator in the transmitter clock recovery circuity which allows for jitter generation/injection. At the receiver side, we make use of existing clock recovery circuit to report statistics on measured jitter. Although generic and can be applied to any wireline transceivers, the method and circuit were prototyped and tested in a high-speed optical modem.

Acknowledgments

My sincere gratitude for my supervisor Dr. D'Amours for his precious feedback, accommodation and support. It was a long journey and Dr. D'Amours was always committed to explore new ideas, provide technical and non-technical guidance, as well discuss the analogy between optical and wireless modems.

A cluster of thank-you goes to Naim Ben-Hamida, Charles Laperle and Kim Roberts for investing the time to review this work so it is filtered properly to comply with Ciena' policies and protection of Intellectual Properties. As well, thank you for allowing this work to happen by allowing the use the labs and facilities in the evenings and weekends.

I would like to express my gratitude to the members of my examination committee Dr. Voicu Groza, Dr. Ian Masrland, Dr. Leslie Rusch, Dr. Melike Erol-Kantarci and Dr. Hussein Mouftah for accepting to review this thesis and providing valuable feedbacks.

Another sincere thank you to my mother, my brother, my sister, my nieces and nephews and to my late father for the love and support.

A special thank you to my in-laws for the support, especially helping with the kids while I am debugging the simulators, running tests over the weekend or typing these chapters.

To my wife, my main man Mohamad and little angel Khadija… thank you for your patience and endless love. From now on, God permits, I will have more time to do puzzles.

Contents

List of figures

List of tables

Chapter 1 – Introduction

"All our knowledge begins with the senses, proceeds then to the understanding, and ends with reason. There is nothing higher than reason." — Immanual Kant

1.1 - A Bit of History

Most data traffic in present-day networks is carried by means of optical electromagnetic (EM) fields. As demand for more communication channels increased with time, researchers had to consider two fundamental quantities, the attenuation and the maximum bandwidth of the transmission median. The first governs the SNR; hence the reach of the EM field and the bandwidth outlines the bit rates of data transmission. Using coaxial cables and waveguides, researchers could consistently increase the frequency of the carrier until they hit fundamental limits. Kao and Hockham, proposed using optical fiber as mean to transmit light allowing THz of bandwidth [4]. Using total internal reflection by covering the core by a cladding of different refractive index ($n_{cladding}$ slightly lower than n_{core}) [5], most of the EM field energy is preserved. The high loss of glass due to impurity was the main issue till early 1970s, when fused silica started to operate at 4dB/km at Corning. Another important component that helped in the evolution is the laser, which provides a line-width limited source to transmit data. By the end of the 70s, a loss of 0.2 dB/km was available around 1550 nm. However, due to the need to use repeaters every 50 km, the cost of lightwave systems were high and their bit-rate was limited. In 1987 [6], optically pumped erbium doped fiber amplifier (EDFA) was introduced. The high gain and bandwidth, along with low noise figure, allowed the use of multiple-channels on same link and the concept of Wavelength-Division Multiplexing (WDM, or FDM in wireless terms) was feasible.

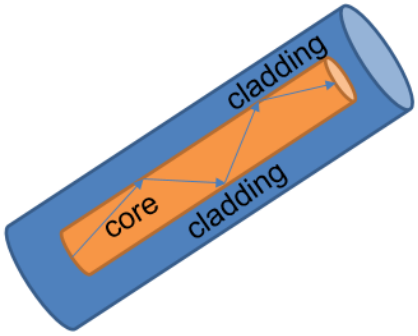

Figure 1: Structure of fiber and total reflection

Until 2005 [3], the transponders were based on Intensity-Modulated Direct Detection (IMDD),

where signaling between transmitter and receiver is based on the ON (1) /OFF (0) concept. The intensity of the light detected using photodiodes determines the bit of information sent.

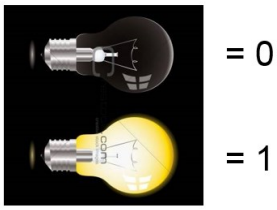

Figure 2: Illustration of IMDD

As laser and electronics technologies matured, allowing the mixing of incoming signal with small line-width laser and implementation of high-speed digital signal processing blocks, coherent receiver research was brought back to life. It permitted the increase of bit rate since the amplitude, phase and polarization are preserved. The three dimensions are made available for electronics to post-process the sampled EM. Another advantage for coherent detection is when mixing the incoming signal with the local oscillator (LO), as we will see in detail in chapter 3, we are amplifying the signal and hence decreasing the receiver sensitivity. Coherent transponders that are programmable, similar to software defined radio, operate at 50Gb/s in submarine cables, 100 Gb/s in long-haul, and 200Gb/s in metro networks are commercially available.

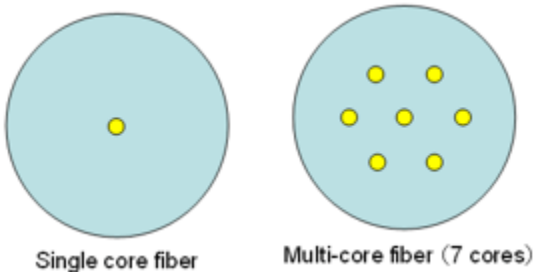

Figure 3: Single Core versus Multi-Core Fibers

To cope with the demand for more bandwidth [1], among research work investigates spatial division multiplexing using either multi-core fiber (Fig. 3) or few modes fiber (larger core compared to single core fiber). Although the after-mentioned methods are still a potential for future deployments, the current infrastructure of buried fibers are mostly single-mode and costly to replace. In the near future, the following aspects are being extensively looked at [2]:

- Increasing the baud rate (along with increasing the clock rate of signal processing)
- Transmitting data using higher order modulation formats.
- Reducing spacing by building super-channels.
- Compensating for nonlinear impairments (especially for Submarine and Long-haul links).

- More efficient network planning using gridless Wavelength Selective Switches (WSSs).

1.2 – Contents, Statement of Problems and Contributions

The next two chapters, 2 and 3, are an overview of fiber physical impairments and how they are compensated for in digital signal processing electronics with coherent receivers. The remaining chapters form the contributions of this thesis, where each chapter is aimed to study a specific challenge in current and future deployments of optical transceivers.

Chapter 4 covers the tracking of fast changes in the state-of-polarization (SOP), along with other link impairments, where practical limitations in hardware design are considered. This subject is currently a "hot-topic" with more content and internet providers depending on aerial fiber links to speed-up establishment of new services. Published works and available literature don't cover the following challenges:

- Comparison of various filters adaptation algorithms.

- Performance in the context of software-defined optical transceivers.

- Consideration of other link impairments, such as polarization-dependent loss (PDL) and filtering effects, since any networks experiencing SOP transients would have the mentioned impairments. Especially that the total penalty due to all impairments combined is not a cumulative of the penalties of each impairment separately.

Therefore, our aim is to fill-up the gaps mentioned above. We study four adaptive filter algorithms while comparing them in the presence of linear impairments. We obtain our results from Monte-Carlo simulations, while presenting mathematical explanation of the variability in performance while further considering the available design trade-offs.

Chapter 5 deals with heavy filtering due to concatenated reconfigurable optical add drop multiplexers (ROADMs) and channel multiplexer/demultiplexer (CMD) in optical links, i.e fixed-grid networks. Published works focused on:

- Pre-compensation at the transmitter through the introduction of time-domain finite-impulse response (FIR) filtering. However, there is no mention of a methodology on how the channel

response is obtained.

- Using waveshaper, as part of spectral engineering or network planning, per link. Such solution means more loss in the link (insertion loss of new equipment should be compensated for by amplifications), higher cost for deployments, higher power consumption to power-up the waveshaper and higher maintenance cost.

We propose a novel method, based on well-defined mathematical modelling, to help reduce the required-optical signal to noise ratio (ROSNR) in presence of ROADMs. We show that with power limitation and noise at the transmitter (Tx), splitting the compensation between Tx and receiver (Rx), yields a better performance. We use the common response of the four adaptive filters at the receiver as a means to extract the static filtering effect of the channel.

Chapter 6 re-uses most of the same method introduced in chapter 5, however, we apply it to the steep loss in the frequency response of Silicon Photonics (SiPh) modulators. The focus of the work is for short-reach gridless networks applications. Available literature assumes full pre-compensation or applied discrete multi-tone, along with bit-loading techniques, to leverage all available bandwidth while maximizing capacity. We take a new approach where we study the impact of the SiPh modulators on ROSNR with and without compensation. We then look at splitting the compensation of the modulator' frequency response between Tx and Rx, and the benefit of such a method in gridless networks with tight spacings between channels.

As mentioned in the introduction, one method to cope with demands for more capacity in fiber link is to increase the baud-rate of transmitted signals. The main circuit impacted by such increase is clock recovery where the unit interval (symbol periods) is getting smaller compared to previous generations of coherent transponders and the sensitivity to jitter is higher. Hence, chapters 7, 8 and 9 are concerned with topics related to clock recovery in digital coherent receivers.

Chapter 7 demonstrates a circuit and method which allow to better mitigate jitter in coherent receivers that use excess bandwidth to extract clock phase error. The goal is to be able to reduce spacing between neighboring channels, to gain achieve higher spectral efficiency, in optical links based on gridless configuration. Therefore, when two channels are travelling together in the same media channel (MC), they impact each other through the leaked power from their edges (end of channel bandwidth). The issue is when the edge information, i.e. excess bandwidth, is used as a

mean to track jitter induced by both the transmitter and the channel. To the best of our knowledge, this is a unique approach. Related literature discussed using techniques to use fourth-power Gardner phase error estimate but still to operate at low roll-off factor of the pulse shaping and not to reduce spacing. The circuit and method are submitted as patent application and currently are under US government review.

Chapter 8 tackles the non-linearity issue of phase interpolators (PI). The latter are used as a mean to adjust clocks phase when converting data from digital to analog. We present a novel, low cost and low power method that measures the PI non-linearity and uses only a look-up table (LUT) to perform the proper pre-compensation. To deal with the issue, Authors in published literature had to increase the granularity of the phase steps which requires a larger design foot-print, higher resolution digital control and an increase in power consumption. Our digital method makes the most of low-cost delay elements, accumulator and simple bang-bang binary phase detector.

Similar to chapter 8, chapter 9, deals with the testing aspect of coherent and, more generally, wireline transceivers. We introduce a new method to induce jitter tones in order to modulate clocks at digital to analog converter (DAC). The circuit is able to produce fine mis-alignments, in the order of femto-seconds, in the clock generating the digital samples. An associated method to automate the process of generating jitter mask for receiver' clock recovery circuity, while re-using existing signal processing blocks, is described as well.

1.3 – Associated Publications

Publication reviewed by Ciena technical and IP teams:

1. *Conference (published):* Abdo, A., D'Amours, C., "Performance of LMS Based Adaptive Filtering in Coherent Optical Receivers in Presence of State-of-Polarization Transients, PDL and ROADMs," Proc. IEEE Can. Conf. Elect. And Comp. Eng. (CCECE), May 2018.

2. *Conference (published):* Abdo, A., D'Amours, C., "Adaptive Pre-Compensation of ROADMs in Coherent Optical Transponders," Proc. IEEE Can. Conf. Elect. And Comp. Eng. (CCECE), May 2018.
3. *Conference (submitted):* Ahmad Abdo, Sadok Aouini, Naim Ben-Hamida and Claude D'Amours, "Circuit and Technique for Measuring and Compensating Phase Interpolator Non-Linearity", Custom Integrated Circuits Conference, May 2019

4. *Journal (submitted):* Ahmad Abdo, Claude D'Amours*, "*Adaptive Filtering in Optical Coherent Software Defined Receivers in the Presence of State-of-Polarization Transients and Colored Noise", Journal of Lightwave Technology, (JTL - 22944-2018)

5. *Journal (in prep):* Ahmad Abdo, Claude D'Amours, "Adaptive Pre/Post-Compensation of ROADMs in Coherent Optical Transponders", Photonics Technology Letters.

6. *Journal (under review by Ciena publication*): Ahmad Abdo, Sadok Aouini, Naim Ben-Hamida and Claude D'Amours, "Jitter Loading Built-In Circuit and Method to Characterize Optical Transceivers and Channels", IEEE Transactions on Circuits and Systems-||

7. *Patent - defensive disclosure (published):* "Characterizing optical fiber channels for jitter and polarization state via optical transceivers", IPCOM000253714D

8. *Patent (published - under government review):* "Clock recovery circuits, systems and implementation for increased optical channel density".

9. *Conference (in-prep for submission):* Ahmad Abdo, Claude D'Amours and David Plant, "System Study of Silicon Photonic Modulator in Short Reach Gridless Coherent Networks", CLEO, 2019.

Chapter 2 – Fiber Optics Channels

"Everything has its tax and the tax of knowledge is to teach people." — Imam Ja'far al-Sadiq (AS)

2.1 - Light Propagation

The Nonlinear Schrodinger equation (NLSE), described in [7] and [11], governs the propagation of the electrical field as a function of time and distance when attenuation, chromatic dispersion and Kerr nonlinearities are present:

$$\frac{\partial E}{\partial z} + \frac{j\beta_2}{2}\frac{\partial^2 E}{\partial t^2} + \frac{\alpha}{2}E = j\,\gamma\,|E|^2\,E \qquad (2.1)$$

Where *E*, function of time (t) and distance (z), is the electric field, α is the attenuation coefficient (loss in dB/km), β_2 is the dispersion parameter, γ is the nonlinear coefficient. *E* is EM wave propagating in nonlinear dispersive media. Therefore, NLSE is derived using Maxwells equations assuming single-mode fiber (SMF).

To double the data rate, propagating with two polarizations as shown in figure below, was introduced in coherent receivers. Signal for each polarization is generated separately then orthogonally merged, using polarization beam combiner, at the output of the transmitter. The impairments and complexity associated with this feature will be discussed in details later on.

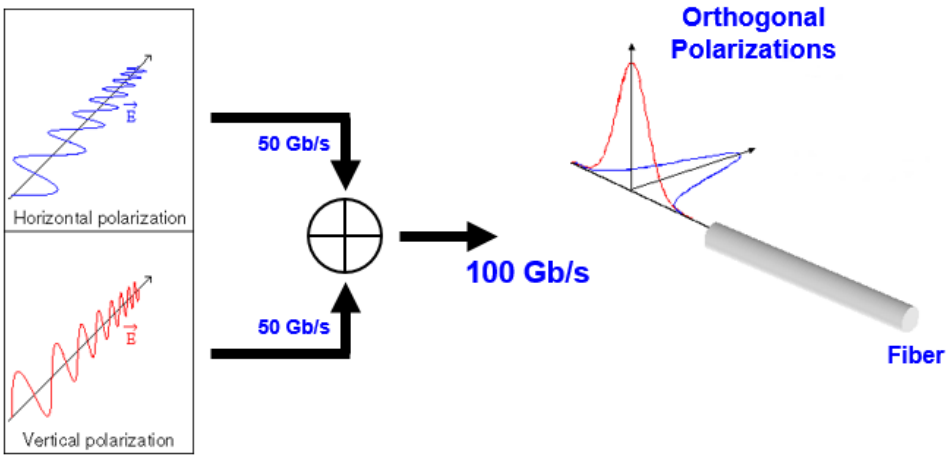

Figure 4: Single and Dual Polarization Signals in 100Gb/s system

Then equation above can be extended as follow, [9], to cover the interactions between the two polarizations:

$$\frac{\partial|E_x\rangle}{\partial z} = -\frac{\alpha}{2}|E_x\rangle - \frac{i\beta_2}{2}\frac{\partial^2|E_x\rangle}{\partial t^2} + i\gamma\frac{8}{9}\left[|E_x|^2 + |E_y|^2\right]|E_x\rangle \quad (2.2)$$

$$\frac{\partial|E_y\rangle}{\partial z} = -\frac{\alpha}{2}|E_y\rangle - \frac{i\beta_2}{2}\frac{\partial^2|E_y\rangle}{\partial t^2} + i\gamma\frac{8}{9}\left[|E_x|^2 + |E_y|^2\right]|E_y\rangle \quad (2.3)$$

2.2 - Optical versus Wireless Channels

A comparison between optical and wireless channels is helpful to pave the way for common ground and ease the digestion of some optical channel related concepts. As presented in the table below, most of the input are adopted from [10], optical and wireless channels are quite unique. Each has its own challenges both in term of speed of the variability and main impairments that should be compensated. We will elaborate on this in chapter 3 when we present the attributes of the transponders.

Impairment	Optical	Wireless
Dispersion	• Chromatic Dispersion • Polarization-Dependent Dispersion	Multi-path propagation
Noise	ASE and shot noise	Thermal Noise
Source of channel variation	Fiber motion	Terminal Motion
Scale of time-varying channel	10 to 100s of µs	1 ms
Fading	• Fiber Attenuation • In MMF, Mode-Dependent optical amplifier gain	Multi-path propagation
Interference	• Inter-Channel CrossTalk (linear) • Inter-Channel interference (nonlinear cross-phase modulation) • Intra-Channel interference (nonlinear self-phase modulation)	Inter-Channel CrossTalk (linear)
Attentuation in MIMO modes	Polarization-Dependent Loss (can be up to 10 dB in long-haul)	Large in case of Rayleigh effect

Table 1: Comparison Between Optical and Wireless Channels

2.3 - DWDM

As laser technology advances, we can divide the available bandwidth in the low loss spectrum of the fiber into frequency bins and modulate data independently –even with different data rate- in each bin. By having multiple carriers in optical domain and simultaneously transmitting them into a fiber, DWDM systems came into existence. A key element in nowadays flexible DWDM optical networks, the ROADMs (built using Micro-Electro-Mechanical Systems), introduce both loss and frequency dependent noise. Nowadays deployments are based on fixed-grid 50GHz spacing defined by ITU G.694.1 standard.

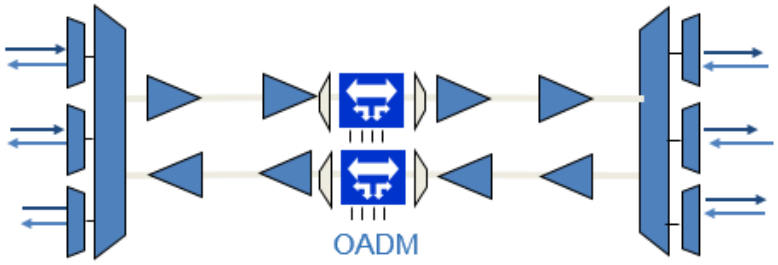

Figure 5: A typical DWDM network with multi-span

In gridless networks, that are being designed to reduce spacing between wavelengths, individual channels are not filtered separately; therefore, the effects of leaked power from neighboring channels (cross-talk) on system performance is a major research topic to be tackled.

2.4 – Attenuation & Noise

It is a necessary condition that the modulated light in fiber optics to reach the other end with power higher than the sensitivity of the receiver. Attenuation is due to multiple reasons, such as partial absorption, impurity of Silica and scattering. The typical attenuation in optical links is 0.2 dB/km. On top of propagation loss, connectors, patch cables, input channel multiplexers, and other passive components required to establish the connectivity have insertion loss. The propagation loss is wavelength dependent; based on the figure below, the so-called C-Band window has the lowest attenuation.

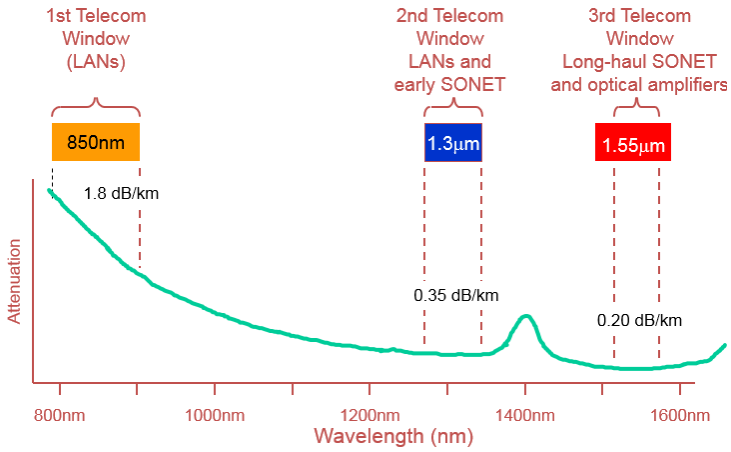

Figure 6: Attenuation in different optical windows

Loss is typically modelled as follow, with α in dB/km:

$$P_{out} = exp^{(-\alpha * L)} * P_{in} \quad (2.4)$$

To overcome the total attenuation, without converting signals back to electrical domain and the use expensive repeaters, EDFA and Raman amplifiers are an integral part of optical links. Amplifiers gain can reach 25 dB and they are installed at the end of a span of fiber of around 80-100 km. As part of the process, spontaneous photons are released and they are not stimulated by signal photons. That is called Amplified Spontaneous Emission (ASE) and it is characterized as AWGN noise source when studying fiber models. As in any complex system, there are many sources of noise. The second dominant one, after ASE, is the local oscillator shot noise.

We will be using both terms SNR and optical-SNR (OSNR). Here are the definitions, with P representing Power:

$$OSNR = \frac{P_{sig,BW}}{P_{noise,12.5GHz}} \quad (2.5)$$

$$SNR = \frac{P_{sig,BW}}{P_{noise,BW}} \quad (2.6)$$

$$OSNR_{BW/0.1} = 10\log_{10}(BW/12.5) + SNR \quad (\text{dB scale}) \qquad (2.7)$$

2.5 - Linear Impairments

2.5.1 - Chromatic Dispersion (CD)

Different colors traveling in a fiber have different velocities. Since a time-domain spreading of the transmitted signal occurs. It is the sum of two dispersion types:

- Material dispersion
- Waveguide dispersion

Before introducing complex DSP functionality, mainly high resolution DAC/ADC, into optical transmitter design, dispersion was compensated optically inline. However, that was costly, requires high-maintenance with more amplifications and more susceptible to outages.

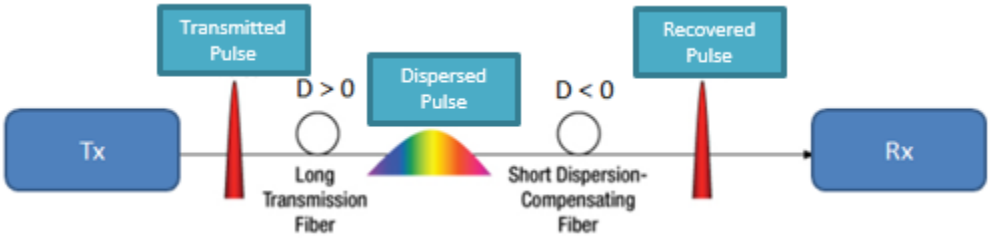

Figure 7: Dispersion effect and DCF (compensating it inline optically)

In frequency domain, dispersion is just a phase shift with unity amplitude [11]:

$$H(f) = exp^{(j*\frac{\pi*D*L*lambda^2}{c}*f^2)} \ldots (2.5)$$

Where, D = dispersion

C = Light speed

L = distance

Lambda = wavelength

As an example, the delay spread for a 1000 km SMF @25GBaud with D = 17 ps/nm*km is 7nsec, that is equivalent to 170 symbols. Below we show how a RRC pulse is broadening and interfering with neighboring symbols after propagation of 3 spans of 80 km each.

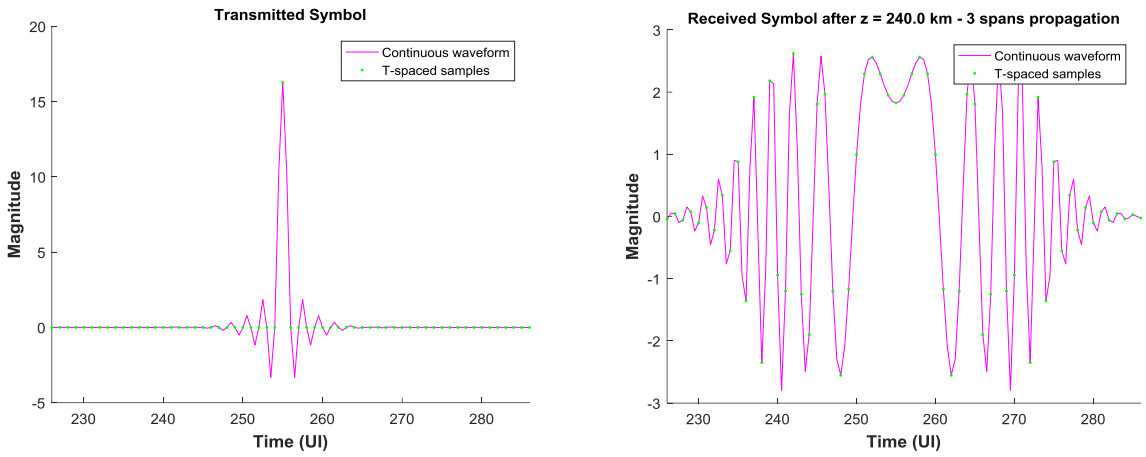

Figure 8: Pulse after Propagation in Dispersive Fiber

The inter-symbol interference above is translated to constellation points being mixed-up.Since it is a linear impairment (linear combination of symbols), so a finite impulse response (FIR) filter at the receiver -with sufficient number of taps – can correct for that without any penalty.

Another way to show input/output relationship, using frequency domain, is used later when solving non-linear **Schrödinger** equation (NLSE) numerically:

$$A_{out}(f) = A_{in}(f) * exp^{(j*2*\pi*\beta_2*(\Delta f^2))} \quad (2.6)$$

2.5.2 - Polarization Dependent Impairments

As mentioned, to increase the data rate by two, polarization diversity is a degree of freedom that is a standard in coherent receiver implementation. However, that creates a new set of challenges in single mode fiber which was not part of the IMDD receivers. Real-life manufacturing processes and deployments introduce internal and external imperfections, such as core stress, fiber bend, fiber twist and many others. That leads to a phenomenon called Birefringence in fiber [12], where the refractive index to change based on polarization state.

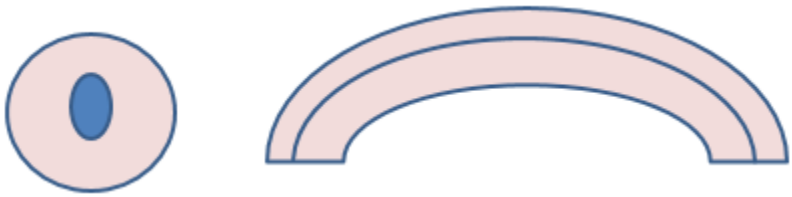

Figure 9: Illustration of Elliptical Core and Fiber Bend

2.5.2.1 – Polarization Mode Dispersion (PMD)

The PMD is another type of dispersion where the two polarizations are travelling at different speed and hence arriving at different time (Fig. 10). As we see in figure below, the total pulse –combining both polarizations- is broadened in time and at high data-rates, ISI becomes a major limitation. However, if the equalizer at the receiver has enough taps to handle the delay, PMD –similar to CD- can be compensated with no penalty. First order PMD can be modeled as follow:

$$H_{channel\ with\ PMD\ only} = \begin{bmatrix} \cos(\theta) & \sin(\theta) \\ -\sin(\theta) & \cos(\theta) \end{bmatrix} \begin{bmatrix} e^{j\varphi} & 0 \\ 0 & e^{-j\varphi} \end{bmatrix} \begin{bmatrix} \cos(\beta) & \sin(\beta) \\ -\sin(\beta) & \cos(\beta) \end{bmatrix} \quad (2.7)$$

2.5.2.2 – Polarization Dependent Loss (PDL)

PDL cause a loss that is polarization dependent. Fig. 10 illustrates both PDL and PMD.

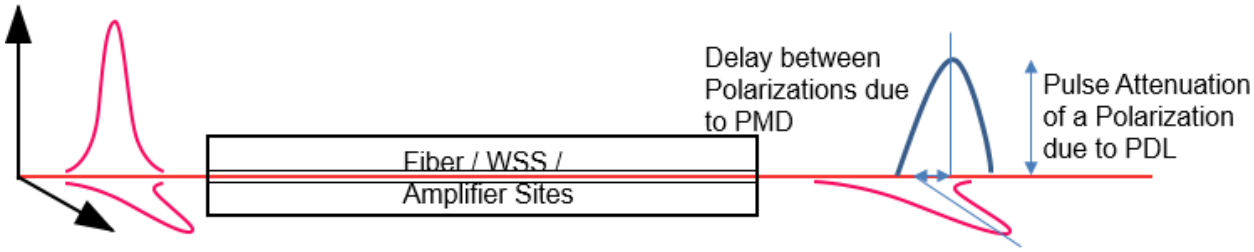

Figure 10: PMD and PDL Effects on PSP in Dual Polarization Optical Fiber Transmission

Mathematical representation of one PDL element in the fiber:

$$H_{channel\ with\ PDL\ only} = \begin{bmatrix} \cos(\theta) & \sin(\theta) \\ -\sin(\theta) & \cos(\theta) \end{bmatrix} \begin{bmatrix} 1 & 0 \\ 0 & k \end{bmatrix} \begin{bmatrix} \cos(\beta) & \sin(\beta) \\ -\sin(\beta) & \cos(\beta) \end{bmatrix} \quad (2.8)$$

Where k < 1. Since θ and β are changing randomly, the two polarizations are being mixed in a time-varying manner and it is up to adaptive filter at the receiver to track and compensate for the linear combination.

2.5.2.3 - States of Polarization

Another form of linear impairment is the combination or rotation of the two states of polarization. The general form is the Jones rotation matrix below:

$$H_{channel\ with\ Rotation\ only} = \begin{bmatrix} \cos\theta \cdot \exp(i\varphi) & \sin\theta \cdot \exp(i\phi) \\ -\sin\theta \cdot \exp(-i\phi) & \cos\theta \cdot \exp(-i\varphi) \end{bmatrix} = \begin{bmatrix} a & b \\ -b^* & a^* \end{bmatrix} \quad (2.9)$$

The Jones Vector represents the state of polarization using the complex Electric Field; while the Jones Matrix is the model of linear operations applied to the Jones Vector throughout transmission in fiber optics. The received signal on each of the polarizations is a linear combination of the two transmitted signals. Hence we can decouple the by using 2x2 MIMO FIR filter adapted to inverse Jones matrix of the fiber channel.

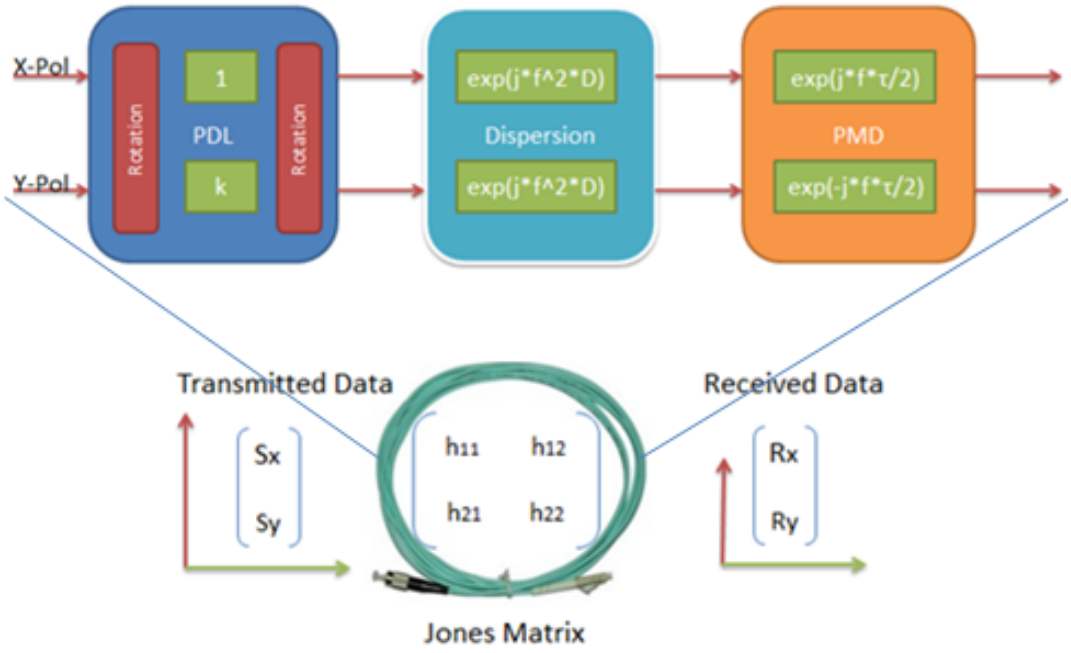

Figure 11: Dual-polarizations Fiber Model with only linear impairments

2.6 - Nonlinearity in Fiber Optics

What has been discussed in the Linear Impairments section, the properties of the fiber do not depend upon the signal. On the other hand, when the silica properties are altered by the energy of the signal itself, then that falls into a category of what is called "non-linear fiber optics". Because of nonlinearity, we can't increase the launch power (equivalently the signal to noise ratio) to allow further reach of optical signal; it is now the main limiting factor to reach Shannon Limit in optical fiber.

The non-linear effects, of interest, in optical fibers are the following [11]:

- *Intra-Channel* Self-Phase Modulation (SPM)
- Inter-Channel Cross-Phase Modulation (XPM)
- Inter-Channel Four Wave Mixing (FWM)

When the light intensity increases, the higher order susceptibility terms in the induced polarization of dielectric material must be taken into consideration. Kerr non-linearity is due to the third-order susceptibility. As the light enters fiber optics, it travels for long time. That causes an accumulation of non-linearity due to its continuous interaction with glass (SiO2).

$$n = n + n_2 \left(\frac{P}{A_{eff}}\right) \quad (2.10)$$

where n_2 is the nonlinear index coefficient = 2.6 x 10^(-20) m^2/W

n is the Silica refractive index

P is the optical power

A_{eff} is the fiber effective area.

For our interest, we will focus on SPM and XPM. The phase shift determined by nonlinearity has the form [11]:

$$A_{out}(t) = A_{in}(t) * exp^{(j * \gamma * L_{eff} * (P(t)))} \quad (2.11)$$

With $$\gamma = \frac{2 * \pi * n_2}{\lambda * A_{eff}}$$

Differential equation NLSE (eq. 2.1) is solved numerically with small number of steps to achieve solution of propagating optical pulse. Split-Step Fourier Method (SSFM) is a one of the popular ways to do so. It splits Schrodinger equation into linear (dispersion) and nonlinear parts. Then it solves the linear part in frequency domain (eq. 2.6) and nonlinear part (eq. 2.11) in time domain.

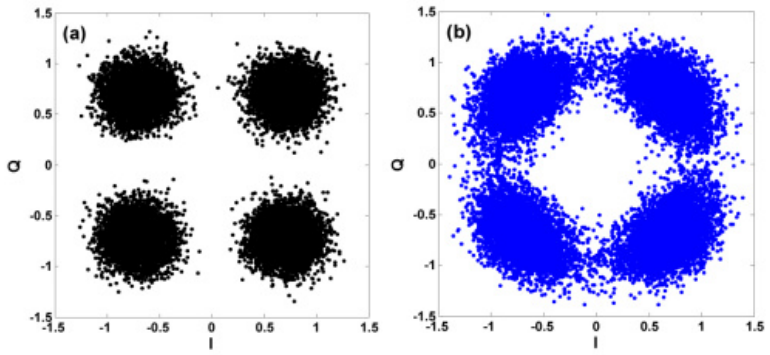

Figure 12: QPSK Constellation with: a) ASE only b) ASE and Phase Noise Impairment

2.7 - Link Budgeting

Monitoring and recording the impairments based on the information gathered by the channel equalizers, described in details next chapter, will help in network planning and spectrum assignment. The statistics of those impairments can be associated with OSNR impairment-*penalty*; therefore, for each route in a network, the operator (or automated planning software) will be able to, based on margin, reduce outages and FEC hits when choosing a route with:

$$\text{OSNR} = \text{Required-OSNR} + \text{impairment-penalty} + \text{end of life margin} \qquad (2.12)$$

Since FEC errors at the optical layer are propagated to all above layers, network operators optimize the OSNR to keep BER at the receiver far from FEC limit.

Chapter 3 - Signal Processing in Coherent Optical Transponders

"For man to be able to live he must either not see the infinite, or have such an explanation of the meaning of life as will connect the finite with the infinite." – Leo Tolstoy

3.1 - Introduction

Digital signal processing has been applied to radars, mobile telephones and digital television to compensate for low available bandwidth, and increase tolerance to noise. Since the early nineties, interest has grown in the use of electrical signal processing using equalization filters for the correction of ISI in high-speed optical communications [13], [14]. The work of adaptive equalization filters to compensate for deterministic distortion of the signal, along with Forward Error Correction (FEC) to protect against random noise, is at the core of the receivers' design. The availability of fast CMOS Integrated Circuits, featuring data converters and signal processing units, where the main drivers permitting the design of electronic chips capable of handling optical transmission. They allowed substantial improvement to linear optical transmission impairments tolerance. Signal processing techniques lend themselves to integration and mass production, and give a cost-effective method of increasing system lengths in a low cost optical communications system.

As previously mentioned, until 2005, the detection in optical transponders operation at 10G and below was based on direct detection of intensity with one polarization being modulated. Using photo-diodes detectors, made with Germanium for example, where free electronholes are generated by absorbed photons; such technique was simple and it has a by-design immunity to state of polarization. Since the phase of the modulated signal is lost during the detection, we could not support rich modulation formats. As well, we could not simply keep increasing the baud-rate (with one bit per symbol) by 10 to reach 100Gb/s, that is limited by the speed of the electronics and the resulting occupied bandwidth. However, by detecting the optical field i.e. the power level and the phase, using interferometric (or coherent) detection we can solve the problem and follow the trends of modems in wireless. When mixing the incoming optical signal with high-power local oscillator, the phase is preserved and the sensitivity of the receiver is decreased since the mixing operation is acting as amplification as well.

As shown in [15], [16], [17], [18], [19] and [20], new techniques are being developed every year to enable both submarine and data-center interconnect communications, while increasing the

capacity of existing fibers. In this chapter, we will look at how dual-polarization (DP-) coherent systems are recovering payloads.

3.2 - Optical versus Wireless Transponders

The complexity of optical transponders is governed by the symbol rates. Compared to wireless, the amount of parallelism required is significant. We will perform a quick table-based comparison with wireless modems. Most of these attributes were mentioned in [10].

Attribute	Optical	Wireless
Symbol rate	30 to 80 GBaud	10s of MBaud
Carrier frequency	185-196 THz	0.8 to 6 GHz
Dithering	Sensitive laser control	Terminal Motion
MIMO Interface	Dual-polarization in SMF Multi-mode in MMF	Multiple Antennas
ASIC Clock	100s MHz	100s MHz

Table 2: Comparison between attributes of optical and wireless transponders

It is worth noting that the demodulation, beyond converting the signal from analog to digital domain, is pretty much common among optical, wireless and DSL modems. As we will see in the Rx DSP section, all modems require clock recovery, adaptive filtering, decoder, estimation of carrier and FEC.

3.2 - Principle of Coherent Detection

3.2.1 - Tx Modulator

The key concept enabling optical coherent modulators, at the transmitter, is that we can slow down light when applying an electric field across its path. A carrier, or continuous wave signal generator, is being modulated. As we see in figure below, the electric field is built one dimension at the time.

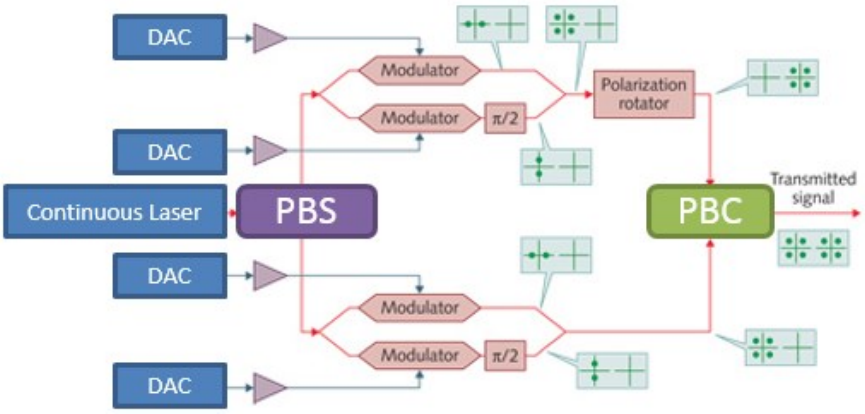

Figure 13: Modulator of coherent transmitter

The mathematical model of one arm is in the equation below, where V_1 and V_2 are the voltage driven by the Digital to Analog Converter (DAC). The interference will result in E_{out}, ranging from constructive when same phase in each arm to the destructive when π is the difference.

$$E_{out} = \frac{1}{2} * \left(e^{j*\frac{V_1}{V_\pi}*\pi} + e^{j*\frac{V_2}{V_\pi}*\pi} \right) * E_{in} \qquad (3.1)$$

As you can see, due to layout variability when building those optical modulators, a lot of issues will raise. To name few:

- I/Q delay on each of the polarization
- I/Q power imbalance
- X/Y delay
- X/Y power imbalance.

3.2.2 - Rx Optical Front-End

By mixing, with simple 50/50 3 dB coupler, the incoming modulated optical field with local oscillator field, then applying a balanced detector to get the electrical signal containing both phase and magnitude information:

$$E_{rx}(t) = \sqrt{P_{rx}} * e^{i*(w_{rx}.t + \phi_{rx}(t))} \qquad (3.2)$$

$$E_{LO}(t) = \sqrt{P_{LO}} * e^{i*(w_{LO}.t + \phi_{LO}(t))} \qquad (3.3)$$

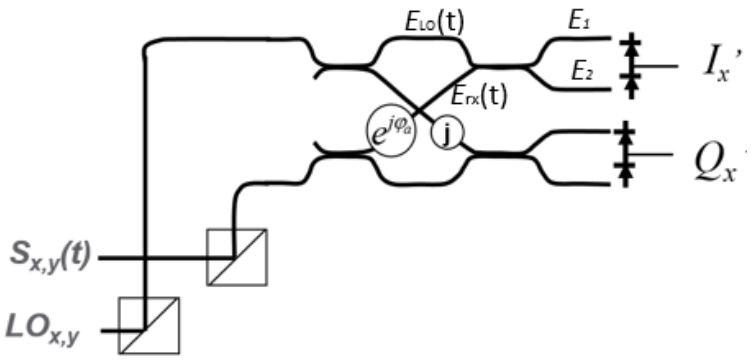

Figure 14: Simple Coherent Detection with Balanced Photo-Diodes

$$\begin{bmatrix} E_1 \\ E_2 \end{bmatrix} = \frac{1}{\sqrt{2}} \begin{bmatrix} 1 & 1 \\ 1 & -1 \end{bmatrix} \cdot \begin{bmatrix} E_{rx}(t) \\ E_{LO}(t) \end{bmatrix} \qquad (3.4)$$

$$E_1 = \frac{1}{\sqrt{2}} \left(E_{rx}(t) + E_{LO}(t)\right);\ E_2 = \frac{1}{\sqrt{2}} \left(E_{rx}(t) - E_{LO}(t)\right) \qquad (3.5)$$

$$I(t) = I_1(t) - I_2(t) = \left(R_1 * {E_1}^2 - R_2 * {E_2}^2\right) \qquad (3.6)$$

with R_1 and R_2 are the responsivity of the photodiodes.

With DC block, the current *I(t)* is a function proportional of both channel power and phase:

$$I \propto 2 * \sqrt{P_{rx} * P_{LO}} * \cos\left((w_{rx} - w_{LO}) + (\varphi_{rx} - \varphi_{LO})\right) \qquad (3.7)$$

We can add in-phase/quadrature and polarization diversity circuits to cover 4 elements per symbol as below:

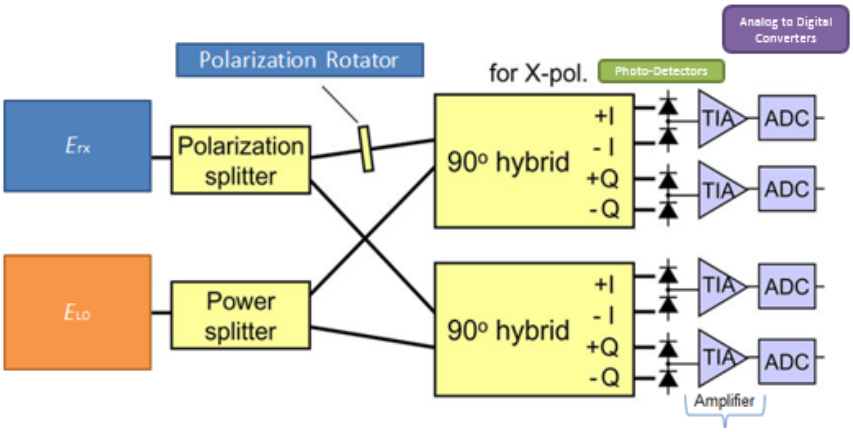

Figure 15: Complete Rx Coherent Detection with Pre-ADC Amplifiers

3.3 – Digital & Analog Signal Processing in Coherent Transponders

3.3.1 - ADC/DAC

The advances in high-speed parallel ADC/DAC architecture were a key enabler for allowing DSP to operate on optical signals. To fulfill Nyquist requirements, the sampling rate should be double the maximum frequency of the signal.

The DAC determines how much pre-shaping/pre-compensation of dispersion we are able to do. It is important to determine dynamic range of operation to avoid clipping.

The current commercial ADC are operating at the rate of the order of 56Gs/s and 6-bit ENOB [22]. The target Effective Number of Bits (ENOB) is based on the modulation format supported by the modem. It is necessary to keep the balance between the clipping and the quantization rates. Typically, Trans-Impendence Amplifier (TIA), as shown in figure above, with gain engineered to keep signal levels so the ADC can operates at full scale. The performance of ADC, typically sub-ADCs interleaved [21], depends on jitter untracked by a Phase Locked-Loop (PLL); that is especially at high frequencies. At low frequencies, quantization and thermal noise are the dominant factors.

$$\mathrm{SNR}_{\mathrm{ADC}}\left[\mathrm{dBc}\right] = -20\times\log\sqrt{\left(10^{-\frac{\mathrm{SNR}_{\mathrm{Quantization\ Noise}}}{20}}\right)^2+\left(10^{-\frac{\mathrm{SNR}_{\mathrm{Thermal\ Noise}}}{20}}\right)^2+\left(10^{-\frac{\mathrm{SNR}_{\mathrm{Jitter}}}{20}}\right)^2} \quad (3.8)$$

3.3.2 – Tx DSP

Tx is mainly responsible for encoding a bit stream coming from the data-link layer. That involves

scrambling, applying Forward Error Correction (FEC) overhead, mapping bits into constellation symbols (with gray encoding if applicable), arranging the symbols into packets and applying a "shape" to the pulse to minimize ISI. In figure below, we show a table with various supported modulation formats in nowadays commercial transponders:

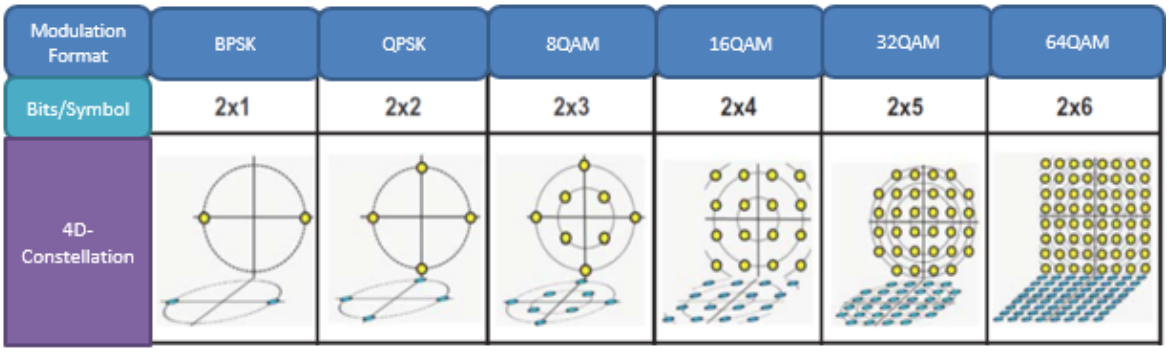

Figure 16: Various Dual-Polarization Constellations

Other important DSP blocks are typically found on the Tx side, such as:

1- Frequency or time domain filter that can be used for the following:

a. *Pulse Shaping*: to maximize SNR at the input of the receiver adaptive filter [23], it is typical to use root-raised cosine on the Tx, then matched with root-raised cosine at the Rx.

$$H(f)=\begin{cases}1 & \text{for}\,|f|<2W_0-W \\ \cos\left[\frac{\pi}{4}\frac{|f|+W-2W_0}{W-W_0}\right] & \text{for}\,2W_0-W<|f|<W \\ 0 & \text{for}\,|f|>W\end{cases} \quad (3.9)$$

with W_0-W is the excess bandwidth.

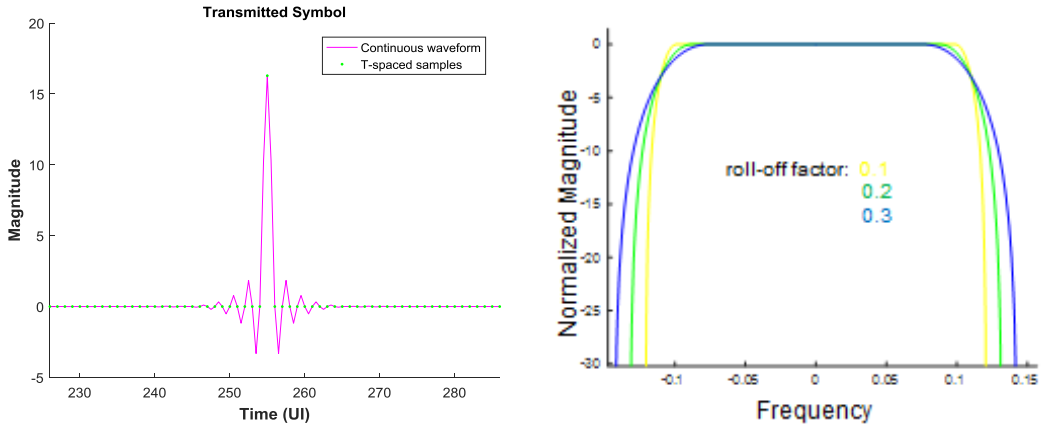

Figure 17: Time and Frequency Representation of a Root-Raised Cosine Pulse

b. Dispersion pre-compensation: It is shown in literature that dispersion pre-compensation can help enabling more dispersion tolerance at high-data rate, as well has the benefit when dealing with nonlinearity [24] in long-haul optical communication.

2- PDL Pre-compensation: PDL can be slightly mitigated using a polarization-scrambler, leading to an averaging over the performance of various equiprobable polarization-states. [25]

3- Nonlinearity: The authors in [26] showed a technique to use the transmitter for non-linear compensation of SPM.

3.3.3 - Rx DSP

Most of the processing, and heat consumption, is taking place at the receiver. Figure below shows the typical blocks used in coherent receivers right from the output of the ADC to the input of the decoder. We will discuss these blocks one by one, then give an overview of non-linear backpropagation and FEC.

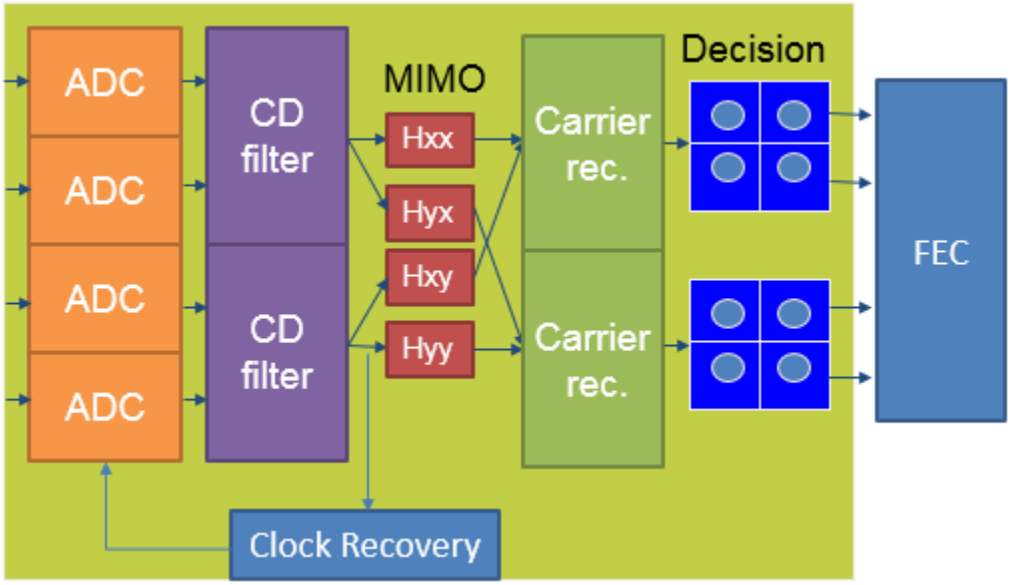

Figure 18: Typical DSP in Coherent Receivers

CD (Post) Compensation

Once data is digitized, the first action is typically to compensate for chromatic dispersion. For long-haul optical communication for example, the large accumulated chromatic dispersion causing one pulse to smear over hundreds of neighboring symbols, makes it impossible to do any

linear operation before compensating for the bulk part of it. The compensation usually occurs in frequency domain (FFTs and IFFTs are not shown here) by multiplying the Fourier representation of incoming burst with the following correction [27] [28] [29] [30]:

$$H^{-1}(f) = exp^{(-1*j*\frac{\pi*D*L*lambda^2}{c}*f^2)} \qquad (3.10)$$

Clock recovery

The second key block is clock recovery. Similar to wireless modems, the transmitter and receiver have different clocks. Therefore to sample received analog data at the right phase (and frequency), we need to track the jitter. The clock recovery circuits are built around a PD (Phase Detector), PLL (Phase Locked Loop) and various filtering/accumulators to equalize the sources of noise. Many methods are proposed in time-domain (Gardner [32]) or frequency domain (Godard [33]). Once PD outputs the phase error, the latter is used as input to a control loop driving a VCO.

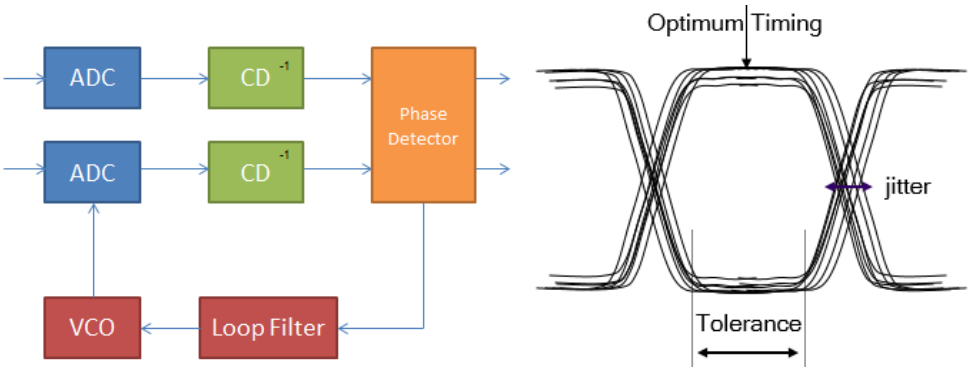

Figure 19: Clock recovery simplified circuit and eye diagram

Dynamic Butterfly MIMO

To decouple the two polarizations, we need a MIMO structure of 2x2 filters [34] [35]. For time-varying channel estimation, the choice between time or frequency domain implementation is usually based on the filter orders. For small number taps, time-domain convolution can be done without much complexity. For T/2 spaced equalization, the amount of PMD that can be mitigated is half the filter order. To handle large PMD, frequency domain is typically used. Adapting algorithms are such Least Mean Square and Recursive Least Square.

Carrier Recovery

At the output of MIMO, the signals from the two polarizations are decoupled but the constellations are rotated due to the difference in frequencies between the transmitter and receiver lasers (Rx

is not sharing the same local oscillator as the Tx, so difference between W_{LO} and W_{rx} in equation 3.7 is tracked here). Therefore, both frequency and phase must be aligned or more like their difference must be corrected for [36] [37] [38]. Similar to adaptive filtering, that can be done in pilot-directed mode, blind or combination of the two. Nonlinearity is another impairment that can benefit from carrier recovery circuit, since SPM and XPM both produce a “phase-noise” like effect.

Non-linear (post) compensation

Due to the required intensive processing, in commercial modems there is no non-linear compensation at the receivers. However, with the trend in CMOS technology, it will be possible to implement back propagation algorithms to adaptively solve the NLSE. It is worth noting that backpropagation can compensate well for SPM, while to mitigate XPM and FWM, we need to know the information from the link, basically neighboring channels spacing and power distributions. That might be possible in static Submarine link and tend to be difficult in a mesh highly dynamic networks. As shown in the image below, using numerical methods such as Split-Step Fourier (SSF), we can simulate signal propagation by iteratively solving the Schrodinger equation.

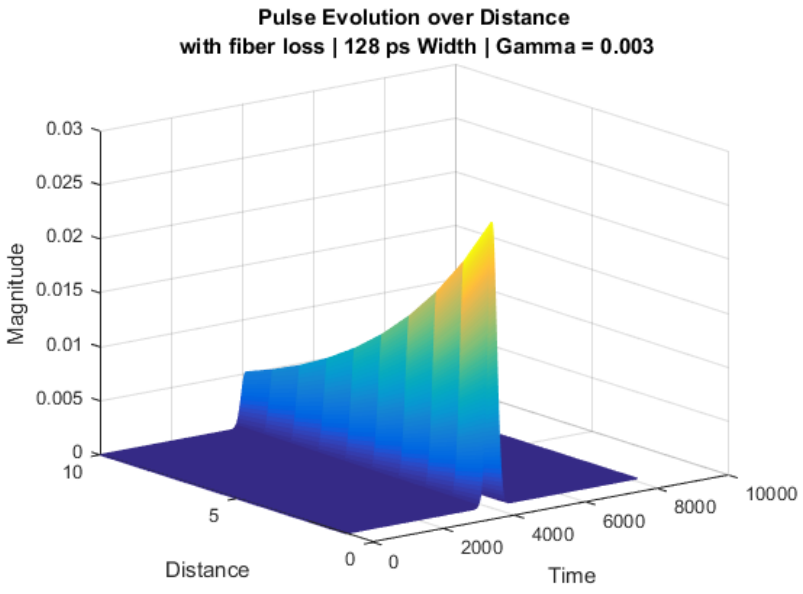

Figure 20: Pulse Propagation using SSF Method

The simplest implementation of the split step algorithm [11] is to propagate the field over step *h* in two stages. In the first step, nonlinearity acts alone, and $\hat{D}=0$. In the second, the non-linearity is zero, and dispersion acts alone.

$$A(z+h,t)\approx \exp\left(h\hat{D}\right)\exp\left(h\hat{N}\right)A(z,t) \quad (3.11)$$

The non-commutating nature of the linear and non-linear operators leads to a leading error term of order h^2. In the symmetrized split step algorithm [53], the non-linear operator is evaluated in the centre of the step, and the dispersion evaluated as two half-steps.

$$A(z+h,t)\approx \exp\left(\frac{h}{2}\hat{D}\right)\exp\left(h\hat{N}\left(z+\frac{h}{2}\right)\right)\exp\left(\frac{h}{2}\hat{D}\right)A(z,t) \quad (3.12)$$

A further refinement is to replace the non-linear step by an integral

$$A(z+h,t)\approx \exp\left(\frac{h}{2}\hat{D}\right)\exp\left(\int_{z}^{z+h}\hat{N}(z')dz'\right)\exp\left(\frac{h}{2}\hat{D}\right)A(z,t) \quad (3.13)$$

In figure below, we illustrate the SSF method.

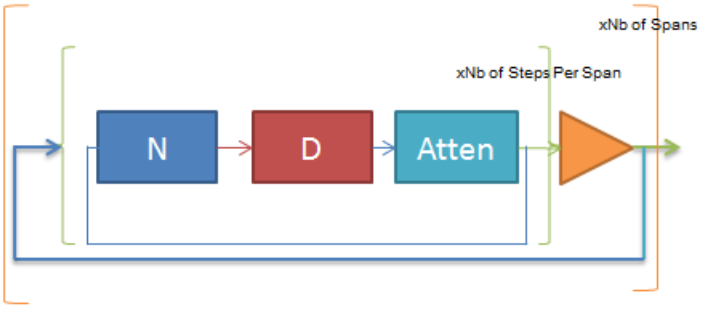

Figure 21: Fiber model with non-linearity, dispersion, attenuation and amplifier gain

Another method considered in optical fiber communication to approximate the nonlinearity is considering the nonlinear field as a perturbation compared to linear dispersion effect [39] [40].

$$E(t) = |E_{linear}\rangle + |a\rangle \quad (3.14)$$

Forward Error Correction

Forward Error Correction (FEC) blocks are typical in transponders, they help increasing the signal reach and allows for more design flexibility. Both hard and soft-decision FEC can be used after DSP. Standards such as G.709 has a coding gain of more than 6 dB at BER 10^{-15}. The FEC is preceded by a de-interleaver that is meant to shuffle error over many transmitted blocks. The size of the interleaver is important in the case of transients' kind of error in the fiber channels.

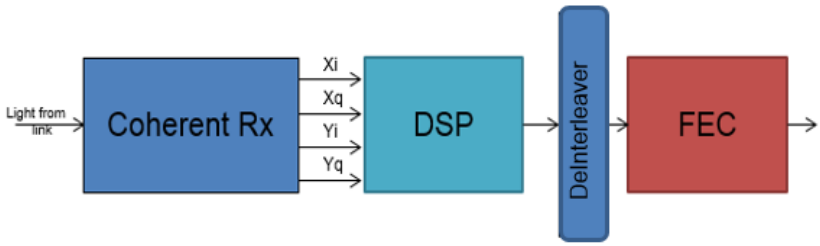

Figure 22: DSP & FEC in Coherent Receiver

Chapter 4 - Adaptive Filtering in Optical Coherent Software Defined Receivers in the Presence of State-of-Polarization Transients and Colored Noise

"He is a man of intelligence, but to act sensibly, intelligence is not enough." — Fyodor Dostoyevsky

4.1 - Introduction & Literature Review

THE era of data-drive and cloud based computation has arrived. To be able to accommodate the increased data rates and increased number of communicating devices on the internet, new techniques in optical telecommunications are being developed. The main vehicles for high-capacity networks are software-defined transceivers that use coherent detection and dual polarization. Dual polarization, introduced in [41], effective doubles the data rate compared to single polarization techniques. The core operation in dual-polarization communication systems is the adaptive filter which performs equalization to correct for the time-varying state-of-polarization (SOP) as well as other linear channel impairments. Studying both the convergence and tracking performance of the adaptive filters used in this process is important in understanding the limitations of the system.

The linear impairments encountered in an optical channel are a mix of deterministic and stochastic impairments. Chromatic dispersion (CD) is a type of deterministic impairment while polarization mode dispersion (PMD), polarization dependent loss (PDL) and (SOP) are stochastic ones.

A dual polarization optical signal has amplitude and phase in one polarization (X) and another amplitude and phase on the orthogonal polarization (Y). The received optical signal is a rotated version of the transmitted one. The rotation caused by the channel is either static or slowly varying allows the receiver to employ a linear adaptive filter to decouple the two polarizations from the received rotated optical signal. Algorithms such as the classical least mean squares (LMS) [42][43][44] and the constant modulus algorithm (CMA) [45] have been used to undo the effects of the channel rotation.

In this chapter, we are interested in the effects of fast SOP transients and PDL on the performance of the adaptive linear filter used to decouple the two polarizations of the received

optical signal. In particular, we wish to see how well the adaptive filters can track fast SOP transients in the presence of PDL and colored noise with limited RSNR penalty due to those impairments.

Optical ground wires (OPGW) are primarily deployed by the electrical utility industry. They shield the conductors from lightning strikes while providing a telecommunications path for third party communications. High-voltage lines carry electricity from the utility to the consumers while fiber optic cables provide telecommunication capability. OPGWs are being increasingly deployed to reduce costs compared to buried fibers; however, lightning strikes and other phenomena can cause the transmitted data to be exposed to fast SOP transients. In [46], it is stated that a 100 km length of OPGW can experience roughly 30 lightning strikes per year in Central Europe. The external structure of OPGW is constructed to discharge the lightning, but a Faraday Effect is observed on the two polarizations when a lightning strike occurs [47].

An in-depth study done using Verizon aerial fiber in [48, 49] showed that aerial fibers typically encounter higher SOP transients than those buried in the ground. In [50], data was collected from an OPGW plant in order to determine the correlation between SOP transients and lightning strikes. They were able to demonstrate a high correlation between lightning strikes and the occurrence of fast SOP transients which could achieve rates of up to 5.1 Mrads/sec. Laboratory experiments were conducted in [51,52] to emulate the effect of lightning on SOP transients observed in OPGW fibers. They showed that the rate of change in SOP increases as both the electrical current created by the lightning strike increases and the length of the cable increases. They demonstrated through repeated trials that, for a given lightning current and cable length, the variance of the measured SOP data was less than 0.5% about the mean. In [53], the authors report that wind speed and the high-voltage line current also have an effect on the SOP rate of change.

Temperature and other forces can also have an effect on SOP in fiber cables. For example, deep sea cables experience mean SOP variations of 200 Hz, [54], while the mean SOP rate of change is 50 Hz in buried cables, as shown in [55]. The authors of [56] found that the rate of SOP change is correlated to variations in ambient temperature.

Other causes of fast SOP variation are mechanical vibration of the fiber cable caused by the passage of trains or construction work in close proximity. In [57], a study of SOP induced by

mechanical vibration of Dispersion Slope Compensation (DSC) modules was done. The special case about DSCs is that they contain long fibers that is typically meant to compensate for dispersion of a span of the DWDM network (80 km). Certain packaging methodologies were introduced in [58] to reduce the fluctuations of SOP in DSC modules.

Much work has been done on reducing the RSNR penalty to compensate for the different impairments that are typical in coherent dual polarization communication systems over fiber cables. In [59], it was shown that PMD actually helps averaging the penalty due to PDL. This is due to the fact that PMD spreads both polarizations equally at the two extreme PDL axes of the fiber. In [9], coding on the X and Y polarizations is used to mitigate PDL to avoid worst case orientations, which in turn reduces the RSNR penalty due to PDL. However, neither study considered the effect of fast SOP transients.

In [60], the authors presented a field programmable gate array implementation of a coherent dual-polarization receiver where quadrature phase shift keying (QPSK) modulation is used. Operating at data rate of 2.8 Gb/s, their receiver's adaptive filter was able to track SOP transients of 5 KHz in the presence of 3 dB PDL in the link with a RSNR penalty of 0.5 dB. The work in [10] compared LMS algorithm to the recursive least square (RLS) algorithm in a system that employs spatial-division multiplexing (SDM), where multiple modes travel in the fiber in order to increase channel capacity. They show that the RLS has the superior convergence properties. The authors of [61] considered the effects of error feedback delay, using CMA, on the performance of the coherent receiver in the presence of CD. The work done in [62, 63] shows how pipelining and efficient implementation of the adaptive filter' feedback loop in the receiver help reducing the delay of the error signal used in the LMS tap weight updates by 18%.

In [64], authors looked at Kalman filtering to tracking SOP with some PDL and frequency offset. Despite the fact that Kalman requires $O(N^3)$ processing complexity which does not fit in the industry trend to reduce power consumption in modems, the prerequisite for a fiber model in order to get the prediction then compare to measurement for correction, makes it tough to generalize.

Constant Amplitude Zero Auto-Correlation (CAZAC) sequence are popular in wireless studies, they are used in long-term evolution (LTE). In [65], the authors performed a detailed study on the impact of CAZAC in long-haul transmission system viewed as chirp signals. In the studies undertaken in [35, 66], frequency domain equalization (FDE) is used to track the SOP transients,

using only QPSK modulation, in pilot-directed mode. The papers focused on the amount of averaging of the channel estimates in trade-off of back-to-back penalty and SOP transients tracking. The authors in [35, 66, 67] did not considering other types of optical fiber impairments such as PDL and optical filtering.

In this chapter, we investigate the performance of the LMS, normalized LMS (NLMS) and RLS algorithms for the adaptive filter in coherent receivers for dual-polarization optical signals in the presence of SOP transients, PDL and optical filters. We consider the limitation in practical implementation such as the error signal feedback delay. In section 4.2, we present the theoretical background and modulation formats that we use in our simulations. In section 4.3, we present a theoretical overview of coherent receivers and adaptive filtering. The simulation environment details are given in section 4.4. In section 4.5, we present our simulation results where we focus on the effect of SOP rate of change on RSNR penalty, as well as the trade-off between performance in back-to-back (i.e. patch cord fiber between transmitter and receiver) link configuration versus PDL penalty versus SOP tracking capabilities. As well, we compare different adaptive algorithms by simulating their convergence speed and maximum trackable SOP for a given SNR penalty. In Section 4.6, we discuss an idea related to autonomous intelligent networks. In Section 4.7, we provide our conclusions. It's worth noting that for all chapters, more elaborate conclusion(s) is provided in the last chapter of this thesis. The main *contributions* of this paper are the following:

1. Study of SOP tracking in the context of Software Defined Optical Transceivers with practical implementation limitation.
2. Illustrating the trade-off between back to back RSNR and PDL penalties versus SOP tracking penalty.
3. Presenting analysis and simulation, in both convergence and steady states, to compare the performance of LMS versus NLMS and RLS in presence of PDL and SOP.

4.2 - Adaptive Filters Architecture and Software Defined Transceivers

Next generation coherent receivers are designed to support high-speed, reduction in power consumption and flexible provisioning. They are an integral component in the migration to Software Defined Optical Networks [68]. The programmability is required so that network operators can switch between modulation formats, such as the ones in Fig.1, based on link margin and available bandwidth. Therefore, it is worth studying the performance of the adaptive filters with the same practical limitations for different constellations (different line rates). We consider

QPSK and 16QAM, as rich modulation format deployed for long reach link, throughout most of the study. As well, we look at SOP rate of change tracking, for a different SNR penalty, of LMS for QPSK and 8/16/32/64 QAM. The PDL values, associated with modulation formats shown in Fig. 23, are estimates based on the possible number of spans per bit rate.

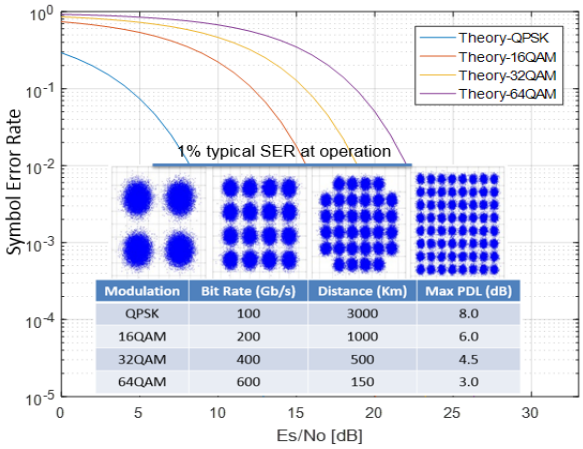

Figure 23: SER versus signal-to-noise ratio (SNR) for different constellations

In a typical link budgeting process, operators and equipment vendors include SNR margin when planning optical networks [69]. Examples of the reasons for the unused what we are call “Fiber Link SNR Margin” are to account for laser aging, amplifier power transients, pixels drift in ROADMs and fast SOP transients. The trends in standardization bodies such asEEE802.3/OIF are focusing on, among other things, Soft-Decoding Forward Error Correction (FEC) with high threshold (In [70], FEC threshold used is 4.5x10-2 with 24% overhead for 64QAM modulation format and propagation scenario of 300 km). Therefore, we chose the FEC threshold, that will define our operating point with base SNR at 4.5x10-2 for all modulation formats studied

Link SNR = SNR (@ BER = 4.5 %) + “Fiber Link SNR Margin”

4.3 - Theoretical Background

The performance of digital fiber optics communications systems, impaired with dispersive effects such as chromatic dispersion and PMD, depends highly how reliably the coherent receivers distinguish the closely spaced symbols. With coherent receivers, as shown in Fig. 24, any linear distortion in the optical domain can be treated as linear in the electrical domain. That permits the use of finite impulse response filters (FIR) to compensate for impairments since both amplitude and phase are preserved. The choice between block frequency domain implementation or time-

domain convolution is determined by the targeted amount of PMD to support. In [71], the authors compared time versus frequency domain filtering in term of hardware gate counts by detailing the number of operations required for both coefficients update and filtering. As we see in Fig. 25 that once the number of taps per branch is more than 7, then frequency domain filtering is recommended. Another architectural decision is data-directed versus pilot directed, while the former increases throughput, it is more prone to error.

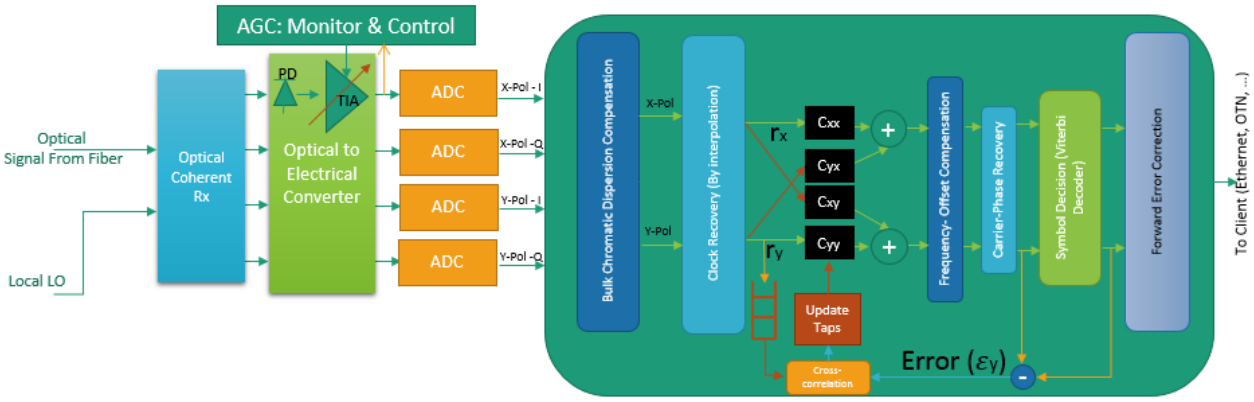

Figure 24: Typical architecture of a coherent receiver

Adaptive filtering methods, such as LMS, are the core elements in the design of the coherent receivers. LMS converges toward the Weiner solution [43]. Since the error calculated in decision-directed modes are part of the update equations, the availability of the error vector is key to making the right update to compensate for the time-varying channel impairments. The two-main time-varying impairments we will consider are fast SOP transients and PDL. The former is usually illustrated on the Poincaré sphere and modelled mathematically as changes in the Stokes vector representation. The instantaneous PDL, resulting from contributions of many random birefringence in fibers and optical components along the link, can be chosen from a Maxwell-distribution [72]. It is considered a time-varying impairment where one of the received polarizations is attenuated in a randomly fashion.

A typical digital signal processor in a coherent receiver contains static and adaptive filters, carrier phase/frequency recovery as detailed in [73], and a threshold-based decision block. For adaptive filter algorithms to work in data-directed mode, the error is measured at the output of the decision block. Signal processing operates at much slower speed than the sampling rate. As the modulation order increases, the complexity of the carrier recovery algorithm and detector/decoder

increases and results in increased feedback delay (FD) of the error signal used to update the filter tap weights. As part of design, there will be trade-offs between size, power and amount of FD. The more parallelism in the implementation, i.e. processing more symbols at same time, the smaller the FD but then the number of hardware gates is larger due to increase number of operations per Application-Specific Integrated Circuit (ASIC) clock, as shown in [74], and therefore power consumption will be higher.

In dual-polarization coherent detection, the adaptive filter can have one of two configurations: 2x2 MIMO (Multiple Input Multiple Output) system equivalent to 4 independent filters where X and Y common impairment are compensated, or 4x4 MIMO [75, 76], at the price of more power consumption, that can compensate for X and Y, as well, in-phase and quadrature related impairments such as delay and loss/gain imbalance. In the presence of FD in the adaptive filter loop, the update equation is modified where current update is based on outdated input data r and error (ε) by FD blocks. The larger the loop delay, the greater the lag error which results in limitations on stability and bandwidth. This reduces the maximum value for the adaptive filter step size which in turn limits the maximum rate of channel state variations that the adaptive filter can track. The main advantage of having the FIR (finite-impulse response) operates per block of symbols is the reduction of computational complexity. Knowing that with baud rate equal to 80 Giga-Baud (GBaud), the symbols spacing is 12.5 ps. Assuming the requirement set by link-budget team for the PMD handling of the coherent transponder to be peak of 200 ps. With adaptive equalizer operating at T (symbol period)/2 spacing, therefore, the FIR filter needs 32 taps.

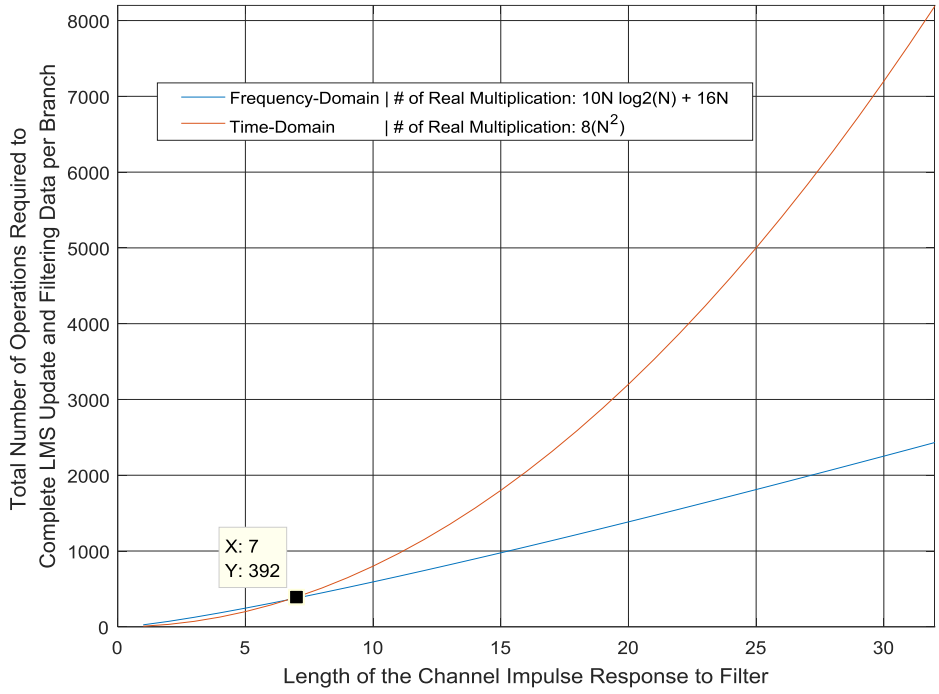

Figure 25: Computational complexity of time versus frequency domain

4.3.1 - Derivation of Minimum Mean-Square-Error Solution

Using quantum mechanics notations, the 2x1 column vector representing the received signal at input of the adaptive filter is defined as:

$$|r(n)\rangle = \mathbf{M}\,|s(n)\rangle + |u(n)\rangle \qquad (4.1)$$

With **M**, the jones matrix representing the channel response at specific time instance. **s** the 2x1 transmitted signal vector with two polarizations, X and Y.

$$|r(n)\rangle = \begin{pmatrix} r_1(n) \\ r_2(n) \end{pmatrix} \qquad (4.2)$$

And **u**, 2x1 vector, is modelling additive noise. For now, assuming it is white with mean 0:

$$E\{|u(n)\rangle\,\langle u(n)|\} = \sigma^2 \mathrm{I} \qquad (4.3)$$

Without loss of generality, let's assume:

$$E\{|s(n)\rangle\,\langle s(n)|\} = \mathrm{I} \qquad (4.4)$$

We would like to estimate **C**, 2x2 correction matrix, in the least square sense. Where:

$$\mathbf{C} = \begin{bmatrix} C_{11} & C_{12} \\ C_{21} & C_{22} \end{bmatrix}$$

The first row generates X-polarization when combined with received vector and second row generates Y-polarization. Therefore, each element is **C** has two indexes. And the estimated symbol is obtained as follow:

$$|s_{est}(n)\rangle = \mathbf{C}\,|r(n)\rangle \qquad (4.5)$$

And the error is equal to:

$$|e(n)\rangle = |s(n)\rangle - |s_{est}(n)\rangle = |s(n)\rangle - \mathbf{C}\,|r(n)\rangle \qquad (4.6)$$

Let's define z as the mean-square error (MSE):

$$z = E\{\langle e(n)|e(n)\rangle\} \qquad (4.7)$$

Defining a, b, c, j and k scalar that are selected from the set {1,2}. In component, per polarization, form:

$$z_a = E\{e_a^*(n)e_a(n)\} \qquad (4.8)$$

Where,

$$e_a(n) = s_a(n) - C_{ab}r_b(b) \qquad (4.9)$$

The mse is then derived as follow:

$$z_a = E\{(s_a^*(n) - C_{ab}^* r_b^*(n))\, e_a(n)\} \qquad (4.10)$$

Therefore, **C** is found by minimizing z with respect to elements of **C**. With δ is the dirac-delta discrete function, we get the popular the "orthogonality principle":

$$\frac{\partial z}{\partial C_{jk}^*} = E\left\{\left(-\frac{\partial C_{ab}}{\partial C_{jk}^*}\, r_b^*\right) e_a(n)\right\}$$

$$= -E\{\, r_b^*\, e_a(n)\, \delta_{ja}\delta_{jk}\}$$

$$= E\{\, r_k^*\, e_j(n)\} = 0 \qquad (4.11)$$

Based on the above, we will look for **C**. With:

$$e_j(n) = s_j(n) - C_{jb}r_b(b) \qquad (4.12)$$

Replacing eq. 4.12 in 4.11, we obtain:

$$E\{\, r_k^*\, (s_j(n) - \, C_{jb} r_b(b))\} = 0 \qquad (4.13)$$

$$E\{\, r_k^*\, s_j(n)\} = C_{jb}\, E\{\, r_k^*\, r_b(b)\} \qquad (4.14)$$

The first term is expanded as follow:

$$\begin{aligned} E\{\, r_k^*\, s_j(n)\} &= E\{\, s_j(n)\, (M_{kc}^*\, s_k^*(n) + \, u_k^*(n))\} \\ &= E\left\{\left(M_{kc}^*\, s_k^*(n)\, s_j(n)\right)\right\} + 0 \\ &= M_{kc}^*\, \delta_{je} = M_{kj}^* \end{aligned} \qquad (4.15)$$

The second term of eq. 4.14 is expressed as follow:

$$\begin{aligned} E\{\, r_k^*\, r_b(b)\} &= E\left\{\left(M_{kc}^*\, s_c^*(n) + \, u_k^*(n)\right)\, \left(M_{ba}\, s_a\, (n) + \, u_b\, (n)\right)\right\} \\ &= E\left\{\left(M_{ba}\, M_{kc}^*\, s_a\, (n)\, s_c^*(n)\right)\right\} + E\left\{\left(u_b\, (n)\, u_k^*(n)\right)\right\} \\ &= (M_{ba}\, \delta_{ac})\, M_{kc}^* + \sigma^2 \delta_{bk} \\ &= M_{bc}\, M_{kc}^* + \sigma^2 \delta_{bk} \end{aligned} \qquad (4.16)$$

Replacing eq. 4.15 and 4.16 back in eq. 4.14:

$$M_{kj}^* = C_{jb}(M_{bc}\, M_{kc}^* + \sigma^2 \delta_{bk}) \qquad (4.17)$$

Therefore, for while noise and minimum mean-square error (MMSE), the correction matrix is estimated as:

$$\mathbf{C} = \mathbf{M}^H(\mathbf{M}\, \mathbf{M}^H + \sigma^2 \boldsymbol{I})^{-1} \qquad (4.18)$$

$(.)^H$ *and* $(.)^{-1}$ are, respectively, Hermitian and inverse operators. When ignoring the variance of the noise, we get the zero-forcing (ZF) solution:

$$\begin{aligned} \mathbf{C} &= \mathbf{M}^H(\mathbf{M}\, \mathbf{M}^*)^{-1} \\ &= \mathbf{M}^H(\mathbf{M}^{H^{-1}}\, \mathbf{M}^{-1}) \\ &= \mathbf{M}^{-1} \end{aligned} \qquad (4.19)$$

In the case of colored noise, each polarization is received as follow:

$$r_a(n) = M_{ab}\, s_b\, (n) + N_{ab}\, u_b\, (n) \qquad (4.20)$$

With **W** defined as the noise covariance matrix, eq. 4.3 becomes:

$$E\{\mathbf{N}|u(n)\rangle\,\langle u(n)|\mathbf{N}^H\} = \mathbf{N}\,\sigma^2\,\mathbf{N}^H$$

$$= \sigma^2\,\mathbf{N}\mathbf{N}^{\boldsymbol{H}} = \sigma^2\,\mathbf{W} \qquad (4.21)$$

With the orthogonality principle in eq. 4.11 still hold, the derivation leads to:

$$\mathbf{C} = \mathbf{M}^H(\mathbf{M}\quad\mathbf{M}^H + \sigma^2\mathbf{W})^{-1} \qquad (4.22)$$

Assuming same input-output relationship as in eq. 4.1, when solving the MMSE:

$$MMSE = \min E(|r - \mathbf{M}s|^2) \qquad (4.23)$$

We get the popular Wiener–Hopf equations. The coefficients of the optimum channel estimate, vector, are derived as follow:

$$\boldsymbol{C} = {}^{\mathbf{R}_{sr}}/_{\mathbf{R}_{rr}} \qquad (4.24)$$

Where: $\mathbf{R}_{rr}$ is the autocorrelation matrix of the received data and $\mathbf{R}_{sr}$ is the cross-correlation vector between the tap inputs and the desired response. Both matrices are illustrated in appendix A.

$$\mathbf{R}_{rr} = E[r\,r^T] \qquad (4.25)$$

$$\mathbf{R}_{sr} = E[s\,r^T] \qquad (4.26)$$

The issue is that computing the autocorrelation and cross-correlation in real-time manner is not possible, especially when processing a block of 512 symbols. Hence, the need for iterative methods to approach such the optimum coefficients.

4.3.2 – Filter Structure & Iterative Adaptive Methods

FIR structure is shown in Fig. 26. Received bits are delayed, multiplied by tap coefficients, which may be adaptive, and then summed. The tap delay (t_1.. t_N) may be equal to the symbol period, or a fraction of it. To reduce receiver noise, by blocking output band noise, the receiver bandwidth is usually less than the signal bandwidth. A fractional equalizer with tap delays matched to the receiver bandwidth, or to the transmitted pulse shape (e.g. raised cosine), can help reduce ISI or channel distortion [23]. The ISI may be due to chromatic dispersion, PMD, channel multiplexers/demultiplexers, ROADMs or non-ideal transmitter or receiver responses.

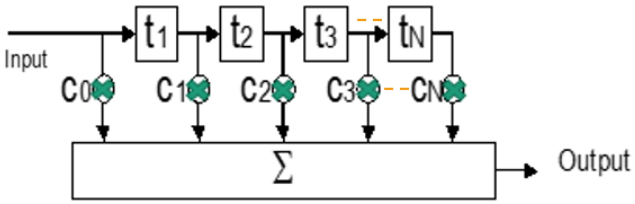

Figure 26: Structure of FIR per Branch

The waveform at the output of the transversal filter is:

$$Output(t) = \sum_{i=0}^{N} C_i \,.\, Input(t - t_i) \qquad (4.27)$$

For the four LMS-based filters, shown in Fig. 24, the update algorithm can be expressed by the following equations when taking the feedback delay in consideration with subscript are based on the polarization:

$$C_{xx}(n+1) = C_{xx}(n) - \mu\, r^*_{x,n-FD}\varepsilon_{x,n-FD} \qquad (4.28)$$
$$C_{yx}(n+1) = C_{yx}(n) - \mu\, r^*_{y,n-FD}\varepsilon_{x,n-FD} \qquad (4.29)$$
$$C_{xy}(n+1) = C_{xy}(n) - \mu\, r^*_{x,n-FD}\varepsilon_{y,n-FD} \qquad (4.30)$$
$$C_{yy}(n+1) = C_{yy}(n) - \mu\, r^*_{y,n-FD}\varepsilon_{y,n-FD} \qquad (4.31)$$

Where *C* is one of the coefficients of the adaptive filter shown on Fig. 26, ε is the error signal fed back from the output of the decision circuit to use in the tap weight update and *r* is the input signal buffered by FD blocks. For NLMS, the step size μ is normalized by the power of the 2x1 received jones vector.

The standard RLS adaptive algorithm considered in this paper is based on the update equations below:

$$\mathbf{C}_{RLS}(n+1) = \mathbf{C}_{RLS}(n) + \mathbf{P}(n) r_{n-FD}\varepsilon_{n-FD} \qquad (4.32)$$

$$\mathbf{P}(n+1) = \frac{1}{\lambda + r(n)^T \mathbf{P}(n-1) r(n)} \left(\mathbf{P}(n) - \mathbf{P}(n) r(n) r(n)^T P\right) \qquad (4.33)$$

with *r* and *ε* are 2x1 vectors, *λ* is the forgetting factor. $\mathbf{P}$ and $\mathbf{C}_{RLS}$ (same for LMS/NLMS) are 2x2 matrices representing all four FIRs as follow:

$$\mathbf{C}_{RLS} = \begin{bmatrix} C_{xx} & C_{yx} \\ C_{xy} & C_{yy} \end{bmatrix} \qquad (4.34)$$

In the case of multi-modulus algorithm (MMA), an upgrade of CMA for multi-level constellations, the error function is:

$$\varepsilon_x = \widehat{r^2} - |\widehat{y_x}\ |^2 \qquad (4.35)$$

$$\varepsilon_y = \widehat{r^2} - |\widehat{y_y}\ |^2 \qquad (4.36)$$

Where r is the nearest constellation point measured at the output of the adaptive filter. The update equation is then similar to LMS:

$$C_{xx}(n+1) = C_{xx}(n) - (\mu/2)\, r^*_{x,n-FD}\, \varepsilon_{x,n-FD} \qquad (4.37)$$

The filtered data per polarization going to carrier recovery block is therefore a combination of two branches as shown below:

$$x_{out} = \boldsymbol{C}_{xx}\,.r_x + \boldsymbol{C}_{yx}\,.r_y \qquad (4.38)$$

$$y_{out} = \boldsymbol{C}_{yy}\,.r_y + \boldsymbol{C}_{xy}\,.r_x \qquad (4.39)$$

The MMSE, minimum mean-square solution, as we showed in previous section, will take this form when *M* is the frequency response of the channel and N_0 is the noise variance:

$$\boldsymbol{C}_{opt} = [M^H M + N_0\, I]^{-1}\, M^H \qquad (4.40)$$

$(.)^H\ and\ (.)^{-1}$ are, respectively, Hermitian and inverse operators. The coefficient vector error, per branch, is defined as:

$$\boldsymbol{q} = \boldsymbol{C} - \boldsymbol{C}_{opt} \qquad (4.41)$$

PDL accumulates in a link mainly due to birefringent elements (mechanical stress or variability in the manufacturing process) and Wavelength Selective Switches (WSSs) [77]. With general Jones 2x2 matrix is shown in the equation below:

$$\boldsymbol{H}_{rotation\ only} = \begin{bmatrix} \cos(\theta)\,.\exp(i\Phi) & \sin(\theta)\,.\exp(i\Phi) \\ -\sin(\theta)\,.\exp(-i\Phi) & \cos(\theta)\,.\exp(-i\Phi) \end{bmatrix} \qquad (4.42)$$

We see how the different orientations of PDL affect the system SNR penalty. PDL is memoryless channel impairment, it degrades polarization-dependent OSNR. Adaptive filters can estimate the effect as in [78], but it can't compensate for it as in the case of PMD. Fig. 27 is

generated by applying MMSE optimal solution, eq. 4.37, to polarization-multiplexed 16QAM data stream impacted by noise, PDL is constant of 6 dB and a rotation matrix as in eq. 4.42. As we see, when the two polarizations are attenuated by same factor, i.e. θ is 45 degrees, the SNR penalty is minimized. Conventional decoders, such as minimum Euclidian distance, are customized for channels impaired with additive white Gaussian noise (AWGN) [79], therefore they are not optimal for colored noise such as PDL.

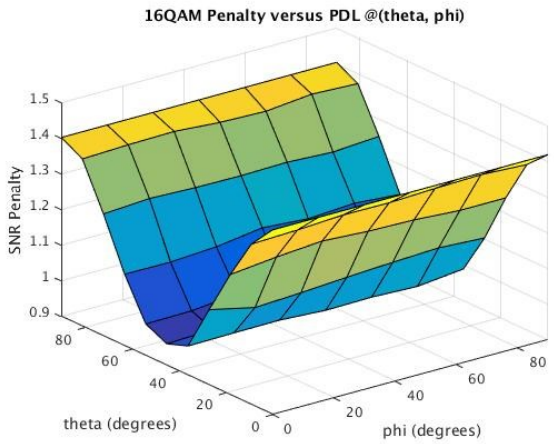

Figure 27: Theoretical SNR penalty for 16QAM in presence of 6 dB PDL

Both pilot-directed (or training-based) and data-direction (or decision-directed) adaptive filtering are used in commercial products. The obvious disadvantage of the former is the reduction of the data load within the transmitted burst, especially if the channel frequency response is long (such as in the case of large chromatic dispersion). While the latter requires the eye of the channel to be open in order for the filter to converge. One way of dealing with such scenario is to train the receiver first then switch to data-directed. We used CAZAC training symbols in our simulation as they are studied in other literature [66]. The main advantages of using CAZAC set of symbols as pilot in coherent optical receivers:

- Constant amplitude reduces the transient in power, lower peak-to-average power ratio, which is good for not introducing further nonlinearities (self-phase modulation and cross-phase modulation) especially in long-haul/submarine transmission systems.

- Their good periodic correlation properties allow for good channel estimation.

With N_{ZC} the number of symbols transmitted per burst, the CAZAC set is calculated as follow:

$$a_q(m) = e^{-j\frac{\pi * q * m * (m+1)}{N_{ZC}}} \qquad 0 \leq m \leq N_{ZC} \qquad (4.43)$$

4.4 - Simulation Methodology

4.4.1 - Limitations

We make the following limiting assumptions which can be addressed in future work:

1. All dispersion is assumed to be compensated by the static FIR filter.
2. No laser offset between Tx and Rx., as well 0 MHz laser linewidth, i.e. both carrier frequency and phase recovery circuits in Fig. 24 are bypassed. The reason is that typically frequency offset recovery is pilot-based solution with high tracking bandwidth.
3. Jitter penalties are not taken into account. In practice, PDL and SOP have impact on jitter estimators [80] and untracked jitter will cause an error in sampling the symbols at the ADC, therefore higher SNR penalty.
4. No methods to help in PDL equalization considered at the Electro-Optical front end. For example, as shown in [81], automatic gain control can offset some PDL effects. Therefore, it is up to the adaptive filters to equalize for PDL and track SOP changes.
5. SOP transients only occurs when receiver is in steady-state except when we look at convergence speed of the adaptive filters.
6. No A/D quantization noise or arithmetic rounding errors.

4.4.2 - Simulation Environment

All simulations were conducted using Matlab 2016b©. PDL is typically simplified as one bulk random attenuator for one of the two polarizations. However, in literature such as [80], the ingress and egress rotation matrices are modelled as being the same; which is not precise. In this correspondence, our model has the two unitary matrices (represented by RI and RII), functions of θ and β, independent and PMD element followed by another SOP rotation (RIII):

$$\boldsymbol{H_{channel}} = \underbrace{\begin{bmatrix} \cos(\theta) & \sin(\theta) \\ -\sin(\theta) & \cos(\theta) \end{bmatrix}}_{\text{RI}} \underbrace{\begin{bmatrix} 1 & 0 \\ 0 & k \end{bmatrix}}_{\text{PDL}} \underbrace{\begin{bmatrix} \cos(\beta) & \sin(\beta) \\ -\sin(\beta) & \cos(\beta) \end{bmatrix}}_{\text{RII}} \underbrace{\begin{bmatrix} exp(\frac{i}{2}\tau\ ) & 0 \\ 0 & exp(-\frac{i}{2}\tau\ ) \end{bmatrix}}_{\text{PMD}} \underbrace{\begin{bmatrix} \cos(\alpha) & \sin(\alpha) \\ -\sin(\alpha) & \cos(\alpha) \end{bmatrix}}_{\text{RIII}} \qquad (4.44)$$

where 0 < k < 1. The attenuation in dB is:

$$PDL_{dB} = -20 * log_{10}(k) \qquad (4.45)$$

Since θ and β are randomly varying, the two polarizations (X and Y) are mixed in a time-varying

manner. And $\tau > 0$ when PMD is introduced. It is up to adaptive filter at the receiver to correct and track for the time-varying crosstalk effects. The high-level parameters and assumptions of the simulator are shown below:

i. Symbol rate of 33 GBaud
ii. 11 complex taps per filter
iii. Fixed block size of 512 symbols.
iv. Uniform steps, as shown in Fig. 28 & 30, over simulated stream of bits when introducing SOP rotation angle (θ) to the signal, that is equivalent to:

$$\theta(n+1) - \theta(n) = \theta(n) - \theta(n-1) \qquad (4.46)$$

v. SOP of full 2π rotation on Poincaré sphere was performed for each tested SOP rate of change.

An example of three SOP transient, with rotation around S3, simulated by varying θ over time is illustrated in two-dimensional graph in Fig. 28.

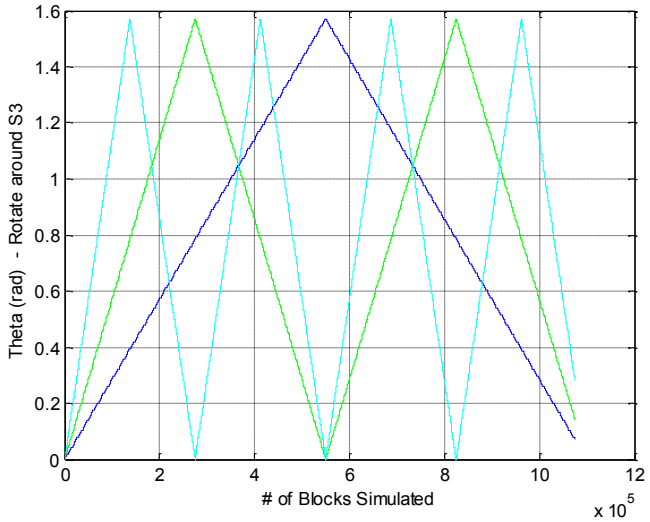

Figure 28: Rotation angle applied per block in simulation based on the target SOP rate of change

The Stokes space is useful to help picturing the conditions of the state of polarization when debugging and monitor changes signal in fiber. Any polarization state of fully polarized light can be depicted by a point in this three-dimensional space that lies on the surface of a sphere - the so-called Poincaré sphere that has its center in the origin of the coordinate system. The vector representation of each dual-polarization point on the Poincare sphere is:

$$\vec{S} = \begin{matrix} S_1 \\ S_2 \\ S_3 \end{matrix}$$

And with S_o is the total energy of the symbol. Typically, that is equal to 1 and hence we require S_1, S_2 and S_3 to represent any point on the sphere.

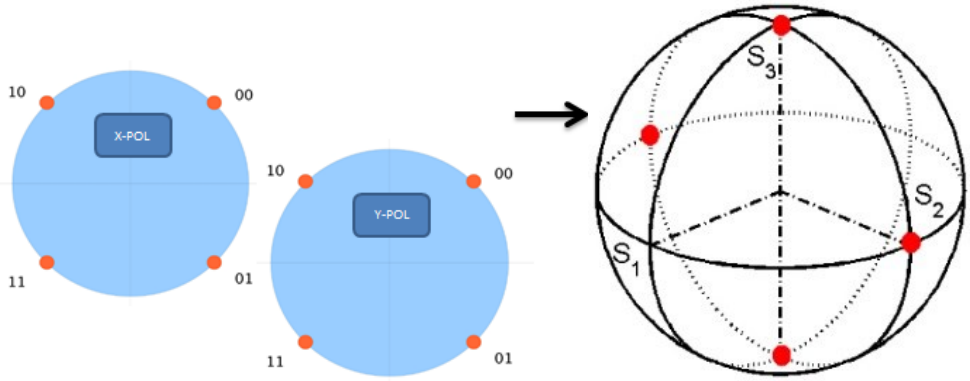

Figure 29: From constellation to SOP of Polarization-Multiplexed QPSK on the Poincaré sphere

On 3D Poincare sphere, various SOP change trajectories, can be simulated by combining rotations of variables in eq. 4.39. Three examples are illustrated below:

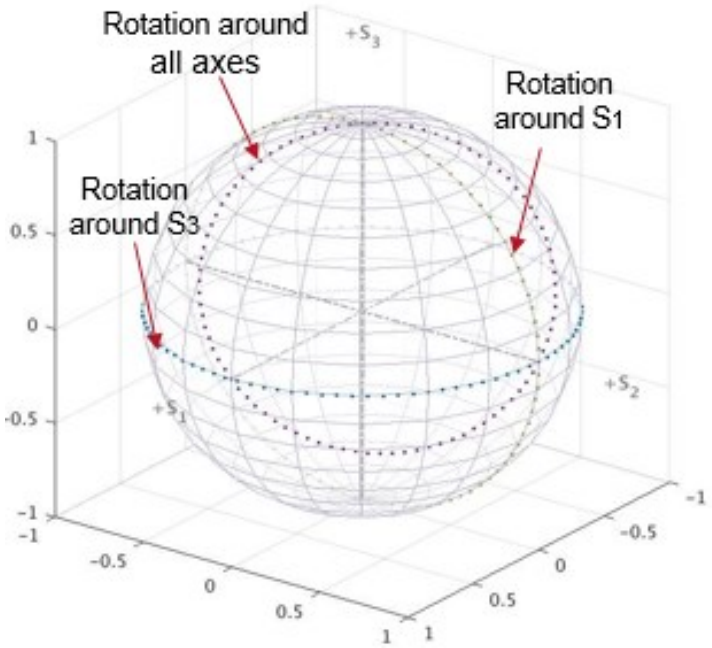

Figure 30: Poincare sphere illustrating different transient trajectories

4.5 - Simulation Results

In this section we present our simulation results based on the theory and assumptions above. We

begin by showing the impact of adaptive filter step-size on both back to back and PDL RSNR penalty versus the ability to track fast SOP transient. We will look at the limitation of feedback delay for different modulation formats. At the end, we compare different adaptive filtering methods in the presence of colored-noise such as PDL.

4.5.1 - SOP Tracking with LMS

In this sub-section we will use floating point LMS algorithm to train the adaptive filters taps.

4.5.1.1 - Impact of Step Size on SNR

We know from [82] that large step size increases misadjustment errors, while small step size make adaptation of taps prone to lag errors. As we see below, even in the back-to-back (B2B) condition (PDL = 0.0 dB as in Fig. 31), the SNR penalty increases as function of step size. In our simulation, the taps are initialized to an 2x2 identity matrix. As we increase PDL, which causes more fluctuation in the measured SNR at the output of the adaptive filter (higher rate of the error), the slope of the SNR penalty gets higher.

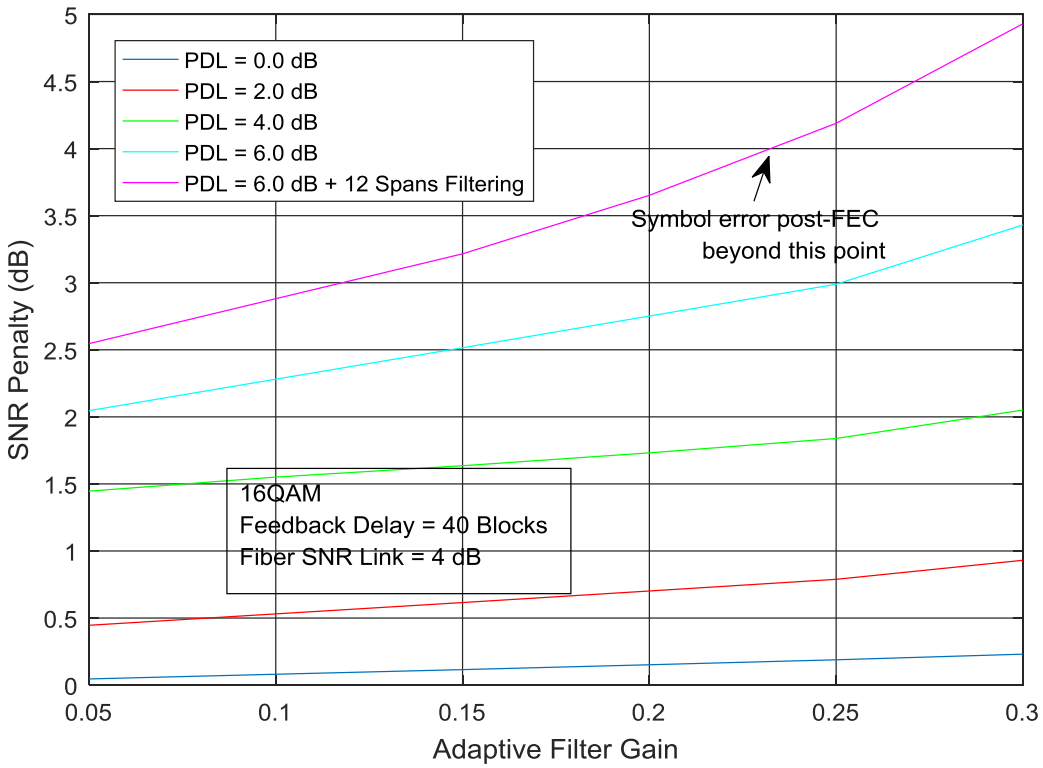

Figure 31: SNR Penalty versus Gain

4.5.1.2 - Trade-Offs in Presence of Feedback Delay

As error feedback delay increases, the lag error becomes more dominant in the adaptive loop. And as discussed above, when high step size is utilized, we amplify the distortion by mis-adjustment, therefore, we get even more decision error that will be translated into larger SNR penalty. Using rich modulation formats, comparing to BPSK, the decoding process becomes more complex, as well carrier recovery circuits; therefore, FD is becoming larger in state-of-the-art coherent receivers. The new upper bound on the step size is a function of error signal feedback delay, it is governed by the equation below (in here *FD* starting index is 0) [83]:

$$0 < \mu < \frac{2}{\lambda_{max}} * \sin\frac{\pi}{2(2*FD+1)} \qquad (4.47)$$

In Fig. 32, we show the maximum LMS gain (or step size) allowed to ensure stability as function of FD.

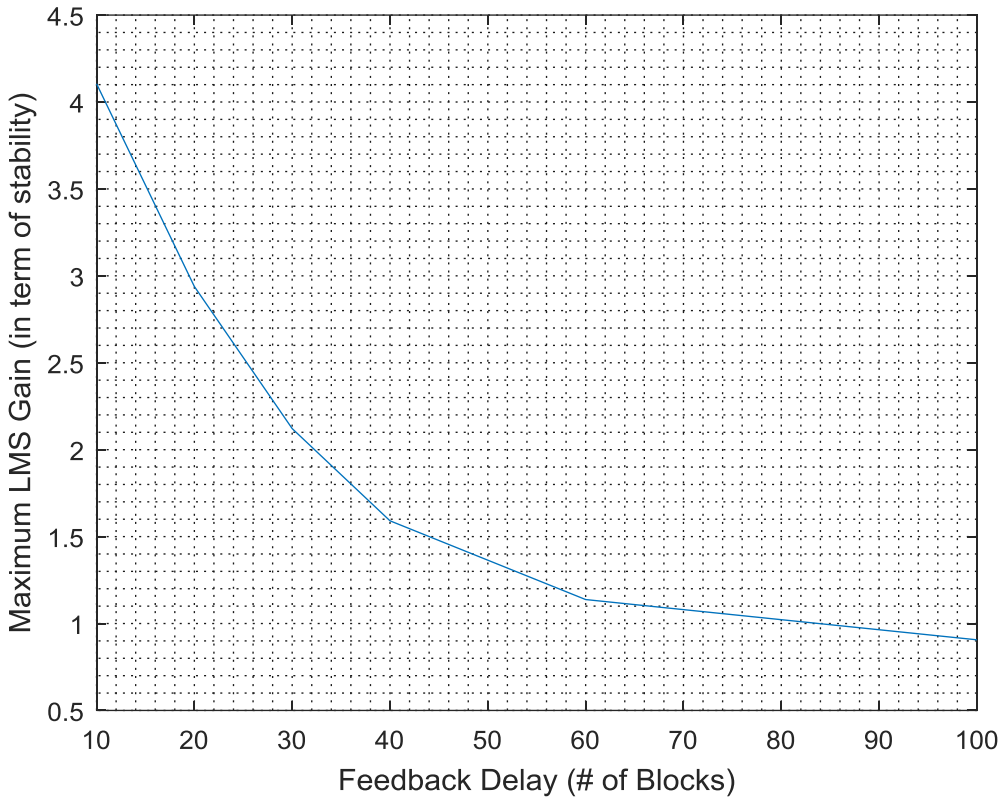

Figure 32: Maximum LMS gain versus delay

For 16QAM, as we see in the figures 31 and 33 there is a trade-off between B2B/PDL RSNR penalty versus SOP rate of change tracking. The smaller the step size, the more stable adaptive

filter is, however the slower it is to adjust the directions of the taps to track the changes in the state of polarization. On the other hand, the larger the step size the faster the adaptation rate. It is shown as well that the SNR Margin on the link does not make much of a difference in presence of large feedback delay (FD). We compared the results of data-directed (DD) to 16 symbols pilot-directed (PD), equivalent to ~ 5% overhead, the latter by default has a FD of 1 since the symbols are known to the receiver and there is no need to get feedback to measure the error. However, if no avergaring performed on multiple measures of the received pilot-symbols, the SNR penalty is high due to noisy estimates. On the other hand, as expected due to small delay, the tracking speed of CAZAC-based PD is higher than tracking capability than DD.

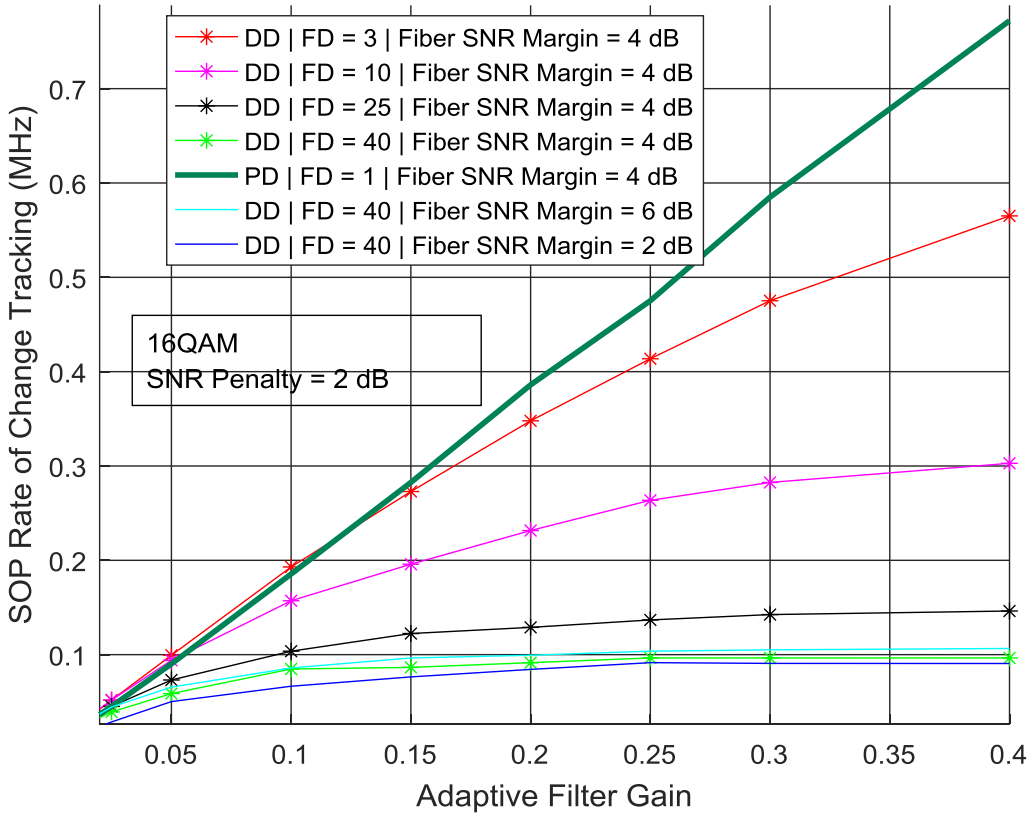

Figure 33: Maximum SOP versus Step Size using 16QAM

When we consider QPSK modulation, our results show similar trends as 16QAM where B2B penalty and SOP tracking capability both increase as function of step size. In [66], SOP related tracking capability is studied, authors used CAZAC-based frequency-domain zero-forcing and minimum mean square error to get channel estimation. As well, with feedback delay set to larger value (as doing more averaging on training-symbols), the maximum SOP tracking capability for a fixed penalty is reduced. It is shown as well that DD has much lower back to back penalty (Fig.

34) and, for same SNR penalty, higher SOP tracking (Fig. 35) when FD is set to 1. The reason is that in DD there is more data available to tune the coefficients, unlike PD where only 16 data points are used. The SNR penalty of PD can be reduced by performing more averaging of multiple received training symbols, before updating filtering coefficients, especially when operating in OSNR link (i.e. noisy channel).

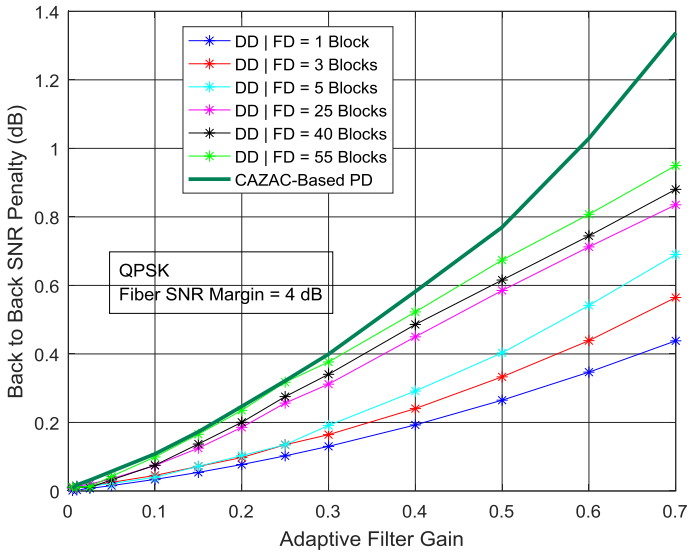

Figure 34: Back to back SNR penalty as function of step size

One way to increase spectral efficiencies in optical fiber links is to increase the baud-rate, i.e. symbol rate. With new CMOS technologies, such as 16 nm [84], new high-speed data converters working at 80 and 100 GBaud, as shown in [85] and [86] respectively, are implemented in nowadays products. That will be converted to faster signal processing; therefore, faster convergence and more tracking of change in SOP transients. Clock speed that is driving the adaptive filter and other functionalities in the ASIC is an important factor that determines amount of SOP tracking, as well as in [87], if buffering of incoming data is used then SOP rotation feed-forward correction is performed, then the SNR penalty can be reduced, and SOP tracking tolerance increased. In [88] & [89], authors introduced a method to choose (variable) step size per coefficient based on the feedback error (or link SNR) that helped reducing the tradeoff between mis-adjustment and tracking ability of the fixed step size.

4.5.1.3 - SNR Penalty versus SOP Transients

To avoid disturbing traffic, network operators design their dense-wavelength division multiplexing links with some OSNR margin (typical 3 to 4 dB). It is reflected in their link budget to account, as

shown in [90], for SOP transients and for end-of-life related performance degradations such as lasers drift, center frequencies per port drift of link filtering and changes in transfer functions of electro-optical components. Increasing the LMS gain and the SOP tracking penalty introduce a noise penalty and not an OSNR penalty. It is not correct to use OSNR penalty (in dB) as a comparator because it unfairly disadvantages any modulation format that has a higher back-to-back RSNR.

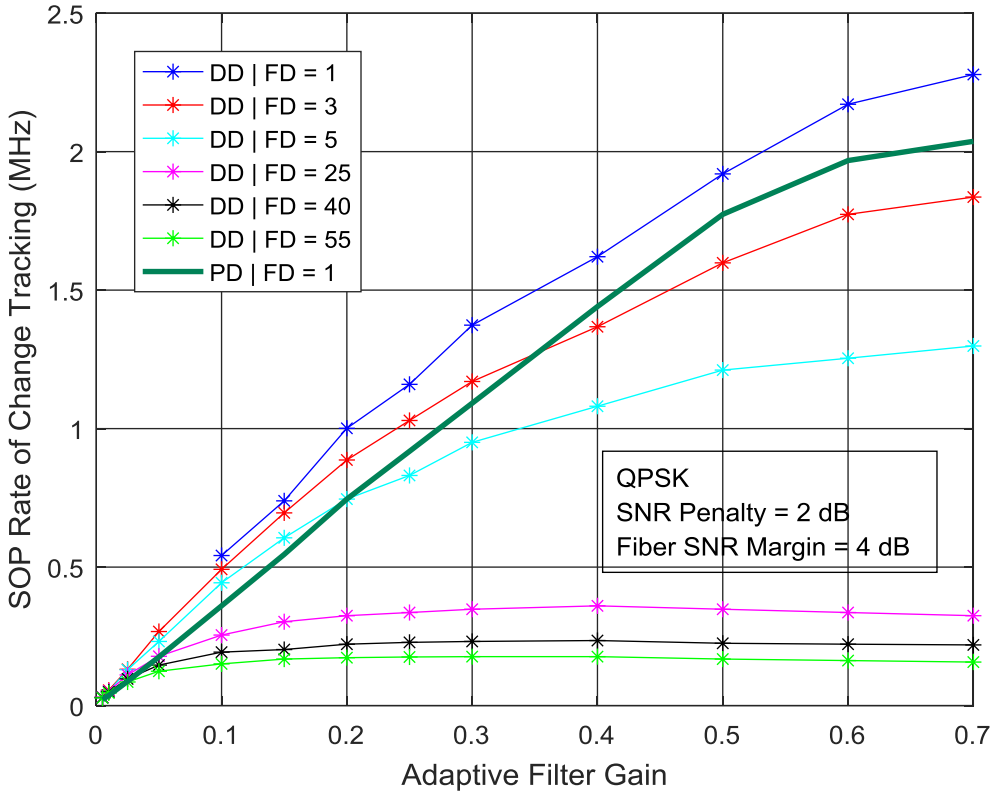

Figure 35: Maximum SOP versus Step Size using QPSK

As described in [91], higher-order constellations are more sensitive to noise. Therefore, noise penalty is the relevant figure of merit for comparison for different modulation format and baud-rates. However, for the sake of performing comparison with a metric that used in typical link budget planning tools, we will use SNR penalty (and not Optical-SNR which takes in consideration the bandwidth of the signal versus the 12.5 GHz noise bandwidth), while the noise can be retrieved as follow:

$$Noise_{dB} = -10 * log_{10}(10^{-\frac{RSNR_{base}}{10}} - 10^{-\frac{RSNR_{impaired}}{10}}) \quad (4.48)$$

In the case of SOP transients, an untracked change in the state of polarization rotates vectors

on Poincare sphere so that data from one polarization interferes with the other i.e. crosstalk that results in confusion of X symbols with Y symbols, and vice versa.

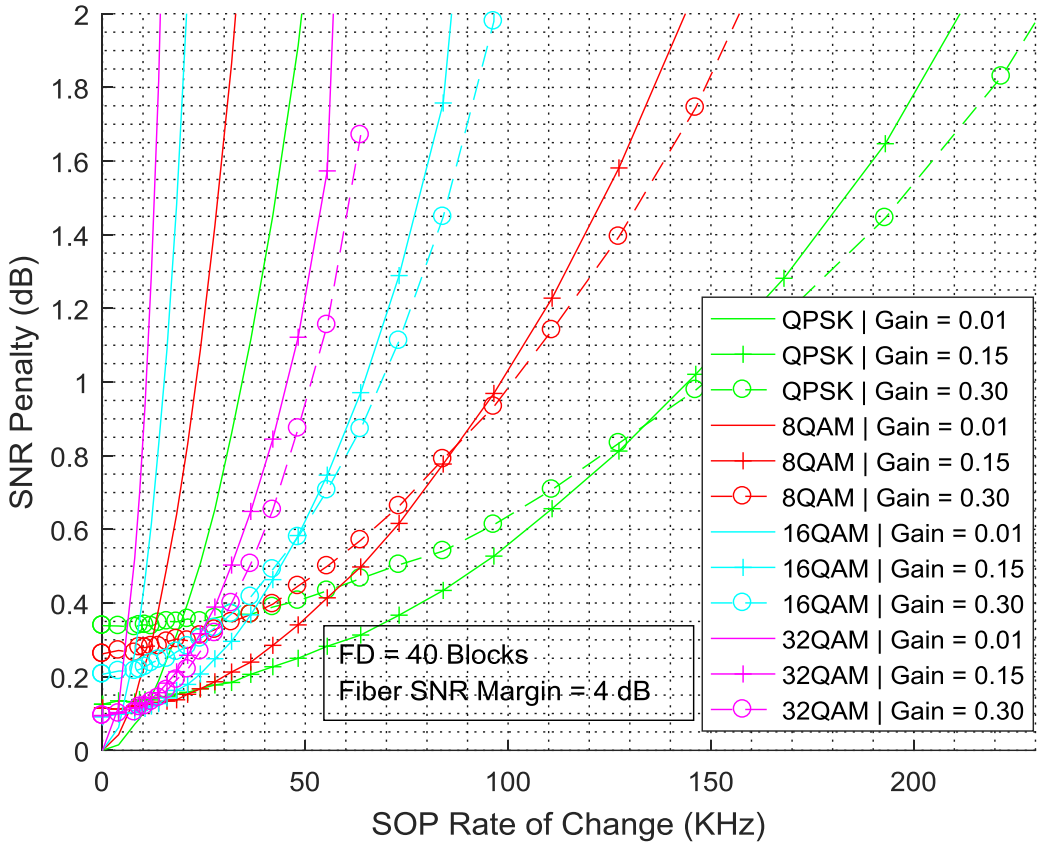

Figure 36: SNR Penalty vs SOP (versus Step Size)

4.5.1.4 - Effect of Colored Noise on Tracking of SOP Transients

Another source of impairments in optical links is the filtering effects of the concatenation of ROADMs. They are based on Wavelength Selective Switches (WSS) and can be silicon-based as presented in [78].

To study the impact of filtering on SOP tracking, we used the fiber model in Fig. 37. Noise was added for each span as it is the case in real optical links. The simulated data stream was shaped at the transmitter with Root-Raised Cosine (RRC) pulse shaped to comply with zero ISI criterion since the bandwidth is limited. The set roll-off factor chosen was 0.21, along with the mentioned baud-rate of 33 GBaud, the total bandwidth of the signal is 40 GHz. Considering it is 16QAM, it allows a line rate of 264 Gb/s (33 (GBaud) * 4 (dual polarization) * 2 (bits per baud)) without consideration of forward error control (FEC) overhead. We tested one set of filters, combined with

the transfer function of the common multiplexer/demultiplexer, to mimic 12 spans (have 6 ROADMs) optical link, with resulting effective 3-dB bandwidth of 37.3 GHz.

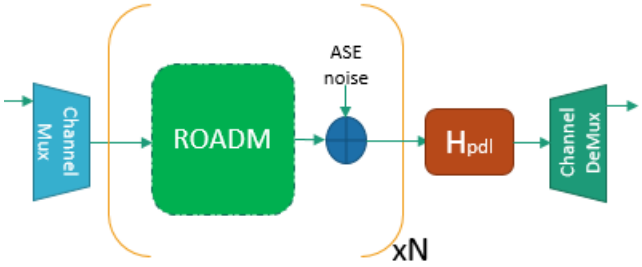

Figure 37: Simulated fiber model

In Fig. 38, we scaled all penalties to remove base due to the additional impairment; therefore at 0 KHz SOP transient, we see the penalty associated are “0”. If we did perform the scale, you would see penalty associated with adding the 12 spans model to the PDL. That is due to the receiver signal having its high frequency components attenuated by the filtering. When LMS tries to recover the data, it boosts noise as well and hence the increase in Bit-Error Rate (BER). As the rate of SOP increases, the penalty gets higher. For 12 spans/PDL = 6 dB versus PDL = 6 dB only, the penalty for SOP at 20 KHz is 0.2 dB while it is 0.4 dB at 25 KHz. Based on some fitting on the data in figure below, for each one dB PDL increase in link, we lose 7.1 KHz and 8.6 KHz for SNR penalty of 1 and 2 dB respectively. It is worth noting that in real fiber link with many filtering sites, the variability in the BER gets higher since the PDL of the link is fluctuating over time. Our observations showed that the adaptive filter taps are noisier due to increase in the feedback error during the transient, therefore the estimate even of the static portion of the fiber channel will be noisy and hence higher the penalty. When adding 10 ps of PMD along PDL of 2 dB, the increment in penalty did not exceed 0.3 dB at the highest supported SOP tracking rate (within 2 dB SNR penalty). As well, the BER variability gets higher as PDL increases, it is mainly due to upsurge in randomness of attenuation and SNR measured per polarization. Therefore, the maximum LMS step size required to assure stability gets smaller.

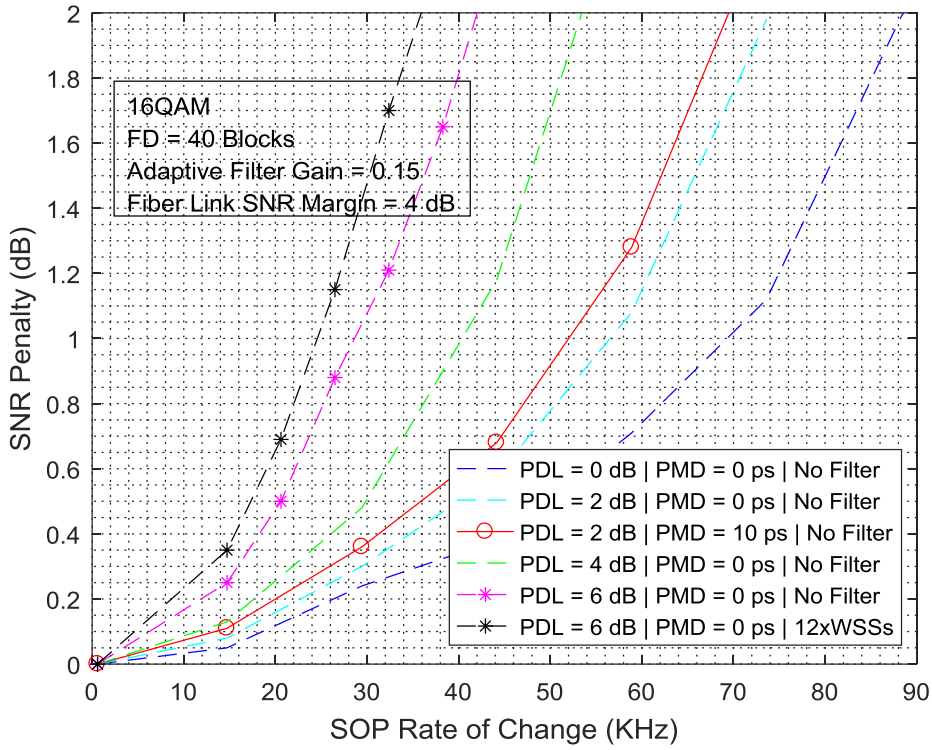

Figure 38: Penalty of SOP tracking for 16QAM for different PDL

4.5.1.5 - Tracking Transients for Different Modulation Formats

With programmable transponders being the norm in next generation Software-Defined Networks, the same hardware will be used for supporting the transmission of more than one modulation format. Therefore, it is important to study SOP tracking capabilities of one modem for various line rates. It is safe to assume that the feedback delay is the same for different modulations formats to reduce hardware footprint/complexity. However, the maximum PDL to be supported is different since the applications ranges from DCI to submarine links, as illustrated in Fig. 23. As we see below, the maximum achievable SOP tracking gets smaller when the modulation order is higher. The reason is that the Euclidian distance between nearest points is smaller for higher order modulation constellations and, as described in [91] for wireless applications, richer constellations are more sensitive to even modest amount of added noise. Assuming same fiber link SNR Margin of 4 dB for all cases and same adaptive filter gain, we show in Fig. 39, the reduction in SOP tracking capability as the number of bits per symbols increases. It is shown as well that allowing higher SNR penalty has lesser effect on SOP tracking.

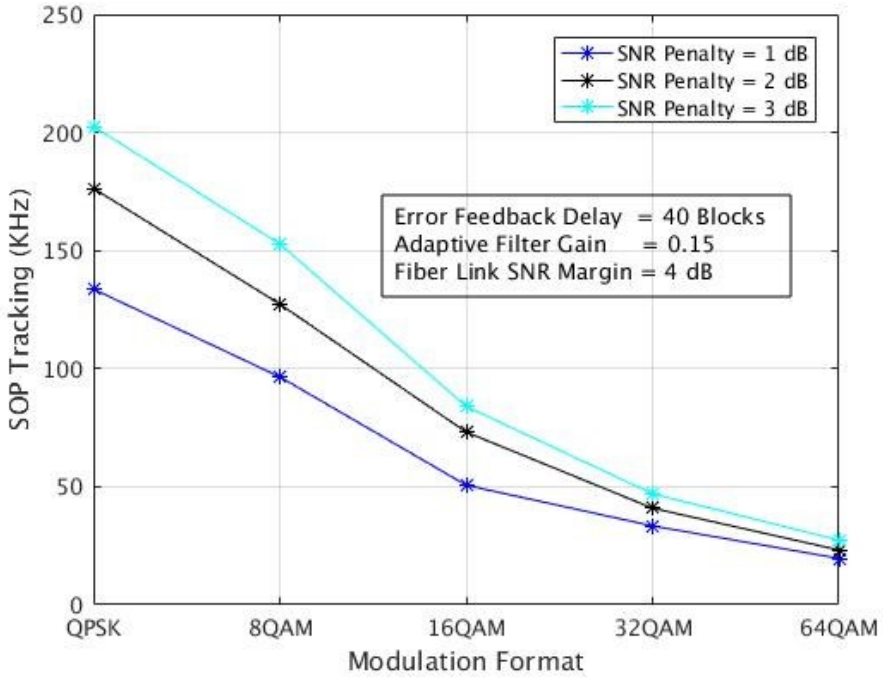

Figure 39: SOP tracking versus modulation format for different SNR penalties

4.5.3 - RLS, NLMS and LMS in presence of colored noise

In this sub-section, we compare floating-point LMS, NLMS and RLS algorithms in term of both convergence speed and steady state performance. In comparison to wireless, SOP transients in a MIMO system is unique to optical fiber communication, it does cause the channel response to become nonstationary. PDL can be compared to slow fading, while combined with SOP transient, it becomes more like “short-duration statistically non-stationary fast-fading channel”.

The authors in [92] performed a detailed study comparing RLS, LMS and sign updating algorithms in time-varying channels. It shows RLS outperforms other methods in term of excess mean-square estimation error, unless the eigenvalues of the input signals covariance matrix are equal. The later condition is not the case in presence of PDL. In [93-95], authors compared RLS and LMS in wireless context with time-varying non-stationary channels. It was shown that depending on the SNR and channel bandwidth, LMS can have a better performance with chirp-like signals. In [79], authors introduced a whitening process that can be applied post the adaptive filters to improve coherent receivers’ performance in presence of PDL. Our simulations showed that with slow variation of SOP, applying the whitening matrix prior to decision block helped reducing ROSNR. However, in presence of fast SOP fluctuation, updating the whitening matrix as quickly is challenging in practice.

4.5.3.1 - Convergence Speed in Presence of PDL

Convergence speed of adaptive filters is part of the signal acquisition process in coherent receivers. Acquisition time is a key specification in optical networks. Initialization needs to be performed each time the signal is re-routed or recovers from loss of signal. As example of the stringent limitation on recovery time, SONET protection should recovery within 50 ms as stated in the Telcordia© GR-253-Core specification [96]. In [99], it is discussed that for 5G networks the "0-Switching time" is as low as 1 ms and latency is 10x better compared to previous wireless networks generations. Since the wireless networks depend heavily on optical links for their backbone connections [95], that imposes severe requirements on the design of the next generation coherent transponders.

In Fig. 40, our Monte-Carlo simulation shows the number of blocks required for system to reach convergence (bit error rate of equivalent to steady state) as function of PDL using 16QAM as modulation format, 0.15 LMS gain (and 0.985 as RLS forgotten factor) and Link SNR Margin of 4 dB. We can see, as expected, that RLS outperforms NLMS, which is faster than LMS. Although it is accepted to assume that acquisition is not performed under fast SOP transients, that's because the latter are supposed to be a rare event. However, we tested few cases with 30 KHz; we show that even with no FD of 1, the high oscillatory behavior due to PDL and SOP resulted in long acquisition time. We can see how a FD of 20 blocks caused the acquisition time for RLS with PDL of 6 dB to double.

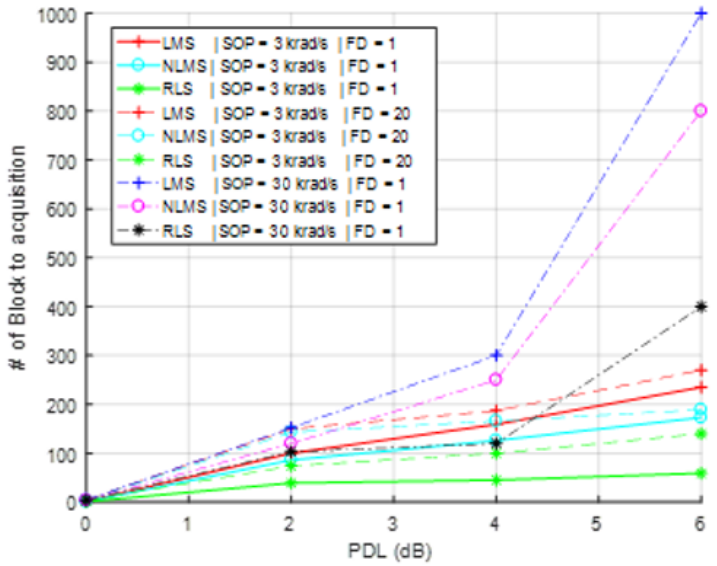

Figure 40: Number of blocks required to reach steady state versus PDL

The above results are in-line with literature [92, 96] where it is shown that the spread in the eigenvalues of the correlation matrix causes LMS to have a slower convergence speed. It is worth noting that PDL can be estimated in coherent receivers using the taps of the adaptive filters as:

$$PDL_{dB} = 20 * log10(\frac{\lambda_{max}}{\lambda_{min}}) \quad (4.49)$$

Where λ_{max} and λ_{min} are the eigenvalues of the channel inverse [61].

4.5.3.2 - SOP Tracking in Presence of PDL

As detailed in [98], even though RLS is significantly superior to LMS in term of convergence performance, the tracking in non-stationary environments must be studied on case-by-case basis. In our simulation, we observed that the ordering of PDL and the position (on fiber) of SOP transient has an impact on the capability of the adaptive filter to track. For LMS and NLMS, the impact was minimal; however, for RLS, as we will see in Fig. 41, for PDL = 6 dB, the SOP tracking capability is around 46 KHz. When flipping PDL and fast SOP, we can achieve it is 70 KHz. The reason is related to how the filter input covariance matrix is calculated. Consider the input-output relation, with bulk PDL element (**PDL**), considered between two rotating Jones matrices (**RI** and **RII**):

$$r = (\boldsymbol{RI} * \mathbf{PDL} * \boldsymbol{RII}) * s \quad (4.50)$$

Where r is the output of the fiber (received dual-polarization signal), therefore the input of the adaptive filter and s is the transmitted data. The autocorrelation of r is:

$$\begin{aligned} &= r.r^{\boldsymbol{H}} \\ &= [(\boldsymbol{RI} * \mathbf{PDL} * \boldsymbol{RII}) * s] * [(\boldsymbol{RI} * \mathbf{PDL} * \boldsymbol{RII}) * s]^{\boldsymbol{H}} \\ &= [(\boldsymbol{RI} * \mathbf{PDL} * RII) * s] * [\boldsymbol{s^H} * \boldsymbol{RII^H} * \boldsymbol{PDL} * \boldsymbol{RI^H}] \\ &= \left(\boldsymbol{RI} * \boldsymbol{PDL^2} * \boldsymbol{RI}\right) \end{aligned} \quad (4.51)$$

If R**I** is slowly rotating and R**II** in rotating quickly, the auto-correlation is not being updated fast enough for the filter to converge. On the contrary, when R**I** is in fast rotation mode and R**II** is slow, the RLS algorithm convergences much more quickly compared to LMS. In the simulations below, we are applying transient on R**II** only. In both cases, the autocorrection of the input signal(s) to the adaptive filters is still a function of the amount of PDL in the channel.

For a fixed penalty of 1.0 dB in SNR, we compare the four adaption methods when the signal

is affected by PDL. It is shown, in Fig. 41, all three methods are tracking similar SOP rate of change transient when there is no PDL. As the latter increases, the 2x2 covariance matrix of the input signal used in RLS (*P* in eq. 4.33 is an iterative estimate of the covariance matrix) or its trace used in NLMS (step size being normalized by the power of the input symbols), help with tracking SOP. In case of LMS using a fixed step size, with PDL acting as random attenuators, the tracking capability is limited as no form of "power equalization" is performed.

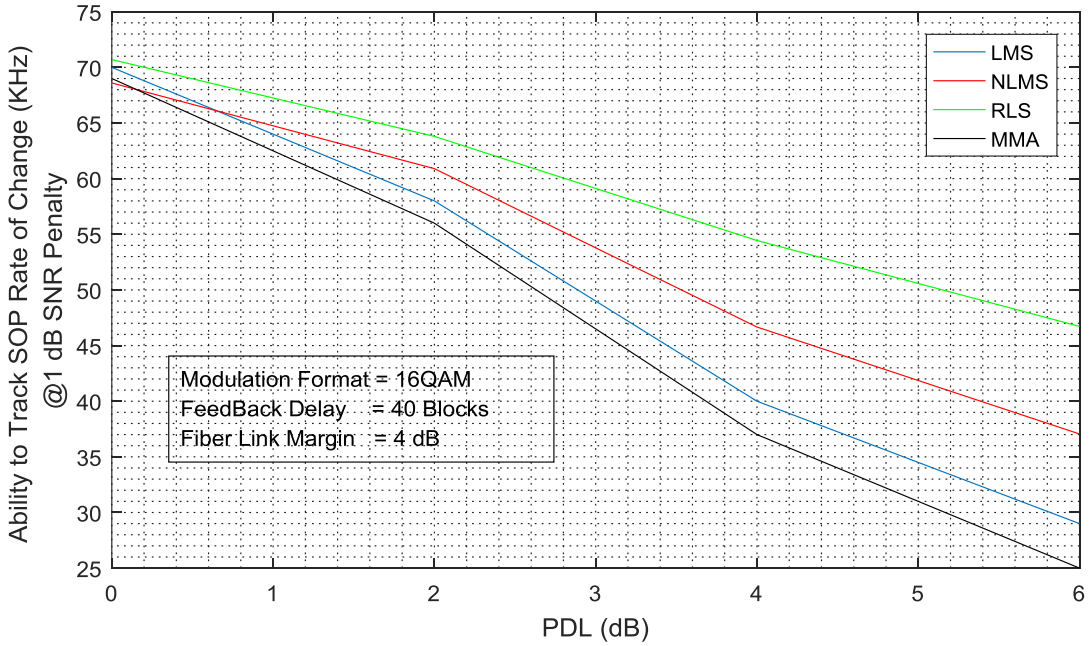

Figure 41: Achievable SOP tracking for 16QAM versus PDL

4.6 - Adaptive Gain Setting

Based on the simulation results above, we can see there is a trade-off between SOP tracking capability and ROSNR. A method for adjusting the adaptive filter gain based on user defined link condition (or modem itself using fuzzy logic to set the condition) can be used. Such method, using flow below, would fit well into SDN strategy of zero-touch network. SOP transient-related traffic hit can be monitored similar to what is described in [61] for PDL.

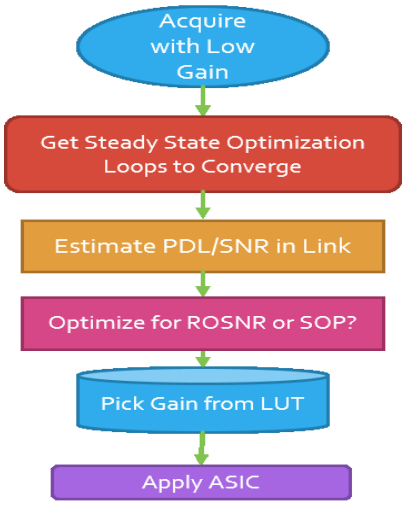

Figure 42: Flow of adaptive gain setting

4.7 - Conclusion

We studied the performance of LMS adaptive filter, in the context of dual-polarization coherent optical receivers, in presence of SOP transients, PDL and ROADMs. The trade-off between tracking capability and implementation noise when choosing the step size and forgetting factor is a key design/modem integration decision. We showed how the higher the step size the more SOP tracking the adaptive filter will be handling but at the price of higher B2B/PDL ROSNR. The higher the order the modulation formats the less tracking can be done, a reduction of 30% is expected for an increase of one bit per symbol. Error signal feedback delay is a key bottleneck for higher SOP tracking, we showed due to higher BER oscillatory behavior that a delay of 40 blocks of 512 symbols can reduce tracking by 50% compared to FD of 20 blocks. As well, for each one dB PDL increase in link, we lose 7.1 KHz and 8.6 KHz for SNR penalty of 1 and 2 dB respectively. We presented the impact of concatenating ROADMs on SOP tracking. The RLS algorithm, using a covariance matrix as an aggressive dynamic “step size”, has an advantage over the LMS and NLMS algorithms in both convergence speed and tracking in steady state in presence of PDL in the fiber. MMA is comparable to LMS in term of implementation complexity, however, it can have a lower feedback delay. As expected, for same error signal feedback delay, the blind MMA is a bit noisier than decision directed LMS and hence the SOP tracking capability is lower. However, unlike NLMS and RLS where the adaptive algorithm gain is constant, the introduction of PDL decreases the SOP tracking capability faster.

Chapter 5 - Adaptive Pre/Post-Compensation in Coherent Optical Transponders of Cascade Filters

"First and best victory is to conquer self." — Plato

5.1 – Introduction & Literature Review

THE deployment of optical switches, such as reconfigurable optical add drop multiplexing (ROADM), was a key milestone in enabling all-optical transmission, as illustrated in Fig. 43, from source to destination in a dense wavelength division multiplexing (DWDM) network. They offer great advantages for service providers such as simplification of network planning and provisioning, reduction in infrastructure cost and lower power consumption (no electrical to optical, and vice-versa, conversion required). Each optical link is split into sections called spans. The latter are characterized by the position of ROADM nodes, one every two fiber spans. Hence, the number of crossed ROADMs (Each ROADM is built with two Wavelength Selective Switch (WSS), a multiplexer and demultiplexer) is equal to half the number of spans. The length of fiber per span are in the range of 80 to 160 km depending on amplification technology used [100].

With flexibility being a requirement in current and future optical networks, ROADMs, which are made using Liquid-Crystal on Silicon (LCOS) [101] or Micro-Electro Mechanical Systems (MEMS) [102] with optical switch fabric, allow control to be done per wavelength both in terms of routing and attenuation. "Broadcast and Select" and "Route and Select" are two main architectures based on ROADMs discussed in [103].

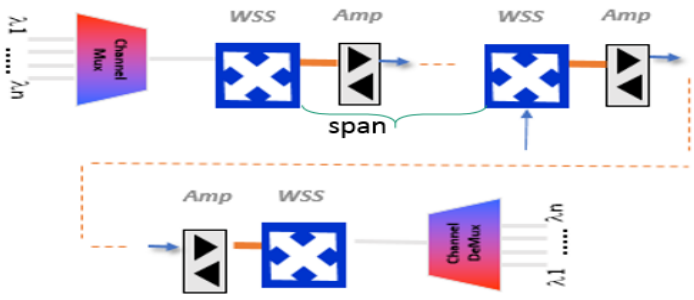

Figure 43: ROADMs in typical networks configuration

ROADMs, acting like filters with limited passband bandwidth, are critical limitations in fixed-grid optical networks [104]. They introduce colored noise to the signal while affecting both the amplitude and the phase of the propagated stream of optical pulses. The system impact of

concatenated filtering on 28 Giga-baud (Gbaud), using dual-polarization (DP) 8QAM constellation, was discussed in [105]. Both passband bandwidth narrowing and ripples are discussed in [106]. The mentioned effects get accumulated by the concatenation of multiple ROADMs as the signal travels from the source to destination across the network. The dispersion introduced and the spectral clipping on the edges are major causes of performance degradation. Currently deployed ROADMs have fixed-bandwidths of 50 and 100 GHz per wavelength. Deployment of next generation flexible-bandwidth, enabling flex-grid networks, with a granularity of 6.25 GHz is under-way [107]. That along with temperature affecting the frequency response of the EO at both the transmitter (Tx) and receiver (Rx), will cause an overall filtering effect that should be compensated for to minimize penalty imposed on signal-to-noise ratio (SNR).

To compensate for the filtering frequency dependent loss, as illustrated in Fig. 44, the authors of [108, 109] discussed applying a pre-compensation at the Tx of a 10G optical transponder. It is assumed that the transfer function of the channel is measured and available to use. In [110,111], authors studied the impact of pre-compensation, using finite impulse response (FIR) filters at the digital to analog converter (DAC), of the narrowing of bandwidth due to gridless ROADMs. The method assumes the knowledge of the number of WSSs in the link and the center frequency offset.

In [112], authors introduced new hardware (HW) block, a trellis decoder, at the end of the Rx processing chain. The solution requires extensive number of gate counts and cause higher power consumption. In [113], authors suggested to use external optical wave-shapers at edge of the DWDM link. The concept is similar to Dispersion Slope Compensation module, described in [114], that deals with compensating for chromatic dispersion per span along the link. However, beside the cost, maintenance and power consumption of new modules in link, the shapers have to be programmed for initial deployment. which makes network planning more burden but will lack continuous track of changes in transfer frequency response due to temperature or drift in center frequency when MEMS' mirrors ages. In [115], time-domain hybrid modulation used to reduce the gap between the required optical-signal-to-noise ratio (OSNR) of regular M-QAM constellations, therefore provides flexible line-rate transmission. Authors presented super-symbols as combination of 8QAM and 16QAM and showed that, as expected, hybrid modulations perform in between the two even when propagating through heavily filtered channels.

In this chapter, we present a new method that uses existing HW blocks in a typical coherent

Rx, to reduce the Required-OSNR (ROSNR) of an optical link in the presence of ROADMs filtering. The contribution of the paper is detailed in section 5.2. The models used for the filtering and architecture of typical dual-polarization coherent Rx are illustrated in section 5.3 and 5.4, respectively. In section 5.5, we will show the mathematical derivation of the proposed gradient-descent based method. The flow covering both acquisition and steady state operations of the Rx is presented in Section 5.6. The channel model and simulation environments are described in section 5.7. In section 5.8 and 5.9, the method is validated through both simulation and lab experiment.

5.2 – Chapter Contribution

We propose a new method that uses typical hardware blocks in coherent optical transponders and system-level feedback loop to continuously optimize both Tx and Rx FIR filters based on estimated signal to noise ratio (SNR) at the Rx. The method does not imply any extra power consumption, compared to other methods using power consuming time domain FIR or trellis decoders. As well, we present an algorithm to cover both acquisition and steady state operations, to give chance for Rx to acquire even if communication with Tx is not established yet.

With software defined networks being designed, providers are moving to automated, zero-touch and zero-provisioning optical networks [116]. Carrier grade requirements are focused on features such automatic rerouting [117] and adaption of line rate based on available OSNR on the link [115]. Having said that, a back channel between Tx and Rx will be a must in current and next-generation intelligent transponders. The feedback communication can be done using an optical service channel, if available in the network. Otherwise, since the vast majority of optical fiber deployments are duplex, a software-based feature which inserts information to communicate back to Tx as part of the frame load once every certain number of frames (based on bandwidth of the loop) can be used. The loop bandwidth is very small therefore the overhead required is negligible compared to capacity of the link. Since the variation of filtering effects are quasi-static (changes very slowly in time versus temperature and aging), we can capture the estimate and send it back to Tx even in the presence of propagation delay. In our case, 256 coefficients, each of 10 bits, required to be exchanged between Tx and Rx every 10 seconds; which adds a very small overhead. The challenge is that feedback loop won't work with modems required to support interoperability from different vendors, unless it is standardized in Optical Internetworking Forum (OIF).

With the introduction of colorless channel mux/demux (CMD), new ROADM-based architectures described as Colorless-Directionless-Contentionless (CDC) mux/DeMux are heavily deployed in nowadays' mesh networks [118]. The latter may have more than hundreds of light-paths [119] and deploy multi-degrees ROADMs, up to 8 degrees using WSSs with 43 ports as in presented in [120], per site where any tunable Tx can be connected to any colorless CMD port. Having said that, pre-setting the correct pre-equalization transfer function or programming FIR filter taps properly takes an enormous effort and its prune to mistakes. Since only the Rx can estimate the channel response, any automated method requires feedback channel.

Beside gain in ROSNR as presented in section VIII and IX, splitting the compensation offers many advantages. Based on what we demonstrate in the results, in most cases, only 70% of worst-case peaking to pre-compensate for concatenated filters, EO and data converters frequency responses is to be performed in the Tx. Such system information provides guidance for designers of various digital and analog blocks in both Tx and Rx of coherent modem, as we explain in the three points below:

1. The ability to do pre-compensation, i.e. applying peaking to high frequencies, is dependent on the effective number of bits (ENOB) of the DAC. Per example, each 6 dB to pre-compensation requires 1 bit of ENOB, which requires four times more power consumption [121]. Therefore, splitting the compensation helps relaxing the ENOB requirement of the DAC.

2. With next generation transponders aiming for 600Gb/s with high baud-rate, 84 GBaud was presented in [122], the analog driver of the optical modulator requires to have a large bandwidth. Our method helps relaxing the design requirement since the frequency response does not have to be wide to let through all the peaking at high frequencies.

3. Continuously moving the compensation of the static portion of the channel, such as chromatic dispersion as in [29], from the adaptive filter to the static filters of the Tx and Rx, allows some of the adaptive filters taps to deal with more dynamic impairments of the optical link such as polarization mode dispersion (PMD) and polarization-dependent loss (PDL).

4. Reducing the impact of noisy, i.e. high intrinsic jitter profile, phase locked loop (PLL) at data converters in the Tx. As we illustrate in appendix B, jitter impact on sinusoidal tones gets higher as frequency increases. Therefore, the more peaking performed at the Tx, i.e. increasing the magnitude of component, the higher the SNR penalty due to jitter.

5.3 - Modelling of ROADMs Concatenation

With fixed-grid switching elements, WSSs and CMDs, being built with different technologies, as well with diverse manufacturing variations and large number of suppliers [119], the predictability of the frequency response and center frequency shift of the concatenation of all the filtering effects is a challenge. In literature, the distribution of center frequency offset varies from the range of (-1,+1) GHz [11] to (-4,+4) in [119]. While in [123], the characterization of 96 CMD instances built with arrayed-waveguide gratings (AWG) technology, showed a variation of +/- 5 GHz around channel nominal frequency. As well, each the insertion loss per port varies and alter the shape of the propagated waveform. As presented in [124], each WSS port can be modelled as super-Gaussian and is specified by two parameters: 3dB frequency width (σ_{sg}) and order (n):

$$S_{sg}(f) = \frac{1}{\sigma_{sg}\sqrt{2\pi}} \exp[-(\frac{f^2}{2\sigma_{sg}^2})^n] \qquad (5.1)$$

For our simulations and lab testing, we got the frequency response of the aggregation of 18 commercial 50 GHz fixed-grid WSSs and one set of worst case Mux/Demux of a 50 GHz fixed grid CMD. The responses showed in Fig. 44 include some ripples in the passband. The phase response was ignored for two reasons: one is that the concatenation of filters causes a reduction in the phase ripple variance, second is that the adaptive filter can correct for that with no penalty. Unlike the work done in [110], we are not covering power loss, so we normalized the root-mean square (RMS) of the signal is in simulation, while in the lab experiments, the erbium-doped fiber amplifier (EDFA) was set in power-mode to keep received power the same. The latter was chosen so RMS of received signal is in the optimum spot for the analog-to-digital converter (ADC).

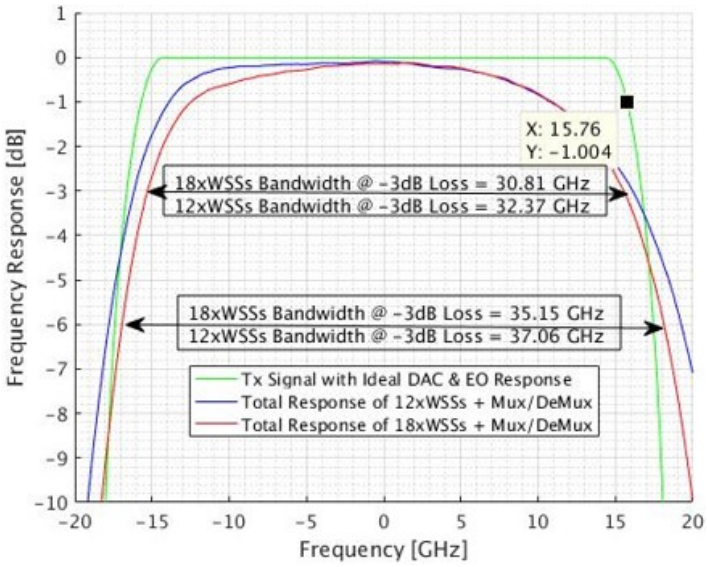

Figure 44: Signal with RRC pulse shaping and Ideal DAC/EO, as well, the two models used in simulation/experiment showing reduction in bandwidth due to cascaded 50GHz ROADMs

5.4 - Typical Blocks in Coherent Receiver

In Fig. 45, we illustrate the typical blocks in coherent transponder. In the Tx, data streams are encoded then filtered with static filter (CD EQ_x/y). The latter can be used for two purposes: pulse shaping (such as root-raised cosine (RRC)) to help reducing inter-symbol interference and dispersion pre-compensation. It is shown in literature [24] that splitting the dispersion compensation between Tx and Rx improves performance in presence of nonlinearity, such as in long-haul propagation. Tx/Rx Firmware (FW) blocks are the software used to provision the digital and Electro-Optics (EO) of modems.

Dual-polarization optical signal is split and mixed with the output of a local oscillator at the Rx to generate four branches (X/Y polarizations, each has in-phase and quadrature field). The data is digitized using an ADC then goes to digital signal processing blocks. Similar to the Tx, the Rx side the static filter (CD EQ_x) is used for matching the Tx filter to maximize SNR and it is used for dispersion post-compensation. Typically root raised cosine (RRC) are used in both Tx and Rx to form a raised cosine to minimize inter-symbol interference (ISI). It is typical that the bulk part of dispersion is compensated prior to symbols reaching the butterfly MIMO equalizer. The latter is the core of the Rx and it is adaptive, where Constant Modulus Algorithm (CMA) and Least Mean Square (LMS) are examples of the adaptive method used, [125], to decouple the two polarizations and compensate for linear time variant channel impairments such as Polarization Rotation, Polarization Mode Dispersion (PMD) and Polarization Dependent Loss (PDL).

Impairments such as residual dispersion, filters passband ripples and edges roll-off are static; they can be estimated using the common factor of the four Multi-Input Multi-Output (MIMO) filters. In [126], the use of common response was introduced to remove some of the residual dispersion from the adaptive filter and transfer them to the static filter to increase the Rx tolerance of PMD. In our case, instead of using the phase of the common response, we will use the magnitude to help mitigate the filtering effects. Frequency and phase offsets, between Tx and Rx laser oscillators, are tracked by carrier recovery block using methods such as Viterbi-Viterbi [127]. Symbol decoding, or de-mapping, and forward error correction (FEC) work together to extract and correct the sent stream of bits from the received symbols. As described in [128], they both can be based on soft-decision, such likelihood metric, or hard-decision.

The 2x2 MIMO equalizer matrix can be represented as:

$$H(f) = \begin{pmatrix} H_{xx}(f) & H_{xy}(f) \\ H_{yx}(f) & H_{yy}(f) \end{pmatrix} \qquad (5.2)$$

With the common response equal to (we want to do enough averaging to get a good estimate), as shown in [29]:

$$Hc\ \ (f) = \sqrt{H_{xx}(f) * H_{yy}(f) - H_{xy}(f) * H_{yx}(f)} \qquad (5.3)$$

With no impairments, such as frequency selective loss and dispersion, the symbol arrives at the Rx within its “dedicated” interval. Otherwise, we see ISI effect where the transition of the symbols scatters to the neighbor intervals. Digital compensation is basically applying different weights and delays, i.e. filtering, to undo the expansion caused by neighboring symbols over the symbol of interest. The size of the filters required depends on the characteristic of the channels. In the frequency domain, the compensation is mainly pre-emphasizing high-frequency components of the data stream. Beside ROADMs, data converters (ADC/DAC), driver and optical modulator can have some roll-off at high frequencies [129]. In [130], it is mentioned that DAC frequency response at 80% of Nyquist sampling frequency, the output amplitude is attenuated by 2.42dB.

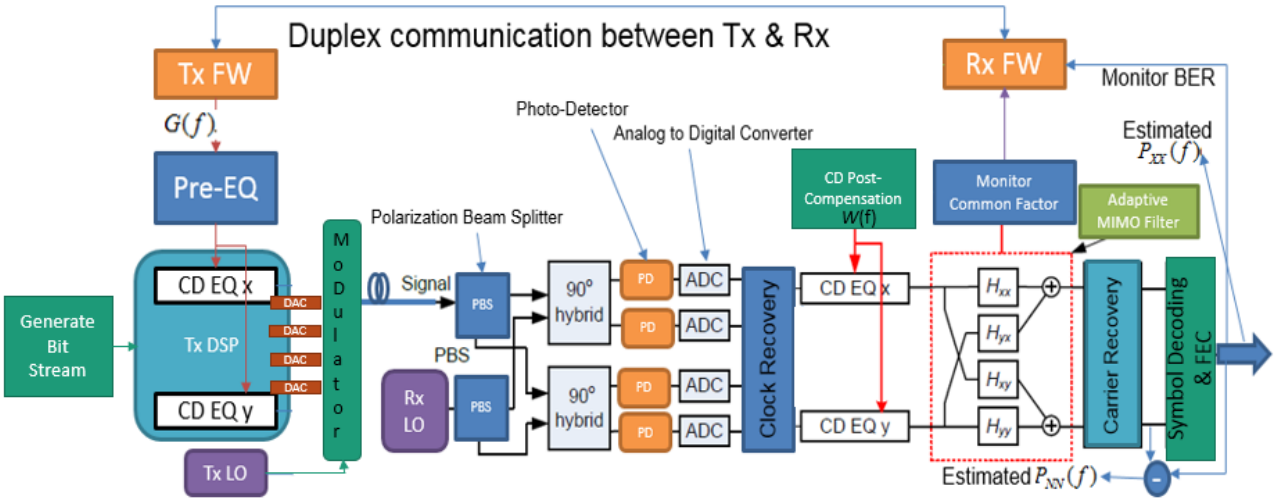

Figure 45: Block diagram showing key functional blocks in coherent optical transponder and requirements for the operation of the presented method

Here we demonstrate how the amplitude of the common response $H_c(f)$, presented in Eq. 3, is capturing the quasi-static frequency-dependent ripple and loss from output of Tx DAC to the input of Rx ADC. In a lab experiment, with commercial card, we captured the four vectors of FIR filters taps ($\boldsymbol{H}_{xx}/\boldsymbol{H}_{yx}/\boldsymbol{H}_{xy}/\boldsymbol{H}_{yy}$) 50 times, with five ms period, as shown in Fig. 46. The latter illustrates how consistent is the common response in estimating the static frequency response, both phase and amplitude. Since the filters response has intense drooping at high-frequencies, and there is a frequency offset to that emphasizes one side, we can see more peaking about 5 dB on the high positive frequencies compared to negative ones. In the mid-range of the frequency response, the ripples are compensating for both the ripples in channels and the residual ripples from Tx EO/Rx EO/DAC/ADC calibrations.

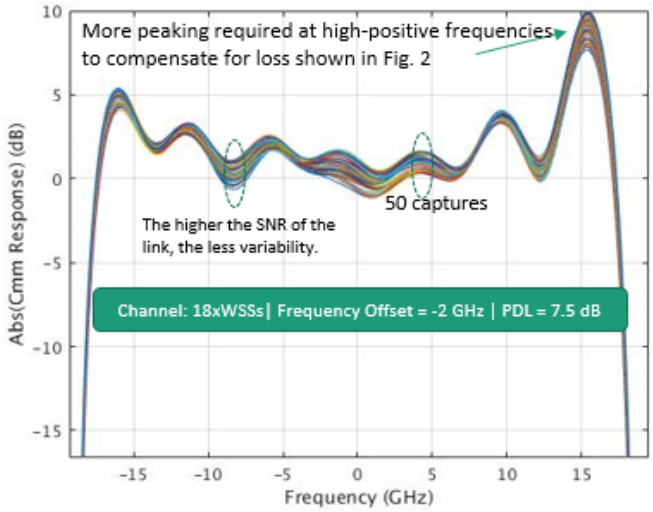

Figure 46: Common response of the adaptive filter after convergence

The average of the retrieved common responses of three different scenarios, displayed in Fig. 47, are used in the optimization process. The approximation of the shift in the center frequency, from the ITU (International Communication Union) center frequency, is embedded in the estimated frequency response; it is visualized when comparing blue and red curves below. The x-axis is the index of the frequency bins used in the operation, they are mapped to -20 to +20 GHz, i.e. +/- sampling frequency/2 (Fs/2).

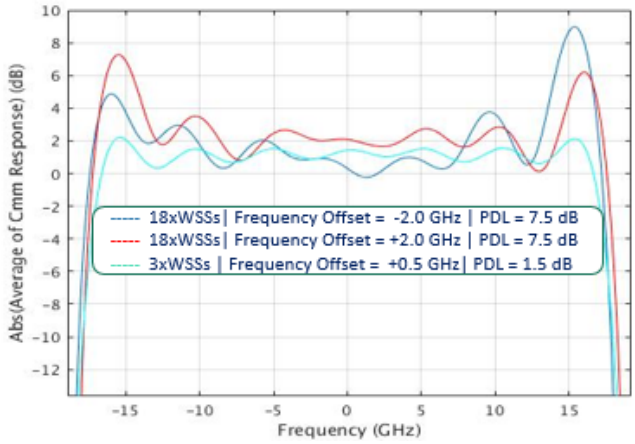

Figure 47: Magnitude of common response for link scenarios

Since PDL accumulates in a link mainly due to birefringent elements, such as mechanical stress or variability in the manufacturing process as described in [131], and Wavelength Selective Switches (WSS), as detailed in [132]; therefore, we modeled the maximum PDL in association with filtering.

5.5 - Mathematical Analysis

In this section, using zero-forcing compensation approach how splitting compensation yields a higher SNR at the Rx. We will, then, present our proposed iterative-based method that operates on frequency-domain coefficients of both Tx and Rx filters. Last but not least, we will show that under the same constraints, a closed-form solution exists.

5.5.1 – Zero-Forcing Joint-Compensation

Consider the simple system below with vector $\boldsymbol{G}$ is the magnitude of frequency-domain pre-compensation filter at the Tx, before the DAC, and vector $\boldsymbol{W}$ is the post-compensation filter. *n* is the white Gaussian noise of the channel, $\boldsymbol{N}$ is the Fourier transform and its power spectrum

density is defined as $\boldsymbol{P_{nn}}$. Vector $\boldsymbol{Hc}$ is the frequency response of the quasi-static impairment in the channel. The sent signal, $\boldsymbol{s}$, is assumed to have zero-mean and variance σ.

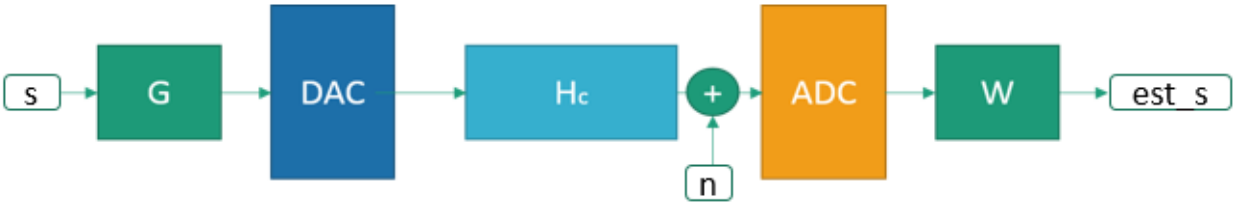

Figure 48: Simplified system model

Under zero-forcing constraint, the following product should be equivalent Nyquist impulse response:

$$G(f) * Hc(f) * W(f) = 1 \qquad (5.4)$$

Then

$$W(f) = \frac{1}{G(f)*Hc(f)} \qquad (5.5)$$

The transmitter output power is given by, with T sampling time:

$$p_0 = \frac{\sigma^2}{T} \int_{-Inf}^{+Inf} |G(f)|^2 * \frac{df}{2*pi} \qquad (5.6)$$

The minimum square error is defined as:

$$\varepsilon = E|e(j)|^2 \qquad (5.7)$$

$$e(j) = est\_s(j) \quad - s(j) \qquad (5.8)$$

When solving the problem from zero-forcing perspective, the error seen by the receiver is due to noise n going through the receiver filter $\boldsymbol{W}$ in time-domain:

$$e(j) = \int_{-Inf}^{+Inf} w(\tau) * q(jT - \tau)\, d\tau \qquad (5.9)$$

Assuming q complies with wide-sense stationarity stochastic processes, the mean square value is equivalent to:

$$\varepsilon = \int_{-Inf}^{+Inf} P_{nn} * |W(f)|^2 * df/(2 * pi) \qquad (5.10)$$

Replacing $W(f)$ from (5.5):

$$\varepsilon = \int_{-Inf}^{+Inf} P_{nn} * \left|\frac{1}{G(f)*Hc(f)}\right|^2 * df/(2 * pi) \qquad (5.11)$$

Using expression above, multiply by:

$$\left(\int_{-Inf}^{+Inf} |G(f)|^2\, df\right)$$

Then establish Cauchy-Schwartz inequality:

$$\left(\int_{-Inf}^{+Inf} P_{nn} * \left|\frac{1}{G(f)*Hc(f)}\right|^2 * \frac{df}{2*pi}\right) * \left(\int_{-Inf}^{+Inf} |G(f)|^2\, df\right) \geq \left(\int_{-Inf}^{+Inf} P_{nn}{}^{1/2} * \frac{1}{Hc(f)}\frac{df}{2*pi}\right)^2 \qquad (5.12)$$

Now considering the set constraint on output power, eq. 5.6, we have:

$$\left(\int_{-Inf}^{+Inf} P_{nn} * \left|\frac{1}{G(f)*Hc(f)}\right|^2 * \frac{df}{2*pi}\right) \geq \sigma^2\left(\int_{-Inf}^{+Inf} P_{nn}{}^{1/2} * \frac{1}{Hc(f)}\frac{df}{2*pi}\right)^2 / (T * p_0) \qquad (5.13)$$

The equality is achieved when the two integrands in eq. 5.12 are related by a scalar. The pre-compensation filter $\boldsymbol{G}$ is optimized to:

$$G(f) = K_{pre} * \frac{1}{Hc(f)^{\frac{1}{2}}} * (P_{nn}(f)^{1/4}) \qquad (5.14)$$

And the post-compensation is derived as:

$$W(f) = K_{post} * \frac{1}{Hc(f)^{\frac{1}{2}}} * (P_{nn}(f)^{-\frac{1}{4}}) \qquad (5.15)$$

With K_{pre} estimated to comply with equation (5.6), then K_{post} can be derived from the equality of (5.13). As in our case with bandlimited channels, the Inf is replaced by Baud-Rate/2 for channels with no excess bandwidth, i.e. T-spaced channels. For the case of white noise, $\boldsymbol{P}_{nn}$ is a constant; therefore, then $\boldsymbol{G}$ and $\boldsymbol{W}$ constitute a pair of matched filter.

5.5.2 – Proposed Iterative Method

Zero-forcing splitting would not consider noise profile. We propose an iterative, gradient-descent, MMSE method. Without power constraint, pre-shaping data only at the Tx would give the best performance since noise has not yet been introduced. However, in practice, transceivers operate with total power constraint over the signal spectrum.

$$P_{ch} = \frac{\sum_{f=Freq\ Start}^{Freq\ Stop} 10^{\frac{FFTBin(f)}{10}}}{Window\ Bandwidth} \quad (5.16)$$

We propose a new method to do the joint compensation that takes into consideration the power limitation at the output of the Tx. It is a gradient-descent approach which involves a valid communication taken place between the Tx and Rx to transfer the estimated pre-emphasis spectrum, while all computations can be done at the Rx. The communication can be done using a service channel or as part of the data overhead. In this paper, we only look at compensating for the magnitude response only.

First, we consider the Weiner solution, [42, 43, 133], in an adaptive equalization context. Once steady state is reached, the MIMO adaptive filter at the coherent Rx converges to a near-Wiener solution. Since both polarizations go through the same filtering effect, we can use one of them in our procedure. In frequency domain, the input of the adaptive filter of the Rx is:

$$Y(f) = S(f)G(f)H_c^{-1}(f) + N(f) \quad (5.17)$$

Where ***S*** is frequency-domain (Fourier transform) representation of the decoded symbols (at the input of the FEC), representing the estimate of transmitted symbols, and its power spectrum density is defined as $\boldsymbol{P_{ss}}$. ***Y*** is the Fourier transform of the received symbols at the input the receiver filters. $\boldsymbol{H_c}$ is the estimate of the static portion of channel frequency response. ***G*** is the frequency domain of pre-compensation coefficients. *n* is the additive noise, ***N*** is the Fourier transform and its power spectrum density is defined as $\boldsymbol{P_{nn}}$, estimated from the error used in the adaptive filters coefficients update. We can show that the optimal Wiener equalizer [36, 37] in the frequency domain, ***W***, is given by the following equation, with * conjugate operator:

$$W(f) = \frac{P_{ss}(f)G^*(f)\,(H_c^{-1}(f))^*}{P_{ss}(f)|G^*(f)\,H_c^{-1}(f)|^2 + P_{nn}(f)} \quad (5.18)$$

The goal is to minimize the mean square error (MSE) over the M (= 256 in our case) frequency bins. We define *F* as:

$$F = \sum_{i=1}^{M} E\left\{\left(W(f_i)Y(f_i) - X(f_i)\right)^2\right\} \quad (5.19)$$

Rearranging (5.19), we get:

$$F = \sum_{i=1}^{M} \frac{N}{\left|Hc^{-1}(f_i)\, G(f_i)\right|^2 + N} \qquad (5.20)$$

Then gradient descent approached can be used, with μ defined as the step size. We picked a small value equal to 0.1 considering the slow dynamic of moving elements (such as the variability of total transfer function of modem' Eos and cascaded WSSs over temperature):

$$G(f_i) = G(f_i) + \mu * \frac{\partial F}{\partial G(f_i)} \qquad (5.21)$$

Normalization is required due to the total optical power constraint at the output of the Tx:

$$G(f_i) = \frac{G(f_i)}{\sqrt{P_{ch}}} \qquad (5.22)$$

Finally, $W(f_i)$ can be derived based on (5.18).

5.5.3 – Closed-Form Proof Approximation

The error power spectrum, due to channel noise *n* in Fig. 48, after the optimal post-compensation Wiener solution presented in (5.18):

$$P_{ee} = \frac{P_{ss}(f)\, P_{nn}(f)}{P_{ss}(f)\, |H_c(f)\, G(f)|^2 + P_{nn}(f)} \qquad (5.23)$$

Knowing that the P_{ch}, introduced in eq. 5.16, is equal to:

$$P_{ch} = \frac{1}{2\pi} \int_{-\pi}^{\pi} P_{ss}(f)\, |G(f)|^2\, df \qquad (5.24)$$

And let's define

$$\beta = |G(f)|^2 \qquad (5.25)$$

Lagrange optimization method allows minimizing *f* function of β, subject to constraint on function *g* (in our case, equal to P_{ch}), by introducing variable λ (Lagrange multiplier) and finding the critical points of Lagrangian function:

$$L(\beta) = f(\beta) - \lambda\, g(\beta) \tag{5.26}$$

Therefore,

$$L(\beta) = \int_{-\pi}^{\pi} \frac{P_{ss}(f)\, P_{nn}(f)}{\beta\, P_{ss}(f)\, |H_c(f)|^2 + P_{nn}(f)} \frac{df}{2\pi} + \lambda \left(\frac{1}{2\,\pi} \int_{-\pi}^{\pi} P_{ss}(f)\, \beta\, df - P_{ch}\right) \tag{5.27}$$

Looking for optimal β by setting the condition

$$\frac{\partial L(\beta)}{\partial \beta} = 0 \tag{5.28}$$

We get

$$\frac{P_{ss}(f)\, P_{nn}(f)\, |H_c(f)|^2}{(\beta\, P_{ss}(f)\, |H_c(f)|^2 + P_{nn}(f))^2} = \lambda \tag{5.29}$$

Solving for β, gives us the pre-compensation filter:

$$G(f) = \sqrt{k \sqrt{\frac{P_{nn}(f)}{P_{ss}(f)\, |H_c(f)|^2}} - \frac{P_{nn}(f)}{P_{ss}(f)\, |H_c(f)|^2}} \tag{5.30}$$

5.6 - Flow of Software Automation

The high-level software implementation can be segregated into the following steps shown in Fig. 49. Once the provisioning of lasers with proper wavelength and initialization of Application-Specific Integrated Circuit (ASIC) are complete, the signal processor at the Rx will begin the acquisition process.

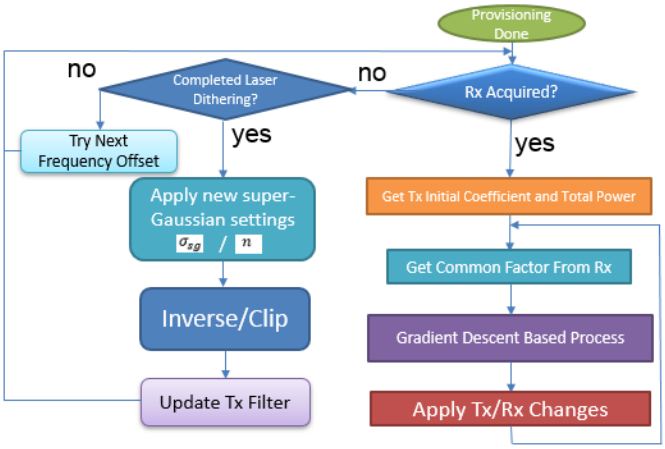

Figure 49: Flowchart of the steps proposed for by software to perform the optimization

Assuming dispersion compensated link, or both Tx and Rx are provisioned with proper digital dispersion compensation settings, the Rx will sweep the frequency around the provisioned ITU wavelength to get the frequency offset between the Tx and Rx local oscillators to within carrier recovery acquisition range (+/- 1.1 GHz for 16QAM as in [134], which not to be confused with shift in center frequency of the channel model). If the search for frequency is complete and acquisition did not occur yet, we propose a blind pre-compensation sweep to help increase the total SNR at the input of the adaptive filter. Updating the Tx filter, causes peaking at high frequencies, as shown in Fig. 50, and is generalized as follow:

$$H_{Tx}(f) = H_{RRC}(f) * H_{CMD}^{-1}(f) * |S_{sg}^{-1}(f)| \tag{5.31}$$

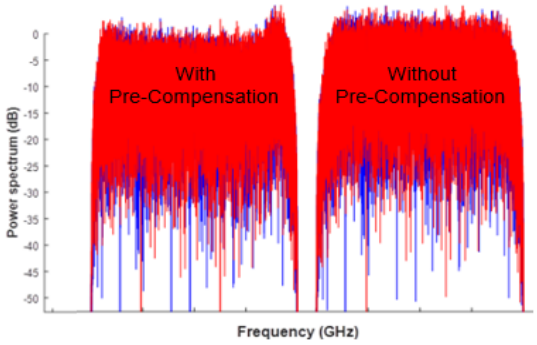

Figure 50: Example showing spectrum at Tx with & without pre-compensation

If SNR improvement achieved, when performing the sweep of super-Gaussian parameters, reaches the level required for acquisition, then Rx will acquire. If dispersion is not known, or links are not equipped with dispersion slope compensation modules, then scanning for dispersion is required for every steps. Blind maximum likelihood methods, such as described in [135], can be added to the software flow. The algorithm was tested with an extreme link condition of 15 spans, i.e. 15 Mux + 15 Demux WSSs, case where the receiver of a commercial and calibrated card was not acquiring. With filter order in Eq. 5.1 set to 5, the sweeping of 3-dB bandwidth resulted in an improvement of SNR by more than 0.4 dB which enabled the receiver to acquire, as illustrated below.

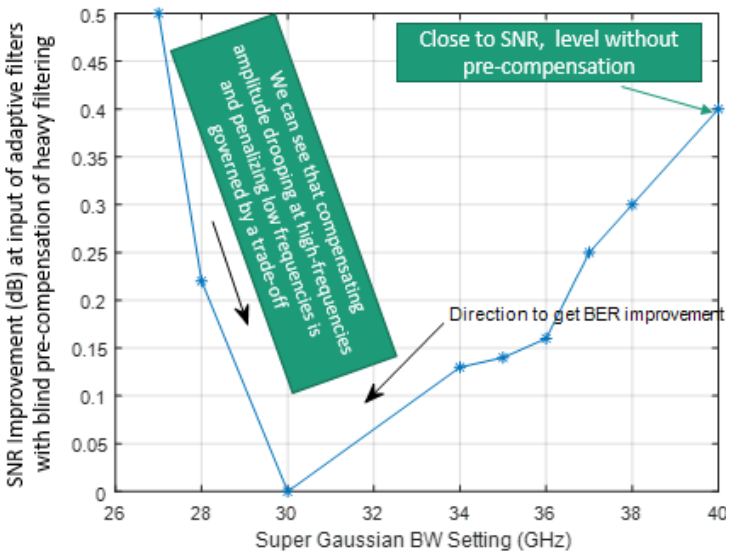

Figure 51: ROSNR penalty versus 3dB bandwidth of super-Gaussian model of WSSs in link when blindly sweeping parameters to achieve signal acquisition at the Rx.

Once acquisition is achieved, the flow to optimize both Tx and Rx, is triggered. In Fig. 52, we show how much peaking at high-frequencies (more than 10 dB) is performed by the adaptive filters at the Rx then the spectrum becomes flat since the static portion of the adaptation is moved to both Tx and Rx static filters.

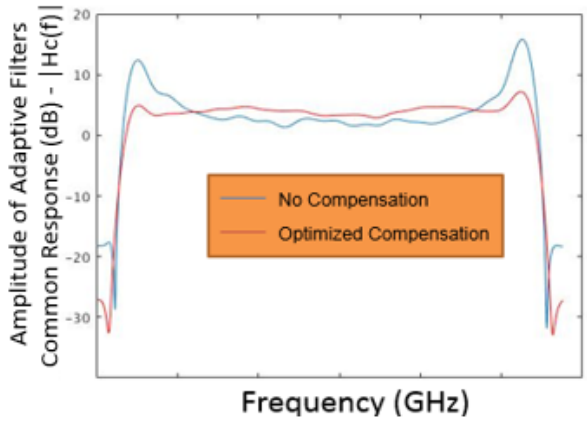

Figure 52: Absolute value of the amplitude of the common response of the Rx adaptive filters

5.7 - Simulation Setup

All simulations were conducted using Matlab 2016b©. Fig. 45 is, as well, an overview of the block diagram of the DSP elements used in simulation to evaluate the methods proposed in this paper.

The modulation format of choice was 16QAM with the signal baud-rate equal to 35 GBaud and the RRC roll-off factor set to 0.14. The total bandwidth of the signal is 39.9 GHz. The LMS-based adaptive filters each has 17 taps in time domain. The EO models were ideal, i.e. brick-wall shape with flat passband in spectrum till Fs/2. In these simulations, both frequency and phase of Tx and Rx LO are equal; therefore, carrier recovery was not active. As well, EO models are set to ideal flat spectrum. Symbol identification was a simple search for minimum Euclidian distant per polarization for each received time-domain symbol from carrier recovery. A white jitter profile of RMS of 1 pico-second is introduced at both the Tx and Rx. The FEC was not modelled in our case.

Three set of filters were simulated with each combined with the transfer function of the common multiplexer/demultiplexer. The 3 dB bandwidth of the final concatenation for 12 and 18 WSSs, Fig. 44, are 30.8 GHz and 32.37 GHz respectively. The model of PDL, used in this correspondence, is the following:

$$\boldsymbol{H_{pdl}} = \begin{bmatrix} \cos(\theta) & \sin(\theta) \\ -\sin(\theta) & \cos(\theta) \end{bmatrix} \begin{bmatrix} 1 & 0 \\ 0 & k \end{bmatrix} \begin{bmatrix} \cos(\beta) & \sin(\beta) \\ -\sin(\beta) & \cos(\beta) \end{bmatrix} \tag{5.32}$$

where 0 < k < 1. The attenuation in dB is:

$$PDL_{dB} = -20 * log_{10}(k) \tag{5.33}$$

Since θ and β are randomly varying, the two polarizations (X and Y) are mixed in a time-varying manner. It is up to adaptive filter at the Rx to correct and track for the time-varying crosstalk effects. The overall fiber model, Fig. 53, used is a concatenation of a channel Mux, filtering effect, noise source to mimic the amplified spontaneous emission (ASE) coming from Erbium-doped fiber amplifier (EDFA), bulk PDL element and channel Demux. The EDFAs are typically used in every span to compensate for the loss of fiber and insertion loss of optical components. And N is equal to number of WSSs divided by 2.

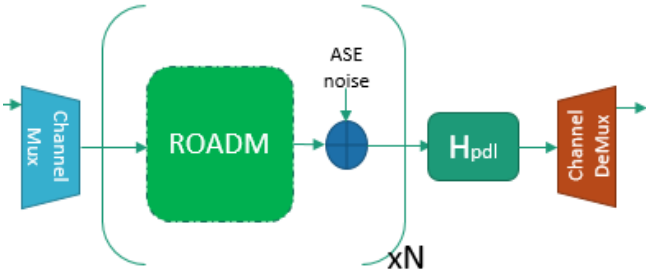

Figure 53: Simulated channel model

The instantaneous PDL, resulting from contributions of many random birefringence in fibers and optical components along the link, can be chosen from a Maxwell-distribution [136]. Therefore, in deployed fibers, the total PDL observed by the Rx is statistical and varies with time. In both our simulation and experiment, we fixed the value of PDL and applied continuous random rotations before and after, as in Eq. 5.32. The value of θ was set to rotate at speed of 800 Hz (maximum rotation measured in buried fibers [137]), while β was rotating at 100 Hz. The BER was averaged out over the length of frame required by the FEC.

5.8 - Simulation Results and Discussion

We start by studying the effect of filtering and PDL on the system performance without any kind of optimization, i.e. the adaptive MIMO filters at the Rx is compensating for all the impairments. In Fig. 54, all data are with a frequency offset of the filter models are set to 0 GHz; therefore, they are modelled as presented in Fig. 44. The ROSNR was measured by sweeping BER versus five OSNR values, then performing an interpolation. We notice that the ROSNR penalty, at 2% BER, versus PDL can be fit to a quadratic function. The penalty of PDL equal to 7.5 dB is inline results reported [43]. As well, as expected, the penalty when aggregating PDL and filtering impairments is bigger than adding the penalty of each impairment tested individually. The reason for the ROSNR penalty is that both impairments are inducing colored noise that affects amplitude. Since the received is equalizing to bring back the two polarizations to be equal and the spectrum to be flat, then it will boost noise as well. Therefore, both PDL and filtering can't be corrected, as PMD and chromatic dispersion, but can only be compensated. As well, when the adaptive filter is compensating for more than one impairment, the taps continuously trying to converge to the solution with the minimum mean square error; however, they are prune to mis-adjustment and hence higher penalty when aggregated. The penalty of 12xWSSs without PDL is ~ 1.05 dB, while when added to PDL, it is ~1.2 dB.

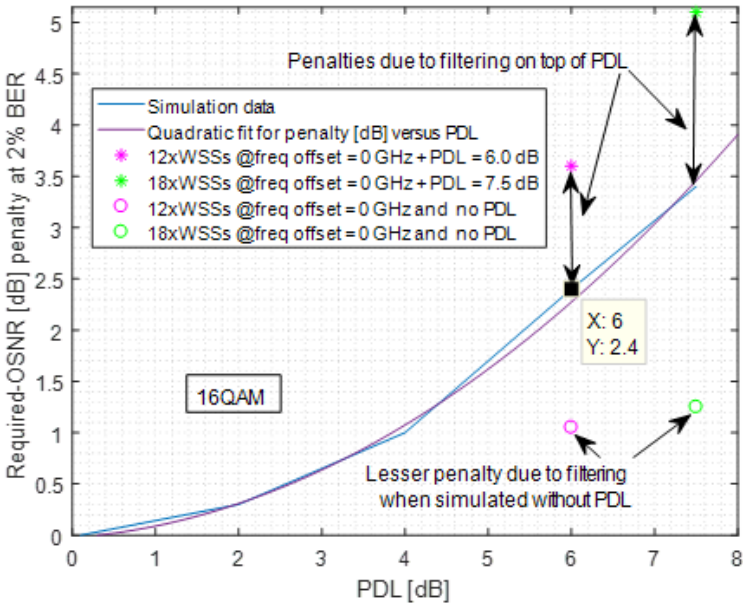

Figure 54: ROSNR penalty as function of PDL and filtering

The higher the noise in the link, i.e. low OSNR, the more advantageous to amplify the signal right at the transmitter since symbols are not corrupted with errors yet. However, to keep the power constant, the peaking of high frequency components comes at the price of de-emphasizing the low frequency bins. Hence the trade-off. However, real transmitters have implementation noise due to quantization (limited bits resolution of both filter taps and QAM symbols), their static filters taps are near clipping and ENOB at the DAC is a function of frequency; therefore, emphasizing frequency bins at the transmitter might be deteriorating rather than helpful. The concept of splitting the compensation is known in serializer/de-serializer (SerDes), as shown in [138], where links have steep loss at high frequencies causing inter-symbol interference. For "Tx Equalization" only, the Tx static filter is programmed with aim to get the spectrum flatten at the output of the modulator, while keeping total power constant:

$$H_{Tx}(f) = H_{RRC}(f) * H_{CMD}^{-1}(f) * |Hc(f)| \qquad (14)$$

At 2% BER, we notice that when method converges (after around 40 iterations on average with the loop running ones every 10 seconds), most of the compensation (~70%) of the steep roll-off of the cascaded filters occurs at the Tx. While the remaining 30% are applied to the static filter of the receiver. At lower BER, i.e. higher link OSNR, the ratios will change. The reason is that it might not be as beneficial to pre-emphasis data since the noise induced is small. Such observations are explained by Weiner optimal solution in presence of pre/post-compensation, Eq.

5.18, where the noise components are showed up in the denominator. As noise gets larger, the post-compensation gets smaller and vice-versa.

With 18xWSSs and PDL of 7.5 dB, splitting the compensation of the steep loss at high frequencies between the Tx and Rx, with minimum mean-square-error at receiver as criteria, reduced the ROSNR by 0.6 dB compared to 0.3 dB when performing pre-compensation only. The penalty versus center frequency offset, due to the mismatch between carrier frequency and center of concatenated filters, is highly dependent on the symmetry of the frequency response of the channel, EOs and data converters. The reason is that all the frequency responses will be multiplied by the signal, with noise added at different stages of the propagation chain, prior being processed by the receiver. As expected, and similar shape was measured in [142], the penalty versus frequency offset has minimal around 0 GHz and gets larger on both positive and negative edges.

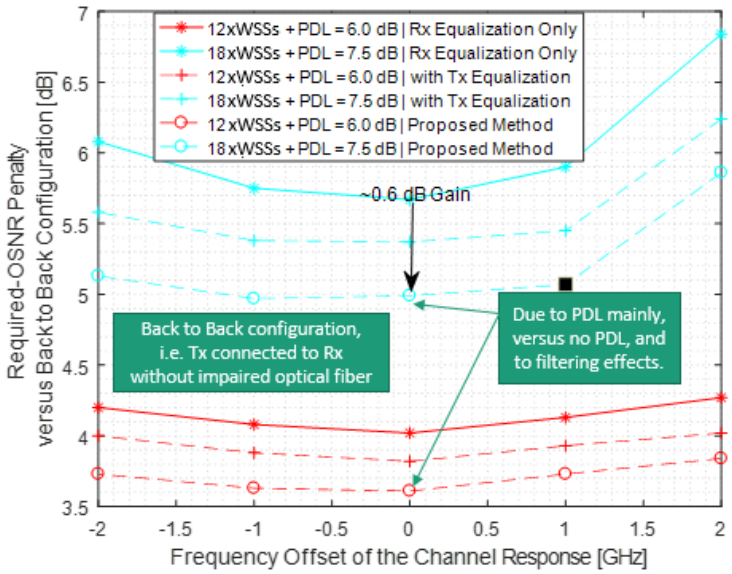

Figure 55: Comparison of different compensation methods, for two scenarios, in term of ROSNR at 2% BER

5.9 - Experimental Verification

The experiment below is using the same filter shape and a calibrated commercial card that is running 16QAM as modulation format, RRC as pulse shape with a roll-off of 0.14 and baud rate of 35 Gbaud.

5.9.1 - Experimental Methodology

A set of experiments were conducted to get the quantitative benefits in real-world settings using

the setup in Fig. 56. We tested channel propagation with PDL emulator, PMD and Polarization Controller. PC1 and PC2, [144], used to scramble the two polarizations sent by the Tx at rotation rate of 800 Hz. Noise was added by controlling the variable optical attenuator (VOA) setting at the egress of the amplified spontaneous emission (ASE) source. Using a LC patch cord fiber, we connected the Tx of a calibrated commercial card to the fiber link. The latter is composed of the following equipment:

- PC1: as polarization scrambler running at 200 Hz SOP rate of change.
- PDL: as PDL emulator to mimic a polarization dependent loss.
- DGD: as DGD emulator to introduce a delay between the two polarizations.
- PC2: as polarization scrambler as well, it is running at 200 Hz SOP rate of change.
- EDFA: due to high loss of the above equipment, it is necessary to compensate for the power loss and to make sure that the received power is in the optimal area to avoid artificial ROSNR penalty.
- An amplifier was used as ASE noise source and the noise level added to signal through fiber combiner through a controllable VOA.
- A fiber splitter 90% / 10 % was used to direct a portion of the optical signal to OSA in order to measure the ROSNR.
- The output of the 90% port of the splitter was connected the common port of the channel Mux/Demux.
- The output port of the Demux associated with wavelength 1546.92 nm was connected to the Rx of the transponder.

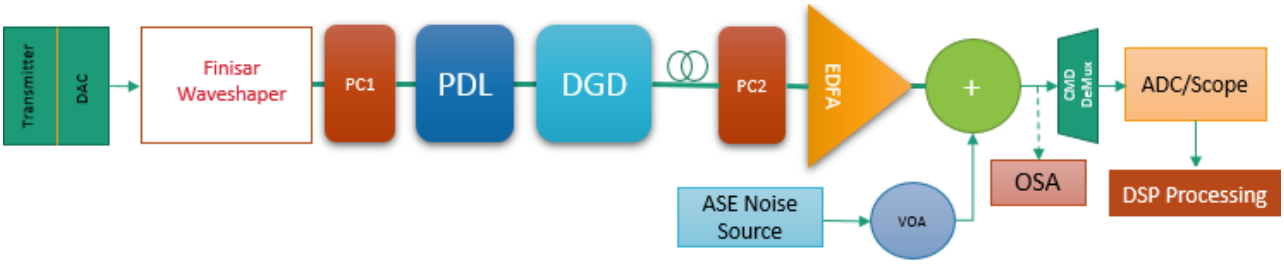

Figure 56: Experimental setup

The LCoS-based 1 GHz resolution waveshaper, [139], was used to mimic two different optical links, as shown in Fig. 44, with the frequency responses of both CMD Mux and DeMux subtracted. Instead, we used real AWG-based CMD at both sides, which helped filtering the noise before

signal is received. PMD emulator was programmed to introduce 30 ps. Variation in PMD, along with state of polarization, can be corrected at the receiver with no penalty. Its introduction here for completeness to mimic real-fiber effects and not directly related to WSSs. The reason is that results in [140] showed, using a high-resolution measurement technique, that a MEMS-based WSS has an upper-bound PMD value of 30 femto-second per port. The commercial card was set in loopback through the experimental work, therefore once acquired, the laser was centered at ITU wavelength of 1546.92 nm (equivalent to 193800 GHz), and only moving within the range of 200 MHz since it is locked to itself.

The procedure described in [143] was used to measure the total PDL seen by the Rx, including the PDL within the Tx (X/Y power imbalance) and the polarization dependent components (PMD emulator). Therefore, the PDL value of 7.5 dB reported in the results is verified to a very high confidence.

To visualize the impact of filtering with real-time measurements, we captured 6 traces as shown in Fig. 57. An optical spectrum analyzer with fine resolution of 300 MHz, [141], was used in the measurement of transmitted spectrum with and without pulse shaping, and filtering effects programmed at the waveshaper. The impact of filtering on high frequency components of transmitted signals is obvious. For our experiment, the waveshaper was provisioned once with the 18xWSSs model. The ASE noise, although completely added after the filtering, it is still filtered by the CMD Demux.

The sweeping of OSNR was done with varying the setting of VOA. The setup was characterized, and we found that the OSNR measurements, done according to IEC 61280-2- 9 standard, are accurate within 0.1 dB. To minimize error, all reported OSNR are the average of 10 consecutive measurements.

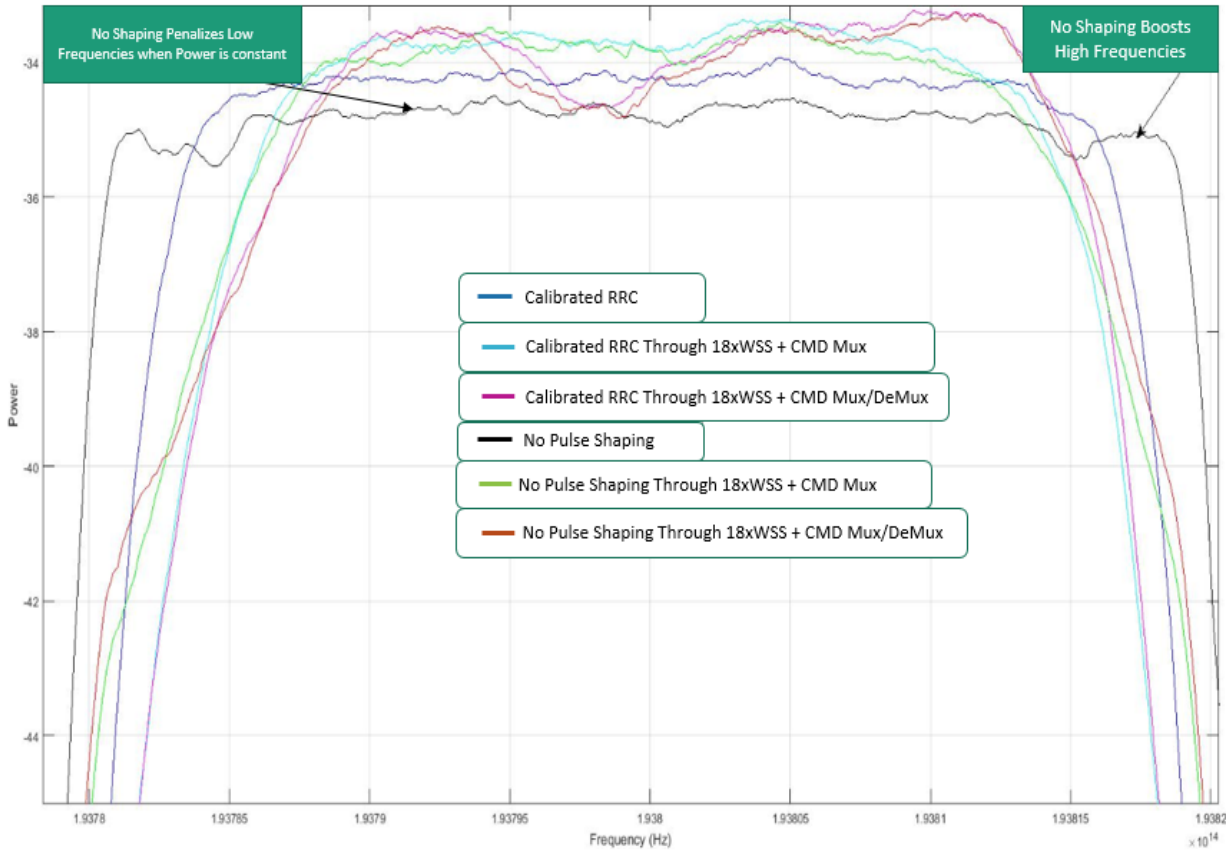

Figure 57: Measured transmitted optical spectrum

5.9.2 – Experimental Results

The lab results are shown in Fig. 58. Unlike how data displayed in simulation results, the required-OSNR again were measured per frequency offset and only the difference to post-compensation only is presented. We saw a consistent gain for both pre-compensation and proposed method, with the minimum gain equal to 0.2 dB, compared to Rx doing the full post-compensating using its adaptive filtering. The proposed method has steady gain over pre-compensation. It does tell that the real-time transponder has many sources of noise at the Tx side.

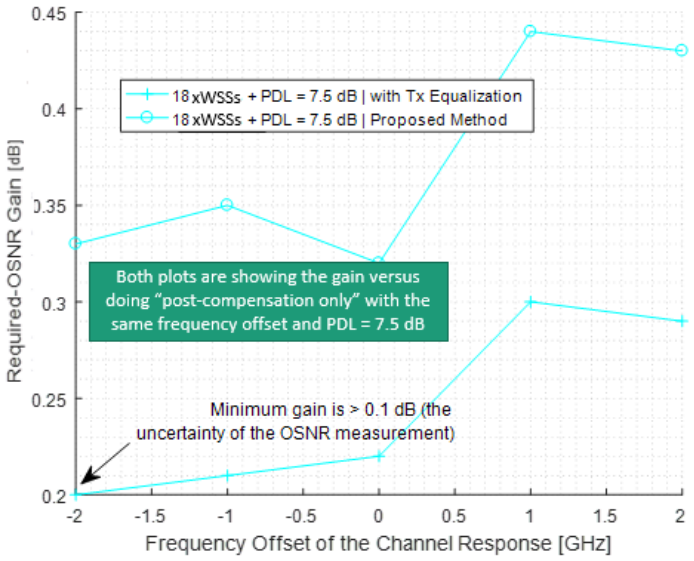

Figure 58: ROSNR gain versus post-compensation only

5.9.3 – Discussion: Simulation Versus Lab Results

The simulation and lab results agree qualitatively. We will list some of the main differences between the two setups:

- Although the Tx/Rx models used in simulation were a fixed-point with inherited implementation noise, the channel model in simulation was Matlab with operations done in floating point.

- The resolution of the waveshaper does not permit the accurate replication of shapes.

- The EO model in simulation had no ripples, while it can be seen from Fig. 14, when bypassing the waveshaper that the signal has frequency dependent ripples. We did not have access to the EO models at both Tx and Rx.

- Carrier recovery is activated in modem, although the frequency of laser was within 200 MHz from ITU center frequency, the small dithering and phase noise would impact slightly the results.

- Although basic jitter models is part of simulation, the jitter for hardware PLL at Tx DAC might be different. As we can see in Appendix B, the overall SNR will be impacted.

5.10 - Conclusion

We presented a new method to perform an adaptive joint Tx/Rx compensation, of stringent filtering effected caused by CMDs and ROADMs in fixed-grid optical networks, while using typical HW blocks in coherent transponder. The only requirement is the availability of communication channel between Tx and Rx. With 18xWSSs scenario, both simulation and lab measurements showed a gain up to 0.5 and 0.15 dB, respectively, in ROSNR at BER of 2% versus doing pre-compensation only.

Chapter 6 – System Study and Compensation Method of Silicon Photonics Modulator in Short Reach Gridless Coherent Networks

"Ignorance leads to fear, fear leads to hatred, and hatred leads to violence." — Ibn Rushd

6.1 - Introduction & Literature Review

AFTER several years of research, silicon photonics has recently entered production and is being highly pursued with the goal of economically satisfying the increasing demand in optical interconnects. Silicon photonic (SiPh) provides a low cost, low power and highly integrated solution which are key features for data center interconnect (DCI) applications. Silicon photonic traveling wave modulators have been under active research and show a good potential for non-coherent applications [145-148]. However, due to the stringent requirements of the coherent modem it is difficult for a silicon photonic based traveling wave Mach-Zehnder modulators (TWMZMs) to be adopted in coherent space. For example, the high required phase shift of the coherent modulator leads to a low bandwidth in the silicon photonic modulator. To compensate for the bandwidth loss, one solution is to peak the high frequency response of the driver at the transmitter (Tx). However, this leads to high power consumption and reduced linearity of the driver.

With optical fibers being in the core of the networks, dense wavelength division multiplexing (DWDM) links should therefore be more flexible. Optical networks evolved from point-to-point links, to fixed add/drop where multiplexing ports are specified per wavelength, to fixed 50GHz bandwidth reconfigurable ROADMs (reconfigurable optical add-drop multiplexer) with internal VOAs (variable optical attenuator) and now with the current high-end generation of WSS (Wavelength Selective Switches) –such as the one based on Liquid Crystal on Silicon (LCOS) technology [149]- that will enable elastic spectral resolution in multiples of 12.5 GHz. The main goal is to fit more channels in the same C-band (or C+L bands) by allowing more agility in assigning traffic to signals with various spectral widths. When channels are travelling together from one source to same destination, we pack them into one media channel (MC), as defined in ITU-T G.870 [150]. Hence, gridless channels are subject to interference from their neighbors.

Typical work in the field of short reach is either based on non-coherent advanced modulation formats such as discrete-modulation-tone [151] and pulse-amplitude modulation [152]. Work done using coherent solution [153] is reported to use standard modulation formats (QPSK, 8QAM and

16QAM). As for the coherent solutions, the design of mentioned constellations does not take in consideration the limitations of the PIC [154], such as the roll-off of the IQ modulator. In [155], authors introduced pre-emphasized drive signal with SiPh modulators, then in [156] they achieved 16Gb/s transmission. The dependency of the transfer function on temperature variation is depending on the configuration of the modulator. While the symmetrically configured interferometer does not have its characteristics change with temperature, ring resonators [157] are highly sensitive. With the operation temperature range is from -5 °C to 75 °C, as specified in GR-468-CORE. The use of continuous joint optimization, beside thermo-control, of both transmitter and receiver static filter dynamic range to mitigate inter-symbol interference is worth investigating. Authors in [157] proposed a pre-emphasis for roll-off in DAC frequency response. The emphasis in the Tx was estimated, assuming knowledge of the real frequency response, by estimating noise and setting a desired response. In [158], pre-emphasis only was used to compensate the non-idealities of low cost phase-modulator in passive optical network, a capacity of 10 Gb/s was achieved for access application. In [159], pre-compensation of I/Q skew and frequency response was used for coherent transponders using 16 and 256-QAM. In [160], authors experimentally compared pulse amplitude modulation (PAM) to discrete multitone modulation (DMT) using SiPh modulator operating in the O-Band. They showed that DMT, using water-filling bits loading mechanism at the Tx based on decoded symbols from the Rx, has lower bit error rate (BER) than PAM-4 for a voltage bias of 4V. As discussed in [161], having multiple subcarrier components being added at the output of the inverse Fourier transform cause high amplitude, spurious-like peaks composite in the equivalent time domain signal. Therefore, the main issue with using DMT, and any other multi-frequency bands transmission schemes, is the resulting increase of peak to root-mean square (rms) ratio (PAPR) compared to single carrier systems. High PAPR imposes on system design that digital to analog converter (DAC), analog to digital converter (ADC), modulator and its driver to have high-swing; otherwise, nonlinearities and quantization noise related impairment will surface. Clipping signal at the input of the driver [162] and precoding schemes such as Walsh-Hadamard [163] can help at the price of system performance. The imperfections in photonic integrated circuits (PIC) due packaging in small form factor and variability of fabrication processes, such as loss or imbalance of delay/power IQ components, can be dealt with using DSP, it does come with a penalty in SNR and complexity in Hardware design. In [164], authors described the benefit, on PAM-2 system in direct-detection mode, of doing only post-compensation, at the Rx when the modulator at the Tx is driverless. The paper did not look into coherent detection.

Our aim in this chapter is to study the impact of the roll-off of SiPh-based modulator in coherent transponder for short reach application (such as 400G ZR using dual-polarization 16-QAM and 100 Km transmission). We will look at the system impact of not pre-emphasizing the signal at the transmitter, we will propose a gradient descent-based optimization method, that uses existing hardware (HW) blocks in a typical coherent receiver, to minimize the mean-square error of the received symbols. We will compare our method to zero-forcing (ZF) version and to doing full pre-emphasis. We will look at the system impact in gridless dense wavelength division multiplexing (DWDM) networks. The paper is organized as follow. In section 6.2, we will describe the SiPh modulator used. The architecture of typical dual-polarization coherent receiver is explained and illustrated in section 6.3. In section 6.4, we will show the mathematical derivation of our proposed compensation mechanism. In Section 6.5, the method is validated through simulation.

6.2 - Silicon Photonics Modulator Model

A SiPh modulator is used at the front-end of optical transponder to modulate a light beam produced by a tunable laser. They are categorized as amplitude, phase or polarization. The authors of this paper, [165], investigated push-pull modulator SiPh MZM based ST fabrication process and fabricated in an SOI process with a low resistivity. The length of the modulator transmission medium and the applied voltage bias determine the resulting frequency response (S_{21}). It was shown the shorter the modulator, the higher is the 3-dB bandwidth when measured using small signal electro-optics (EO) measurements. The resulting frequency response with bias voltage of 4 V is shown in Fig. 59.

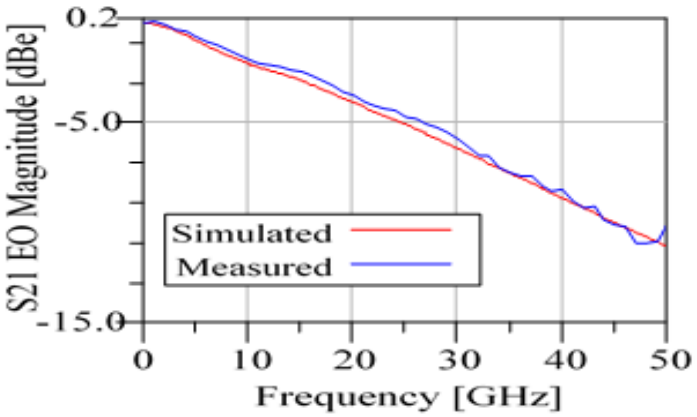

Figure 59: Frequency domain EO response, i.e. transfer function (TF), of a silicon photonic modulator

When modulator' RF drivers are used to boost the low voltage coming from CMOS DAC, a balanced rms voltage is required. If value too high, risking operating in non-linear region of

modulator (edges of the S-curve) and higher power consumption. If too low more carrier leak which causes constellation to shift and degrades SNR.

6.3 - Capacity Trade-Offs & Typical Blocks in Coherent Receiver

Using Shannon formula below, for a given Capacity (*C*), we can trade-offs Bandwidth (*B*) versus Signal to Noise Ratio (*SNR*). if you increase the system bandwidth (i.e. baud-rate) by 1dB, you can expect to add 1dB in overall system SNR penalty due to modulator response with no cause in overall penalty (as the gain in bandwidth increase cancels out the penalty due to the modulator response).

$$C = B * log_2(1 + SNR) \quad (6.1)$$

In Fig. 60, we illustrate the typical blocks in coherent transponder. In the Tx, data streams are encoded then filtered with static filter (CD EQ_x/y). The latter can be used for two purposes: pulse shaping (such as root-raised cosine (RRC)) to help reducing inter-symbol interference (ISI) and dispersion pre-compensation. Data generated is converted to analog domain using a digital to analog converter (DAC) which are characterized by effective number of bits (ENOB). Variable gain amplifiers (VGA), descripted in [166], are used to drive optical modulators since data coming from CMOS is low power and modulator requires high Vpi (7 V in the case here). Tx/Rx FW blocks are the software used to provision and monitor the ASIC and Electro-Optics (EO) controllers. Dual-polarization optical signal is split and mixed with the output of a local oscillator (LO) at the receiver to generate four branches (X/Y polarizations, each has in-phase and quadrature field).

The data is digitized using an ADC then goes to digital signal processing blocks. Similar to the Tx, the Rx side the static filter (CD EQ_x) is used for matching the Tx filter (with RRC to form a raised cosine) to maximize SNR and it is used for dispersion post-compensation. It is typical that the bulk part of dispersion is compensated prior to symbols reaching the butterfly MIMO equalizer. The latter is the core of the receiver and it is adaptive (Constant Modulus Algorithm and Recursive Least Square are examples of the adaptive method used) to decouple the two polarizations and compensate for linear time variant channel impairments such as Polarization Rotation, Polarization Mode Dispersion (PMD) and Polarization Dependent Loss (PDL).

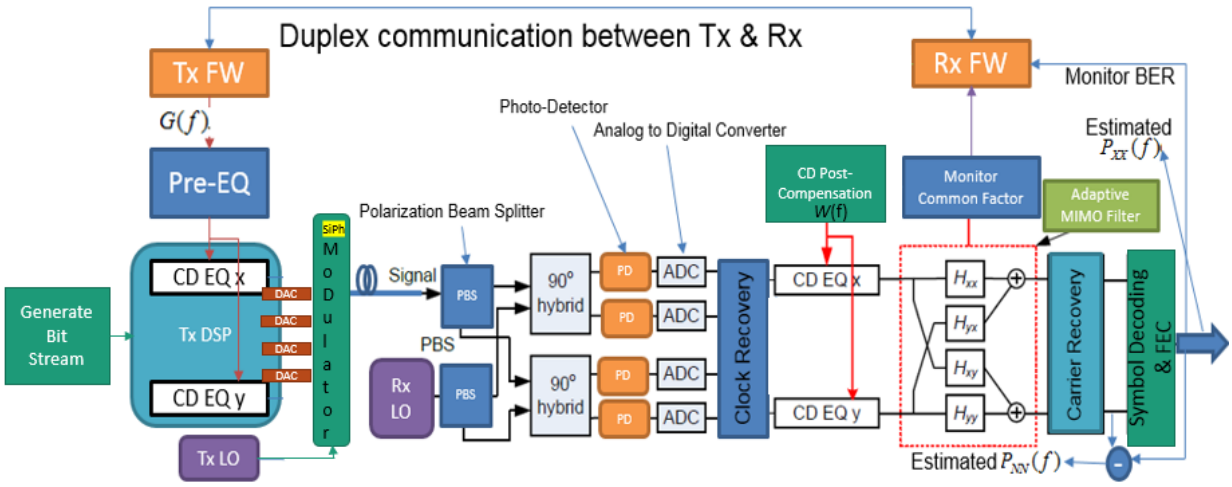

Figure 60: Block diagram showing key functional blocks in coherent optical transponder and requirements for the operation of the presented method

With no impairments, such as frequency selective loss and dispersion, the symbol arrives at the receiver within its "dedicated" interval. Otherwise, we see ISI effect where the transition of the symbols scatters to the neighbor intervals. Digital compensation is basically applying different weights and delays, i.e. filtering, to undo the expansion caused by neighboring symbols over the symbol of interest. The size of the filters required depends on the characteristic of the channels. In the frequency domain, the compensation is mainly pre-emphasizing high-frequency components of the data stream. Beside SiPh modulators, both digital to analog converter (DAC) driving the VGA and ROADMs can have some roll-off at high frequencies. Although it can be different based on the design and the technology. The transfer function of a DAC is typically modeled as:

$$H_{DAC} = sinc(^{\pi f}/_{f_s}) = \frac{\sin(^{\pi f}/_{f_s})}{^{\pi f}/_{f_s}} \qquad (6.2)$$

Analysis of optical modulators, DAC/ADC and channels in frequency domain, using both amplitude and phase responses versus frequency components (*H(f)*), gives a full description of their impacts. When time-domain signal *x(t)*, with its Fourier transform *X(f)*, propagated from the encoder at the Tx, the received signal *Y(f)* is defined as the multiplication of the Fourier transforms of pre-distortion (*G(f)*) and concatenation of frequency responses DAC, modulator, channel, optical integrated coherent receiver (ICR) and ADC. Assuming ideal settings, except for the modulator, we show in Fig. 61 how the amplitude of the common response is "tracking" static impairments. As well, common factor of adaptive filters is compensating for high frequency losses for different decay loss (due to voltage bias) of the SiPh modulators. The adaptive filter is flattening

the spectrum by boosting (post-distorting) the high-frequencies portion of the received signal.

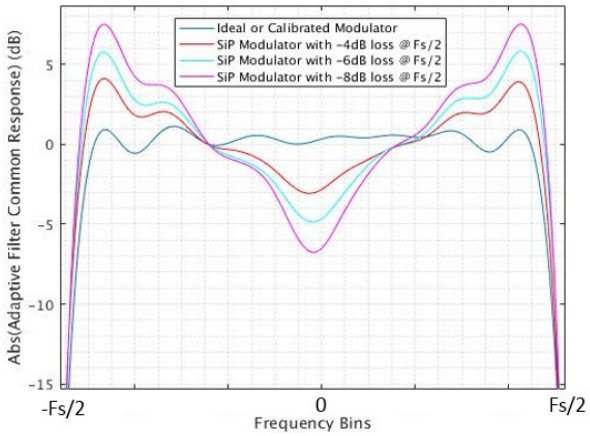

Figure 61: Common response of the adaptive filter after convergence

6.4 - Mathematical derivation

The critical component in PIC is the IQ modulator, where the limitations imposed by design should be understood and over-came to meet the optimal performance. Unequal transition probabilities of input symbols, along with input power constraints, and various FEC overhead can lead to algorithm for efficient use of spectrum. In here, we take a frequency domain approach to re-use existing HW Tx and Rx static filters in typical coherent transponder to optimize the performance. Without power constraint, pre-shaping data only at the Tx would give the best performance since noise has not yet been introduced. However, in practice, transmitters operate with total power constraint over the signal spectrum. The rest of the analysis is similar to section 5.5 of previous chapter.

The equation used to perform the pre-compensation, in which the static part of the channel is estimated and applied through digital signal processing circuity with the aim to flatten the Tx spectrum at the output of the modulator, is the following:

$$H_{Tx}(f) = H_{RRC}(f) * H_{CMD}^{-1}(f) * |H_c(f)| \quad (6.3)$$

The Tx power is kept constant and the chromatic dispersion compensation impacting the phase response only:

$$H_{CMD}(f) = \exp\left(-1 * j\pi * f^2 * \left(\frac{LD\lambda^2}{c}\right)\right) \quad (6.4)$$

6.4.1 - System Benefits of Proposed Method

The overall goal is to flatten the channel response, up to Nyquist frequency, so we remove the ISI before the symbol identifier (or decoder) block. Pre-distorting transmitted pulse to invert fully or partially channel response causes attenuation of the low frequency components of the signal. Therefore, a trade-off between the two exists to get an overall optimal solution, in the mean-square minimum sense. Beside gain in ROSNR per channel or impact on neighboring channels in gridless network as we will see, the method provides three other advantages for coherent system design:

A. Having 6 dB to pre-compensate for at the Tx filter requires 1 bit of effective dynamic range of the DAC. Splitting the compensation helps relaxing the ENOB requirement of the DAC.
B. Relaxing VGA filtering requirement at the Tx since the frequency response does not have to be wide.
C. Continuously moving the compensation of the static portion of the channel, such as chromatic dispersion as in or changes in modulator frequency response to temperature as in our case, to the static filters of the Tx and Rx, allows some of the adaptive filters taps to deal with more dynamic impairments of the optical link such as PMD and PDL.

6.5 - Simulation Settings & results

All simulations were conducted using Matlab 2016b©.

With ideal Electro-Optic model at the Rx, we simulated the system shown in Fig. 60 using Dual-Polarization (DP) 16-QAM as modulation format. The Tx and Rx were implemented in fixed point model; therefore, quantization noise is taken into consideration. Both ADC and DAC have an ENOB of 10 bits. Since we are targeting short-reach applications, 80 to 120 km i.e. up to two spans, concatenation of ROADMs in fixed-grid (75 or 100 GHz as discussed in OIF [167]) networks is not an issue. While in most cases of gridless configurations, Fig. 62, there is only filtering at the edge of the MC on one side of some of the channels, but as well, it is not a concern.

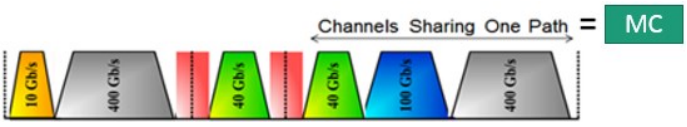

Figure 62: Channels placing in gridless optical network

6.5.1 - Impact of Modulator Frequency Response

In coherent detection, the LO acts as amplifier of the low power optical signal received at the end of optical link. To adopt silicon photonic modulator for a low power, where we don't consume high-power by boosting signal at the Tx and accept the penalty of the frequency response roll-off due to SiPh modulator, we study the impact on ROSNR for two cases. The red curve shows the ROSNR penalty, at BER of 1% and 60 GBaud channel, versus fully compensated modulator. For measured TF in Fig. 59, the penalty is only 0.6 dB. For the blue curve, in Fig. 63, what is reflected here is the penalty we get from getting lower Rx power compared to fully compensating the modulator TF at the Tx (or having an amplifier at the end of the link) that normalizes the power (to reach similar rms) before sampling signal at ADC. Otherwise, when small signal is outside the dynamic of the ADC, the penalty gets much larger. Therefore, most of the penalty is due to the modulator decaying response is indeed due to its attenuation on input signal rms.

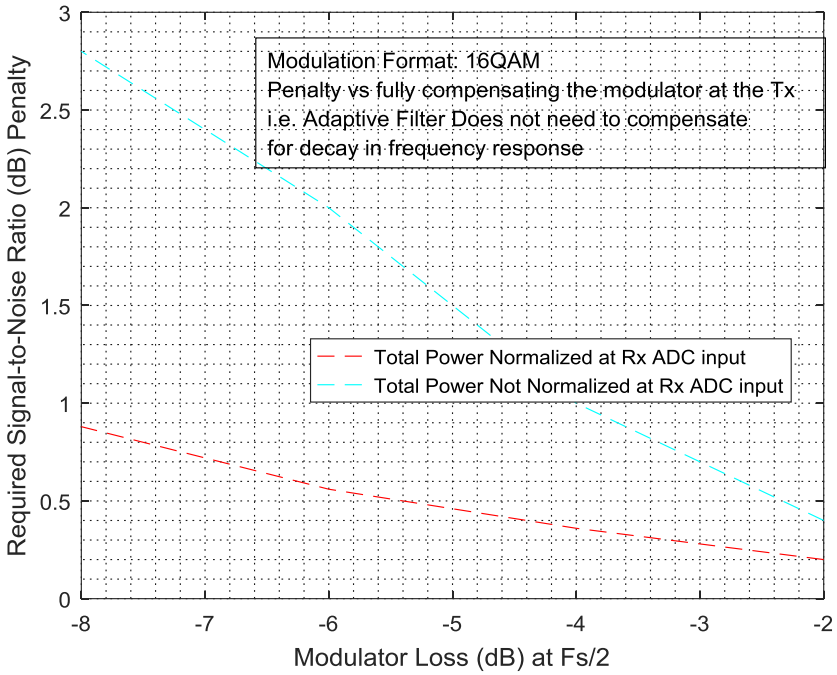

Figure 63: System signal to noise ratio penalty versus loss in TF at Fs/2

6.5.2 - Benefits of Proposed Method

Both described methods in Section IV result in combining Tx and Rx compensation, of the modulator response, such that they effectively constitute a matched filter pair. Doing full pre-compensation is not always the optimum case especially when Tx, before the modulator, is impaired with multiple sources of noise such as high noise figure of VGA driver, low DAC ENOB

and Tx implementation noise. In Fig. 64, we notice the advantage of the joint equalization is getting larger as the signal Baud-rate increases. The main reason is that the more loss we are try to compensate, while keeping power constant, we penalize low frequency contents. As well, the digital Tx peaking when being quantized through the DAC, the amplitude of the high-frequency components is amplifier, therefore the impact of jitter and quantization is higher.

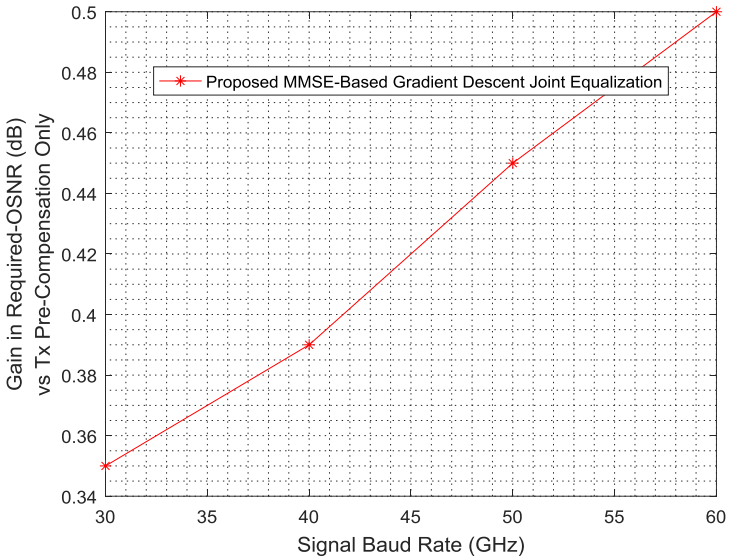

Figure 64: Simulation results showing comparison of different compensation versus baud-rate

6.5.3 - Impact of Proposed Method in Gridless DWDM Link

It is known in wireless, since channels are using the same medium over different frequencies, specifications such as the adjacent channel leakage-power ratio (ACLR) are required to limit the impact on neighboring signals. In gridless optical DWDM networks, there is a need to do such tests if channels are transmitted within same MC. As you can see in Fig. 65, the less power a channel has at the edges (less pre-compensation), the less leaked power to impact SNR of neighboring channels.

With three channels, one as probe and two as interferes as illustrated in Fig. 65, the interferes are using SiPh modulators with 6 dB decay at 30 GHz and static filter set with optimal solution. The reference ROSNR is defined when the carriers are 61 GHz apart i.e. channel spacing is equal to total channel bandwidth of 61 GHz. In Fig. 66, we present the gain in term of reduction in ROSNR of the probe, typical fully compensated Tx DAC and analog/EO chain, versus spacing between the center of the probe and the two interferes.

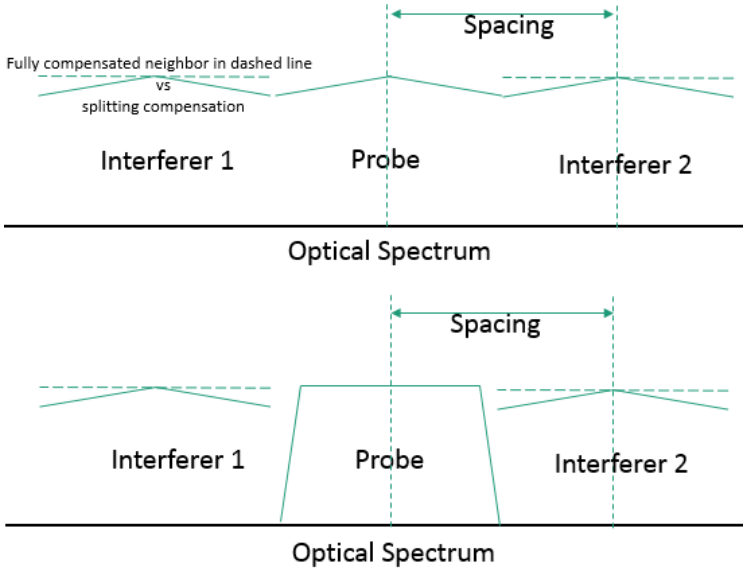

Figure 65: Illustration of the two scenarios simulated for gridless applications

As expected, when channels are squeezed, i.e "Spacing" in Fig. 65 is getting smaller, there is less noise power leaked into the neighbor channel, hence higher SNR. For richer constellations, we expect the gain to be higher since they are more susceptible to noise, [91], then will benefit more from less power leakage from neighboring channels.

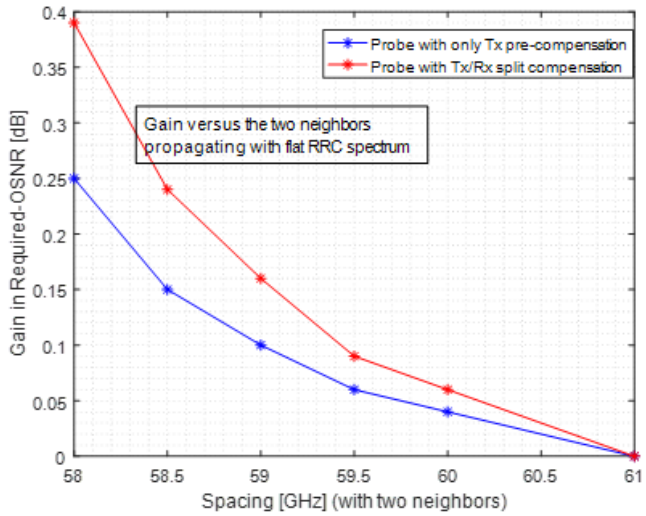

Figure 66: ROSNR Gain versus channel spacing in gridless application

6.6 – Conclusion

We studied the impact of bandwidth loss of SiPh MZ modulators in coherent receivers. We showed that our proposed MMSE gradient-descent based method provides 0.5 dB of ROSNR reduction for 60GHz channel when decay of modulator TF is 6 dB at 30 GHz. We presented

system benefits of not doing full pre-compensation at the Tx signal processor. As well, we showed that when squeezing channels in gridless networks, using joint compensation provides a reduction of 0.1 dB to the probe channel when squeezing both neighbors by 2 GHz.

Chapter 7 – Adaptive Coherent Receiver Settings for Optimum Channel Spacing in Gridless Optical Networks

"The ideal subject of totalitarian rule is… people for whom the distinction between fact and fiction and the distinction between true and false no longer exist." — Hannah Arendt

7.1 – Introduction

THE cloud computing era is pushing operators to upgrade to more autonomous and agile management of traffic demands. With optical fibers being in the core of the networks, DWDM links should therefore be more flexible. Optical networks evolved from point-to-point links, to fixed add/drop where multiplexing ports are specified per wavelength, to fixed 50GHz bandwidth reconfigurable ROADMs (reconfigurable optical add-drop multiplexer) with internal VOAs (variable optical attenuator) and now with the current high-end generation of WSS (Wavelength Selective Switches) –such as the one based on Liquid Crystal on Silicon (LCOS) technology [149]- that will enable elastic spectral resolution in multiples of 12.5 GHz. Such flexibility in the photonics transport layer, is completed with advancement in software-defined coherent transponders. The latter are typically dual-polarization coherent optical receivers coupled with high speed data converters and intelligent digital signal processing [168]. With centralized control and high-level applications, SDN (software defined networking) is coming along. The paradigm is based on monitoring, provisioning and running networks with zero-touch. Since performance metrics are being collected from existing channels in the network, ideally network management should take advantage of them to optimize the process of adding new capacity.

Managing gridless channels is by far the biggest turmoil of photonic systems. The level of complexity in planning and assigning resources grows exponentially with available ports and directions. The main goal is to fit more channels in the same C-band (or C+L bands) by allowing more agility in assigning traffic to signals with various spectral widths. The red areas, appearing in Fig. 62 (previous chapter), are dead-bands on the edges of each Media Channel (MC), they can be up to 6.25 GHz roll-off as defined in ITU standard [150]. When channels, each called Network Media Channel (NMC), are travelling together from one source to same destination, we pack them into one MC (as defined in ITU G.870). Hence, gridless channels are subject to interference from their neighbors. When excess bandwidth is used as part of clock recovery scheme, spectral energy from adjacent channels first leaks in the edge bands which hinders the integrity of the extracted transmitter clock manifested by an increase in clock jitter. The latter defines the certainty in the sampling moment and the effective number of bits (ENOB) of the

interleaved high-speed analog-to-digital converters (ADC) [169]. The clock recovery loop is built around a Phase Detector (PD) implemented in digital processing domain, a voltage- controlled oscillator (VCO) gain and filtering elements working in conjunction to reduce the sources of noise.

One of the most important aspect to enable high-speed optical networks for 400 Gb/s and beyond, is the performance of data converters. Therefore, jitter is a key impairment to be studied as circuits are required to operate at high-speed clocks, while having higher ENOB to support rich modulation formats and reduce power dissipation. With samplers operating at 100 Gsample/s, as demonstrated in [170], the unit interval of transmitted symbols is 10 ps. Therefore, better systems and practices to control and mitigate jitter are crucial to future optical (coherent and non-coherent), wireless (such as 5G) and wireless (backplane serializer/de-serializers). Our simulation, Fig. 67, shows how the penalty measured, in required-optical-signal-to-noise ratio at 3% bit error rate (BER), is sensitive to untracked jitter when the order of the modulation format is higher.

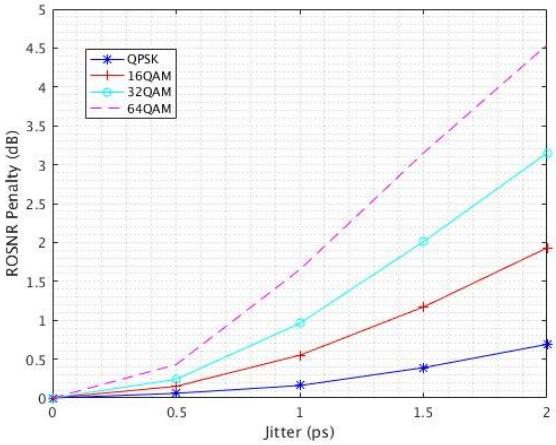

Figure 67: ROSNR penalty versus uncorrected jitter for various modulation formats

In this paper, we present a new methodology to optimize the channel spacing per MC by adaptively controlling the coherent receiver settings based on link conditions. The method, along with using a new clock recovery circuity as an example, is validated through experimental results. The paper is organized as follows. In section 7.2, we describe the source of noise in optical links and clock recovery circuity. The theory along with simulations are presented in sections 7.3 and 7.4, respectively. Finally, in section 7.5, we describe the experiment performed and show the results.

7.2 - Clock Recovery in Coherent Optical Receivers

With rich modulation formats becoming the norm in coherent transceivers, data converters are

more sensitive to degradations in signal-to-noise ratio (SNR); especially with single-carrier modems operating at high-baud rates, hence higher frequencies at the ADCs input. One of the key tasks to maintain good performance, and to allow signal processing to compensate for the optical channel, is to optimize the clock synchronization for the ADC. The typical architecture of such apparatus is shown in Fig. 68.

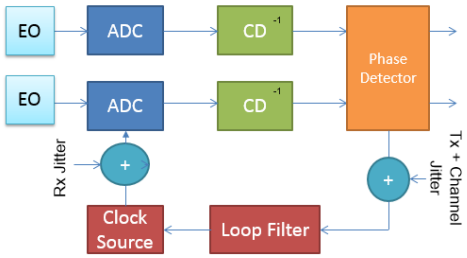

Figure 68: Simplified clock and data recovery schemes used in coherent receivers

The main objective of the clock recovery is to estimate the timing offset and compensate for it. The architectures discussed in the literature are typically a combination of digital and analog blocks, and designs can be feedforward-based, feedback or a combination of both, and data-aided versus non-data aided [171]. In the context of optical gridless networks, cross-talk from adjacent channels is an extra source of linear impairments. It is a bigger challenge when clock recovery depends on excess bandwidth, i.e. phase detector is non-data-aided. That is especially the case in Nyquist and Super-Nyquist spacing. The latter is defined as when the spacing between channel and its neighbor (Δf) is smaller than the channel bandwidth (B). In the case of root-raised cosine pulse shaping, the excess bandwidth is governed by the roll-off factor β and it is defined in time-domain as:

$$h(t) = \frac{2\beta}{\pi\sqrt{T}} \frac{\cos\left[\frac{(1+\beta)nt}{T}\right] + \frac{\sin[\frac{(1-\beta)nt}{T}]}{4\beta t/T}}{1-(4\beta t/T)^2} \qquad (7.1)$$

With T is the duration of the symbol. The frequency domain spectrum is illustrated in Fig. 69, showing the excess bandwidth.

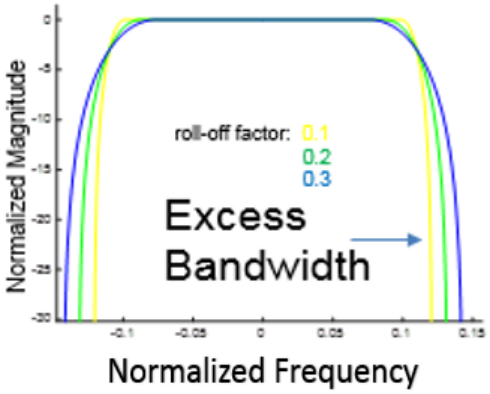

Figure 69: Root-raised cosine filtering example with different roll-off factors

7.2.1 - Sources of Jitter

Coherent receivers must deal with two main sources of jitter, one is specific to optical impairments and the second is due to typical PLL implementation. Jitter from optical links is due to:

- ASE (amplified spontaneous emission) induced by optical line amplifiers can shift the pulse from its ideal location [172].
- CD (chromatic dispersion), which its bulk part should be compensated before being able to digitally recover timing information, although a certain residual dispersion tolerance is anticipated but it comes with a penalty. In [175], when CD is convoluted with the phase noise of the local oscillator it causes timing jitter.
- Kerr nonlinearity such as SPM (self-phase modulation) and XPM (cross-phase modulation) have effect on timing jitter as shown, respectively, in [173] and [174].

From the electronics side or RF (radio frequency), on both the transmitter and receiver clocks, the dominant sources of jitter in PLLs are the VCO (voltage controller oscillator) and CP (charge pump). With respect to the VCO, it is subject to jitter accumulation which manifests itself as high phase noise at low frequency offsets with respect to the carrier frequency as depicted in Fig. 70. This can be expressed with the following simplified Leeson' frequency domain equation [176]:

$$\boldsymbol{L(f_m) = \frac{FKTemp}{2P}\left[\frac{1}{f_m^{\,3}}\frac{f_c^{\,2}\frac{f_1}{f}}{4Q_L^{\,2}} + \frac{1}{f_m^{\,2}}\frac{f_c^{\,2}}{Q_L^{\,2}} + \frac{\frac{f_1}{f}}{f_m} + 1\right]} \quad (7.2)$$

With:

Q: Resonator loaded Q

P: Resonator power

$\frac{f_1}{f}$: Flicker noise corner

f_m: Offset from carrier

f_c : RF frequency

F: Oscillator noise figure

K: Boltzmann's constant

Temp: Temperature

Other sources, [177], are thermal noise, and flicker noise in clock buffers, internal aperture of the ADC, supply variation and electromagnetic coupling. The latter is due to the decrease in electronic channel lengths when circuits are integrated on the same substrate. Some jitter, or ripple effects, is caused by the closed loop control. The design of the loop filter order and bandwidth plays a major role in controlling the total jitter induced.

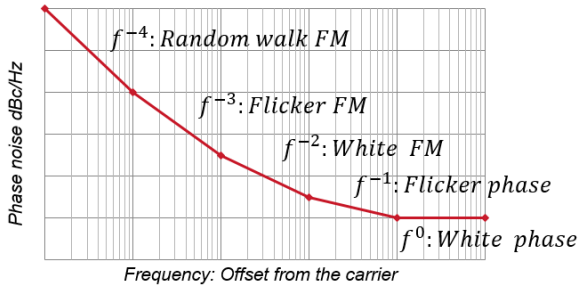

Figure 70: Phase noise versus frequency in PLLs

7.2.2 - Timing Phase Error Detection

At the receiver, to track the transmitter sampling clock, we leverage some out of band signal energy to estimate the total phase noise. The center frequency band of the signal, i.e. direct current (DC), does not experience any jitter effect; while the higher the frequency the more deviation the data will be from the ideal sampling value. This phenomena is illustrated graphically in the Fig. 71. Therefore, to measure jitter, we need to look at the phase error from DC to the highest frequency, i.e. end of signal bandwidth.

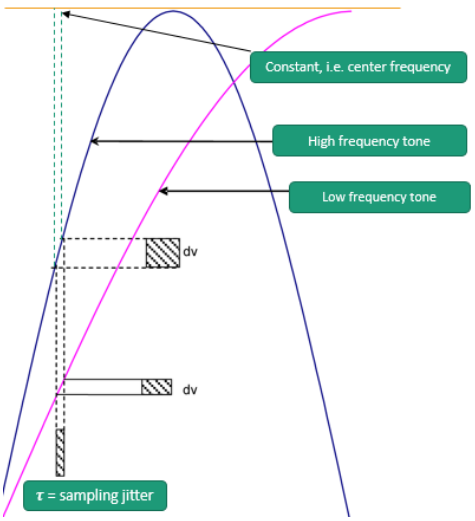

Figure 71: Jitter impact as function of frequency

We will examine mathematically how to use excess bandwidth to extract clock information. A time-domain approach is detailed by Gardner in [32] and the equivalency between different methods is available in [178]. In here, we are using a frequency domain approach. The transmitter will upsample the data in order to produce identical frequency domain contents at the extreme edges of the spectrum. Initially, let's assume there are no impairments. Let $\{X_k\}$ represent a single DFT of size N obtained from analog input signal $x(t)$ sampled with period T_s at the "optimum" instants.

A property of the DFT is that a shift in time corresponds to a phase ramp in the frequency domain. If we had sampled late by a time offset of $\boldsymbol{\tau}$ we would get:

Let's define *G* as the number of bins before pulse shaping and *N* as number of bins after pulse shaping, i.e. includes excess bandwidth. Now let's define sampling phase offset (in radians) as function of time offset:

$$\varphi \triangleq 2\pi \frac{\tau}{T_s} \qquad (7.3)$$

Then the phase shift introduced on each DFT bin is simply:

$$\theta_k = 2\pi \frac{\tau}{T_s} \frac{k}{N} = \frac{k}{N} \varphi \qquad (7.4)$$

We'll apply this construct to the frequency bins after the DFT. With optimum timing the pair $\{X_k, X_{k-G}\}$ separated by G bins would have the identical phase, just as they had at the transmitter. We'll use this general property in polar domain of complex numbers:

$$X_a = r_a \exp(j\theta_a) \quad (7.5)$$

$$X_b = r_b \exp(j\theta_b) \quad (7.6)$$

$$X_b^* = r_b \exp(-j\theta_b) \quad (7.7)$$

$$X_a X_b^* = r_a r_b \exp(j(\theta_a - \theta_b)) \quad (7.8)$$

$$\angle(X_a X_b^*) = \theta_a - \theta_b \quad (7.9)$$

Then, with sampling phase offset of φ we get:

$$\angle(X_k X_{k-G}^*) = \theta_k - \theta_{k-G} = \frac{k}{N}\varphi - \frac{k-G}{N}\varphi = \frac{G}{N}\varphi \quad (7.10)$$

Extracting the phase above translates into being able to estimate the phase error τ. The latter is smoothed and by a control loop, as shown in Fig. 3, to properly adjust the receiver sampling clock used in the ADC.

7.2.3 - PLL Basics

A detailed look at PLL allows us to elaborate on the limitations of the existing clock recovery methods in gridless applications. Both control theory and signal processing are required tools to study the stability of PLLs. The basic structure of PLL is depicted in Fig. 72.

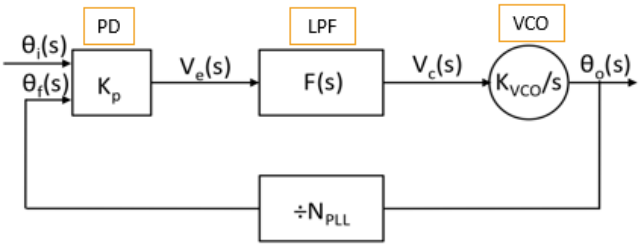

Figure 72: Block diagram representation of a PLL.

A typical PLL consists of a PD, a low pass loop filter (LPF) and a VCO in the feed-forward path and a frequency divider (N_{PLL}) in the feedback path. The need for divider is that reference clocks, crystal-based ones, are stable and have low jitter at low frequencies. Therefore, we adjust the input voltage of the VCO as part of the feedback loop. Under steady-state conditions, the PD creates an output that is proportional to the phase/frequency difference of its two inputs with a gain of *Kp*:

$$V_e(s) = K_p \left(\theta_i(s) - \theta_f(s)\right) \qquad (7.11)$$

The loop filter (LPF) is assumed to be a low-pass filter with general transfer function *F(s)*. The order of the filter depends on the configuration of the resistors (R) and capacitors (C). The higher the order of the PLL, the more rejection of high-frequency components is achieved in the forward path. If *n* is the number of cascaded *RC* stages, the resulting frequency domain filter response, have a roll-off of (n x -20dB)/decade.

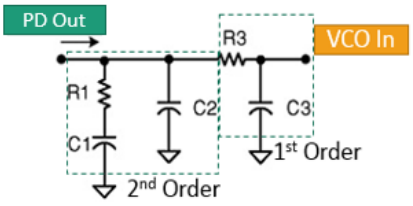

Figure 73: A third-order PLL loop filter

Fig. 74 shows the frequency response for a 2nd, 3rd and 6th order PLL implementation. Filters of high orders achieve more rejection of noise and spurs from both VCO and reference.

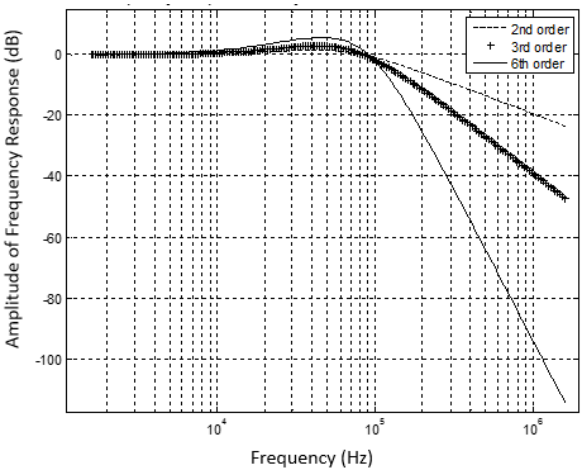

Figure 74: Magnitude of the frequency response of three PLLs with different filter order with same 3-dB bandwidth

The VCO is responsible for generating the high-frequency clock used to drive the ADC. It converts a voltage to frequency with a gain of K_{VCO} and frequency offset w_{FR}. Since the input and output variables of a PLL are best described in terms of instantaneous phase, the VCO operation can be described in the Laplace domain as:

$$\theta_o = \frac{K_{VCO}}{s} V_c(s) + \frac{w_{FR}}{s^2} \qquad (7.12)$$

Finally, the divider in the feedback path N_{PLL} reduces the frequency or phase of the signal feedback to the PD:

$$\theta_f(s) = \frac{\theta_o(s)}{N_{PLL}} \qquad (7.13)$$

When deriving the closed-loop form reflecting input-output behavior of the PLL, we get an aggregation of a low-pass filter (second term) that governs the reference to output response and high-pass filter (first term) that governs the noise from the VCO viewed from the output. Presented in eq. (7.14) below:

$$\theta_o(s) = \frac{N_{PLL}\omega_{FR}}{s\left(N_{PLL}s + K_{VCO}K_pF(s)\right)} + \frac{sN_{PLL}K_{VCO}K_pF(s)}{s\left(N_{PLL}s + K_{VCO}K_pF(s)\right)}\theta_i(s) \qquad (7.14)$$

Typical reference clocks have their phase noise at low frequencies; Hence decreasing the forward-path loop bandwidth (left of Fig. 75) does not add much noise from the reference. However, decreasing bandwidth of the low-pass means increasing bandwidth of the complementary high-pass and therefore, letting more VCO noise through.

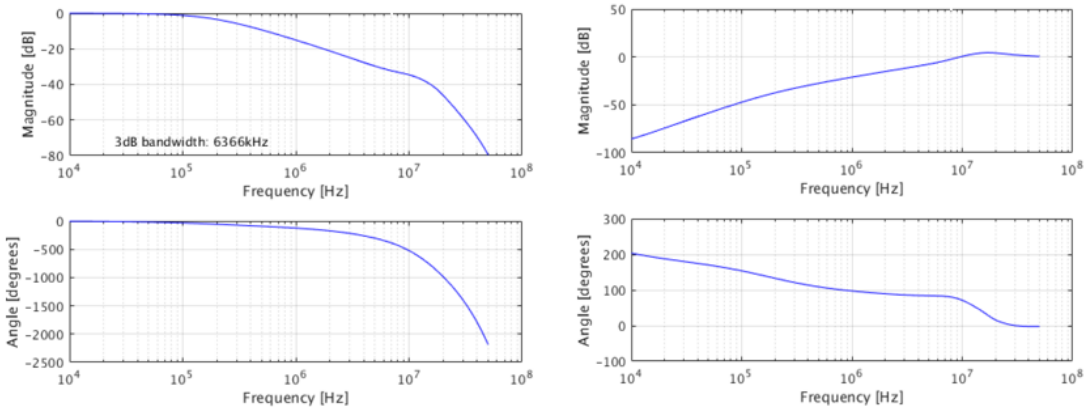

Figure 75: Reference to output and VCO to output transfer functions

7.3 - Clock Recovery Circuit and Method

We are proposing a new methodology to optimize the channel spacing based on the total jitter seen by the receiver in gridless networks. We will discuss the issues with typical clock recovery architecture, then present our circuit and methods.

7.3.1 - Limitation of Existing Architectures

As discussed at the end of section II-C, when the clock recovery loop is controlling the VCO

directly, Fig. 76, adjusting the bandwidth will result in higher VCO noise, i.e. degradation of system performance. Hence, the key limitation of existing clock recovery circuity is the lack of flexibility and hence they can't be optimized when "Data Clk" is corrupted with leaked power from neighboring channels.

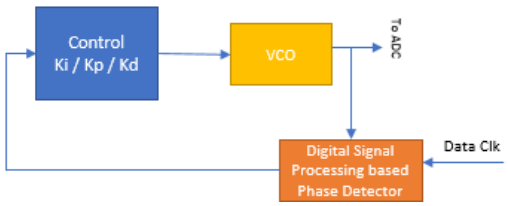

Figure 76: Clock recovery circuit used Optimization Method

7.3.2 - Our Proposed Circuit

In the receiver, a clock recovery scheme which decouples the intrinsic VCO jitter bandwidth requirement from the clock recovery overall bandwidth is used. To do so, we are segregating our circuit into two loops: digital PLL, with high bandwidth in the forward path to filter as much as possible VCO noise, and another loop is governed by the software controlled "Digital LPF" and interacts with the "Numerically Controlled Oscillator" by adjusting phase delay. The architecture is presented in Fig. 77. The parameters of the digital or analog PLL, represented as "Numerically Controlled Oscillator", VCO gain/PD gain/loop damping and bandwidth are chosen in a way to guarantee a stable operation around the desired sampling frequency and adequate transient time.

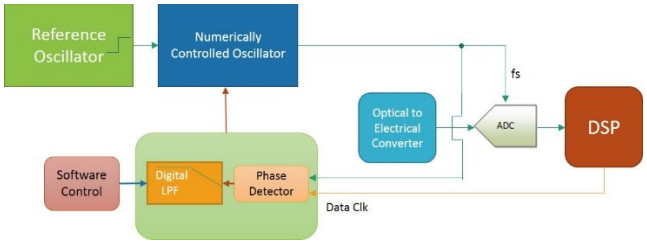

Figure 77: Clock recovery circuit used Optimization Method

In presence of interference from adjacent channels, "Data Clk" becomes noisy. Therefore, the bandwidth of the software controller "Digital LPF" can be adjusted to filter the noise without affecting the stability and noise profile of the "Numerically Controlled Oscillator". In our design, the latter locks to a reference clock with a high bandwidth to reduce VCO phase noise.

7.3.3 - Method Overview

To elaborate further, we note that when measuring SNR, and assuming noise is uncorrelated with zero mean, it is averaged over *L* observations to smooth out the result:

$$SNR_{averaged} = \frac{E[|signal|^2]}{\frac{E[|\sum noise|^2]}{L^2}} = \frac{E[|signal|^2]}{\frac{L*E[|noise|^2]}{L^2}} = L * SNR_{original} \quad (7.15)$$

The equivalent of lower loop' bandwidth is the higher averaging of incoming error signal prior to produce a control signal. Therefore, the system performance gets better if there is no high-frequency noise source that goes untracked.

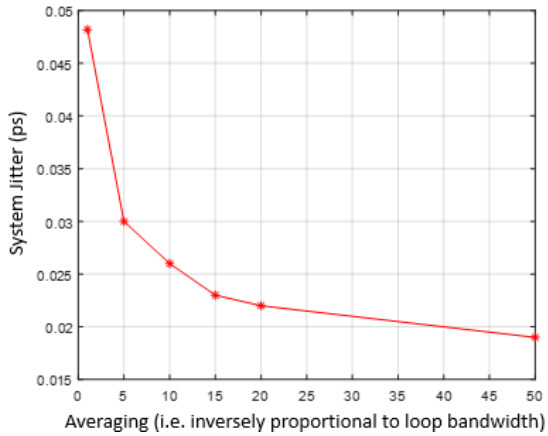

Figure 78: Jitter measured versus averaging of Clock recovery circuit used Optimization Method

The phase domain (ϕ_{dBc}) spectral density of the different contributors at the receiver is depicted in Fig. 79. As can be seen, lowering the clock recovery bandwidth effectively helps in filtering out the impact of the adjacent channel interference (in yellow) and would provide better signal integrity with respect to the transmitter clock extraction. However, the untracked jitter from the Tx, for example, must be bounded to keep the overall jitter within specification. A scheme that takes into consideration phase noise induced by channel and where the effective clock recovery bandwidth and gain can be digitally programmed is required.

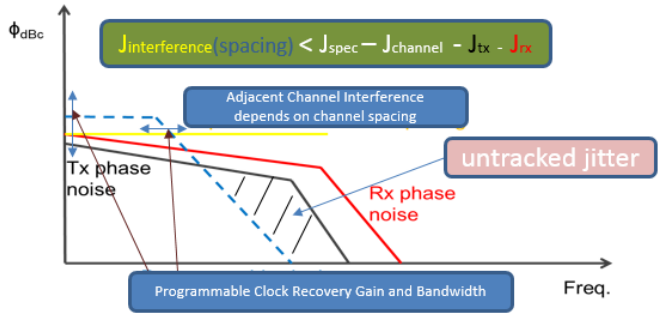

Figure 79: Phase-domain spectral density of different contributors

In addition, optimizing the clock recovery bandwidth reduces the effective tracking by the receiver of the other sources of jitter. If we assume J_{rx} (jitter induced by Rx) is tracked by the receiver PLL, $J_{channel}$ can be estimated from neighboring channels in the same MC. For the cases of low transmitter clock standard deviation in the total phase error (J_{tx}), we can simply base the optimized parameters (bandwidth and gain) on the specification in order to perform a fitting to extract optimal channel spacing as shown in Fig. 80.

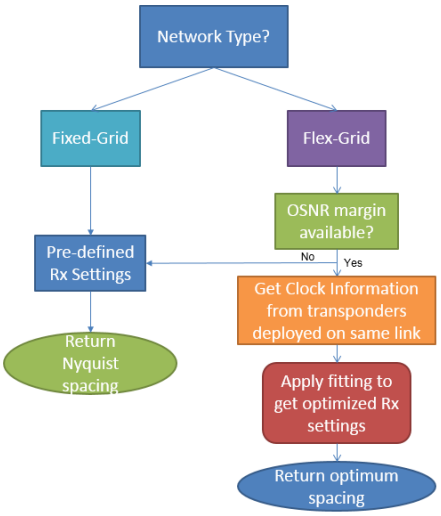

Figure 80: Application-layer algorithm

"Digital LPF" is illustrated in Fig. 81. It is implemented as simple proportional/integral control scheme [179].

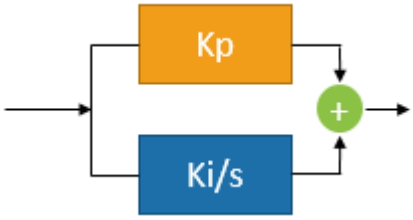

Figure 81: Proportional/Integral Control in Laplace-domain

The relationship between loop bandwidth and Ki setting, to be stored per card during calibration, is manifested in Fig. 82. For simplicity, we are showing the equivalency between clock recovery loop bandwidth, blue dashed line in Fig. 79, and Ki control setting. It is shown that the higher the gain, the faster the loop reacts to changes, therefore, the higher the bandwidth.

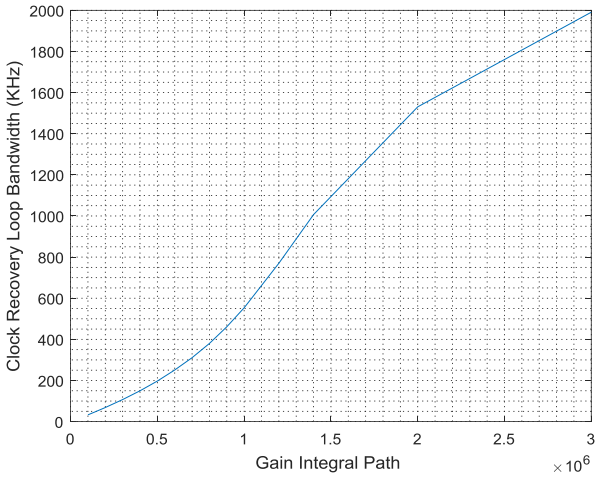

Figure 82: Loop bandwidth versus Ki setting

Since with Software-Defined Networks (SDN) the trend is to have a centralized server that oversees the whole networks, passing information about the link to modems can be performed using NETCONF, an Internet Engineering Task Force (IETF) network management protocol. Upon a request for a new channel, a brute force method can be used to optimize parameters by adding the channel at nominal spacing (pre-defined or at (1+β)*symbol-rate) then run 2D sweep using receiver firmware (or processor) to find the minimum jitter. Based on the margin available (targeting 100G QPSK in this case), squeeze the channel using a fitting method. The latter can be derived from the modelling performed in Fig. 84, where we associate a spacing and OSNR with jitter margin. Both discrete look-up table based or continuous fitting, can be used to translate a jitter margin, defined based on specifications associated with the modem, into spacing when knowing the OSNR.

7.4 – Simulation Results

7.4.1 - System Penalty versus Channel Spacing

When measuring the impact of spacing on the ROSNR (Required-OSNR) for different modulation formats typically used in commercial coherent modems, we see that the penalty gets higher as the constellation gets denser (Fig. 83). We looked at cases covering submarine links, to long-

haul, metro and data-center interconnects with a DP-32QAM modulation format to be able to predict how ROSNR in link budget will be impacted by channel spacing. It will give us as well the minimum OSNR availability required to perform the optimization process. The simulation below covers the case of two neighbors with same power as the probe. In other terms, the penalty is due to Signal-to-Interference & Noise Ratio (SINR) is defined as:

$$SINR = \frac{P_S}{P_I + P_N} \qquad (7.16)$$

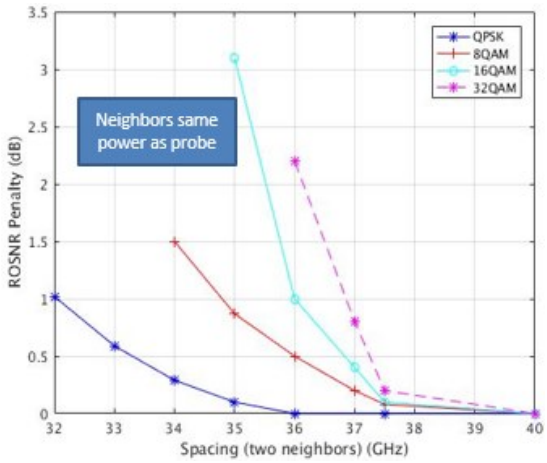

Figure 83: ROSNR, at 3% BER, penalty due to spectral leakage from neighboring channels

7.4.3 - Jitter Tolerance versus Channel Spacing

Typically, the PSD of the generated phase noise of VCOs within a PLL is modelled as a Lorentzian distribution. When putting components together in simulation, we predict the effects on total jitter and the ability of the receiver to acquire. In Fig. 84, 0% margin is the point at which the receiver can't reach steady state and 100% is when jitter reaches its expected noise floor (that is due to various sources presented in section 7.2.1). The lower the OSNR, the more noise is added to the data and then higher jitter is simulated. However, in Fig. 84, the ramp is steeper versus spacing compared to change in ASE noise level. That observation can be explained by the high bandwidth phase noise induced in the jitter estimation when squeezing channels together. We can use this model as part of our methodology to predict the jitter margin available versus a link OSNR and spacing.

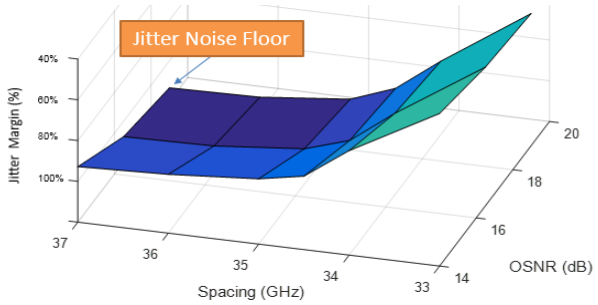

Figure 84: Jitter versus spacing and noise level

7.5 - Experimental Verification

7.5.1 - Experimental Methodology

A set of experiments were conducted to get the quantitative benefits with real-world flex-grid settings using Ciena 6500 ROADMs. We used three 100G QPSK channels with the center one being the probe as in Fig. 85.

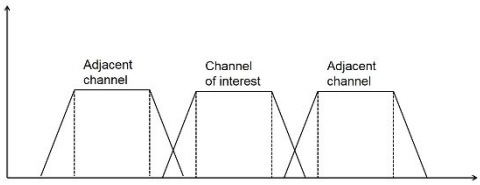

Figure 85: Gridless setup

We used the setup shown in Fig. 86 with three WaveLogic3 © transponders operating at 35GBaud, two as interferers and one centered as the probe ("two sides" or "two neighbors" are used to reflect that the probe channel is "double-sided"). Since most digital signal processing techniques for clock recovery are sensitive to optical impairments, our sweeps were done over multiple Polarization Dependent Loss (PDL), Differential Group Delay (DGD), State of Polarization (SOP) scramblers (PC1 / PC2) and OSNR values. The latter is controlled by adjusting a variable optical attenuator (VOA) at the egress of an ASE source.

Using a LC shape patch cord fiber, we connected each of the three Tx of calibrated commercial cards to the channel Mux/Demux of a Ciena ROADM 6500 ©. The common fiber is then connected to the fiber link. The latter is composed of the following equipment:

- PC1: as polarization scrambler running at 200 Hz SOP rate of change.
- PDL: as PDL emulator to mimic a polarization dependent loss.

- DGD: as DGD emulator to introduce a delay between the two polarizations.
- PC2: as polarization scrambler as well, it is running at 200 Hz SOP rate of change.
- EDFA: due to high loss of the above equipment, it is necessary to compensate for the power loss and to make sure that the received power is in the optimal area to avoid artificial ROSNR penalty.
- An amplifier was used as ASE noise source and the noise level added to signal through fiber combiner through a controllable VOA.
- A fiber splitter 90% / 10 % was used to direct a portion of the optical signal to OSA in order to measure the ROSNR.
- The output of the 90% port of the splitter was connected the common port of the channel Mux/Demux.
- The output port of the Demux associated with wavelength 1546.92 nm was connected to the Rx of the transponder.

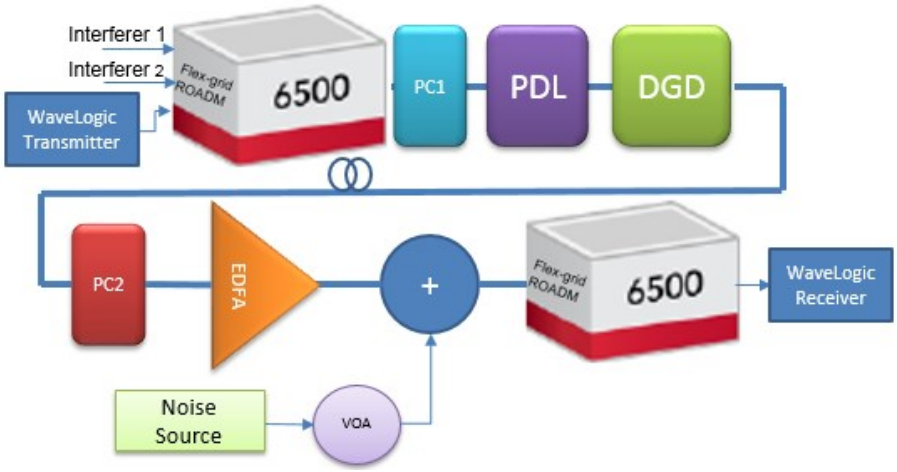

Figure 86: Experimental setup

7.5.2 - Experimental Results

When trying to squeeze channels into super-Nyquist mode of operation the penalty from linear cross-talk, which appears similar to white noise, is inevitable. Our method allows for pushing the bounds at which receiver can carry traffic. We were able to operate without any errors with the same 2 dB OSNR penalty as non-optimal method but with 1 GHz less spacing. In Fig. 87, we show how the optimized method improves the jitter margin.

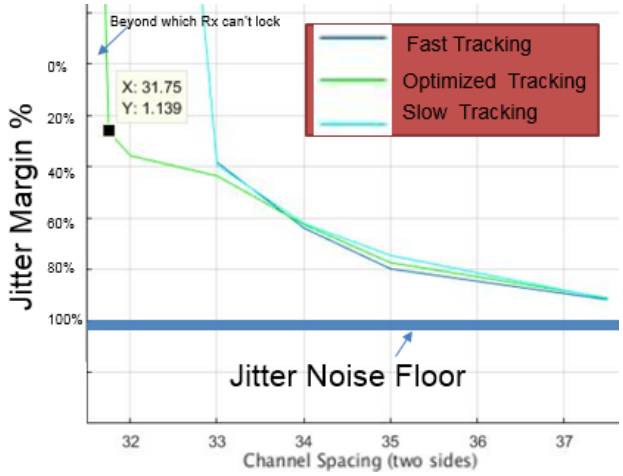

Figure 87: Optimization of jitter through setting the proper tracking

We then show, in Fig. 88, the system level benefit in terms of channel spacing with the associated OSNR penalty. We compared two circuits, legacy in Fig. 76, and our proposed circuit/method. The penalty from linear cross-talk is unavoidable, hence the increase in ROSNR penalty but it is shown that our method allows for tighter spacing in gridless setup.

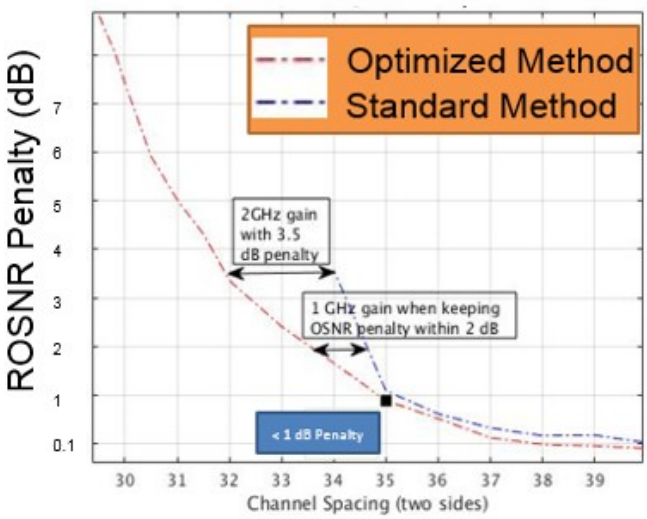

Figure 88: Results showing the advantage of the proposed optimization method

7.6 - Conclusion

We presented a novel circuit and method to optimize the channel spacing in gridless optical networks. We showed the results for 100G QPSK; however, the method was successfully tested for different data rate/modulation formats. When assuming 10 channels are propagating together,

i.e. therefore there are 9 spacings to be optimized, the experiment showed ability to gain from 9 GHz (9*1 GHz for 2 dB OSNR margin) to 18 GHz (9*2 GHz for 3.5 dB OSNR margin) in the optical spectrum for each MC.

Chapter 8 – Circuit and Technique for Measuring and Compensating Phase Interpolator Non-Linearity

"Man was born free, and he is everywhere in chains". — Jean-Jacques Rousseau

8.1 - Introduction & Literature Review

THE rapid growth of internet traffic has stimulated the development of high-speed modems in wireline, wireless and optical spaces. As stated in [180], the majority of high-speed digital wireline transceivers have their digital to analog converters' (DAC) timing controlled by a phase-locked loop (PLL). While at the receiver side, PLL and delay-locked loop (DLL) are used to extract the clock information from the data and correction is applied properly to analog to digital converters (ADC) or to digital interpolator within digital signal processor (DSP).

Phase interpolator (PI) is one of the critical components in high-speed Serializer De-serializer (SerDes) [181,182], it permits applying fine adjustment to the phase of sampling clocks. Two PI design categories are discussed in literature, current-controlled [183] and voltage-controlled [184]. The former is larger in size, while the latter is less linear. PI is used to shift clock phase within data sampling window. The controlled current-mode logic-based topology, shown in Fig. 89, is described in detail in [185]. The input consists of two clocks, having same frequency, but with 90^{o} phase difference. The weight, X is digitally controlled by a DAC. Then the granularity, number of phases, is determined by the controllable bits of the DAC and the frequency of the cross-coupled VCO. However, PI can suffer from non-linearities originating from two sources: divider mismatch between in-phase (I)-quadrature (Q) clocks and arctan effect resulting from a linear summation of a differential current mode DAC.

In [186], a PI design with increased number of phases that gives improved performance in term of linearity was introduced. However, the increase of complexity and power consumption are a burden. Other techniques such as using stages of multiple steps were proposed in [187]. In [188], a phase interpolator was demonstrated using CMOS 65 nm technology, operating at clock frequency of 2.5 GHz with improved linearity by combining two techniques: proper setting of the integration of the output signal and increasing the step size resolution. In [189], authors discussed a closed-loop circuit to estimate and continuously correct for non-linearity. The result presented, in term of residual INL, is a 10% improvement compared to [191]. The resolution of circuits

presented in literature, [186, 188, 190 and 191], are in the order of pico-seconds (ps), while our circuit is designed for femto-seconds (fs) applications.

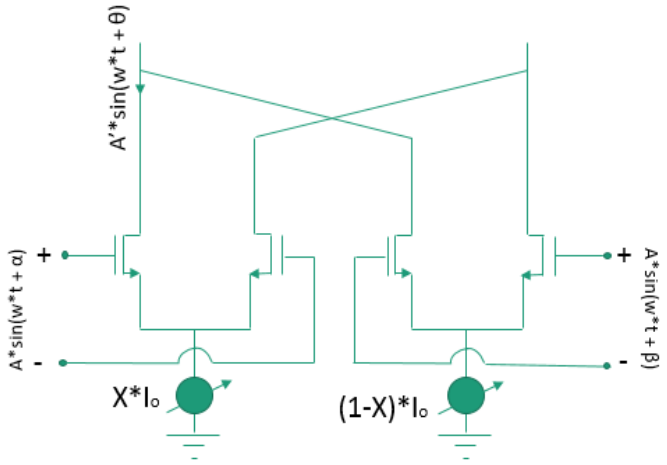

Figure 89: Differential controlled current-mode logic phase interpolator circuit

We present a digital technique that allows an extremely fine resolution (10-20 femtosecond) with an infinite phase domain dynamic range without the need for any bench top equipment such as an oscilloscope. We propose to run the calibration once (such as during optical modem integration/production) which reduces parasitics and power consumption during the operation when deployed. The paper is organized as follows. In section 8.2, we describe the source of non-linearities in phase interpolators. The test circuit and compensation method are discussed in section 8.3. In Section 8.4, we present lab results.

8.2 - Non-Linearities In Phase Interpolators

In general, the sum of two sinusoids of the same frequency but different phase is given by [192]:

$$C\sin(\omega t + \phi) = A\sin(\omega t + \alpha) + B\sin(\omega t + \beta) \quad (8.1)$$

where

$$\phi = \tan^{-1}\left(\frac{A\sin(\alpha)+B\sin(\beta)}{A\cos(\alpha)+B\cos(\beta)}\right) \quad (8.2)$$

and the amplitude C is a function of the other variables, but here we are only interested in the phase. Referring to Fig. 1, for the meaning of X, if we set $\alpha = 0$ and $\beta = -\pi/2$, $A = X$ and $B = (1 - X)$, the expression of eq. 8.2 simplifies to:

$$\phi = \tan^{-1}\left(\frac{X-1}{X}\right) \quad (8.3)$$

In Fig. 90 we show the quasi-linear shape of the output phase of phase interpolator, across one quadrant, versus 10 bits input code. For $X = 0$ the output phase is $\beta = -\pi/2$, while for $X = 1$, we get $\phi = \alpha = 0$. This is part of the transfer function of the phase rotator that we are trying to compensate (the variation from the ideal linear output-input relationship is evident).

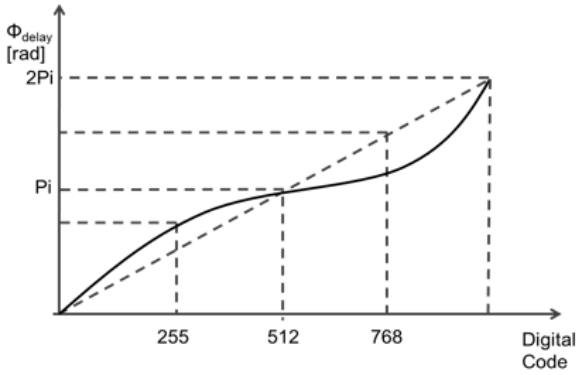

Figure 90: Digitally controlled phase rotator transfer function. Phase delay in radians vs digital input code (10 bits)

The curve in Fig. 90 illustrates the primary source of non-linearity in the phase rotator. The secondary source of nonlinearity in the phase rotator is the fact that the in-phase (I) and quadrature (Q) signals are not perfectly orthogonal in practice. This is because these signals are derived from the rising and falling edges of the VCO clock, respectively, and this clock may not have a perfect 50% duty cycle. Note that the first non-linear factor is deterministic, while the second will vary from one instance of the circuit to the next, and may even vary with temperature and time, so is more difficult to compensate for.

Beside the digital technique presented in [190], typical solutions for estimating INL in circuit is to measure phase rotator steps with an external oscilloscope which suffers from both limited time and noise resolution. Such limitations impact time-domain accuracy; especially in high-speed modems where measurements are in the order of femtoseconds. Other techniques can involve using an on-chip time-to-digital converter. All reported time-to-digital converters suffer from a limited range (do not go around 2Pi circle) and have relatively coarse resolution (in the order of picoseconds).

8.3 - Circuit & Method

We present a novel low-power built-in test circuit, implemented in 28 nm CMOS technology, that can be used in wireline transceivers using PI. In Fig. 91, we show how all the blocks are put together. With the PI being part of the PLL feedback loop at Tx, any movement in phase is

translated into a movement in the VCO clock (within PLL bandwidth). And since the loop is filtered, then the deviation injected is cleaner. The test circuit solution has the following key elements: phase interpolator, 1-bit bang-bang phase error detector, fine-resolution delay elements and a digital filter. The compensation process can be automated as software application running part of firmware bring-up to perform the measurements and apply proper compensation.

The phase rotator under test is placed in the feedback path of the main PLL. The following steps describe in detail the operation of the circuit and the methodology used in the process of compensation for non-linearity:

- A digital delay-locked loop with a 1-bit (bang-bang phase detector) locking the PLL output to the reference clock by controlling a high resolution digitally controlled delay element is used as the measuring instrument. The delay element has an ultra-fine delay step (10-20 fs) but a limited range (in the order of a few ps).

- The other phase rotator (within “test circuit”) is used to center the delay locked loop so that it settles in the middle of the range of the digitally controlled delay element.

- Applying a phase step to the phase rotator under test would force the delay locked loop to track that phase step and the accumulator controlling the digitally controlled delay element would settle to a new code (accumulator value) proportional to the phase rotator step (DNL value). To filter out jitter, the accumulator code is sampled many times and the average value is stored.

- The above process is repeated for every code step of the phase rotator under test (phase rotator in feedback path) until the digitally controlled delay elements run out of range.

- At this point, the other phase rotator (within “test circuit”) is used to “rewind” the delay locked loop so that it settles in the middle of the range of the digitally controlled delay element.

The process described above to build the DNL curve is then repeated. Summing all the DNL steps of the phase rotator would then result in the integral non-linearity (INL) of the phase rotator and can be used to pre-compensate its transfer function using a lookup table (LUT). A brute force method can be used to derive the contents of the pre-compensation LUT. It consists of searching

for the nearest word code that minimize the error INL per phase.

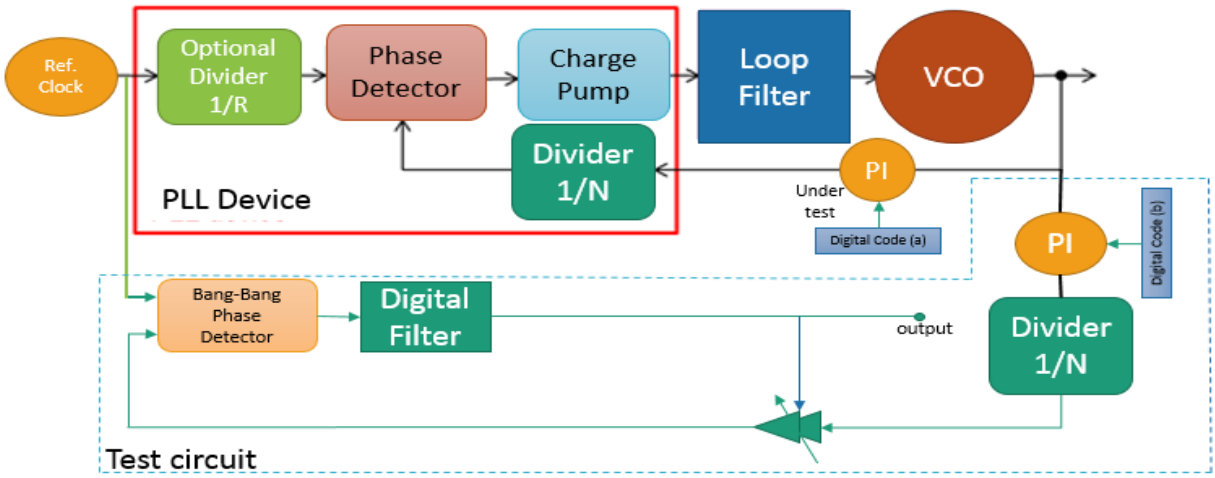

Figure 91: Phase rotator DNL & INL test circuitry.

The same divider is required in the PLL feedback path and in the test circuit so the inputs to the bang-bang phase detector are at the same frequency. If “optional divider” R > 1, then a similar divider will be introduced in the test circuit after the high-resolution delay elements.

8.4 - Results

We can see the ripple effect clearly by plotting the phase rotation error, as shown in raw plot in Fig. 92, as a function of the target phase rotation. The prototype was successfully demonstrated where the phase interpolator, used in the test chip for transmitter clock recovery circuity, has been fully characterized with an accuracy of 20 femtoseconds and then its transfer function was compensated using a lookup table.

Fig. 92 shows the error transfer characteristic curve for the same phase interpolator for both uncompensated and compensated cases, where the reported error is with respect to the ideal transfer curve for each sample. The root-mean square (rms) error is improved by 10x when the phase interpolator is properly compensated.

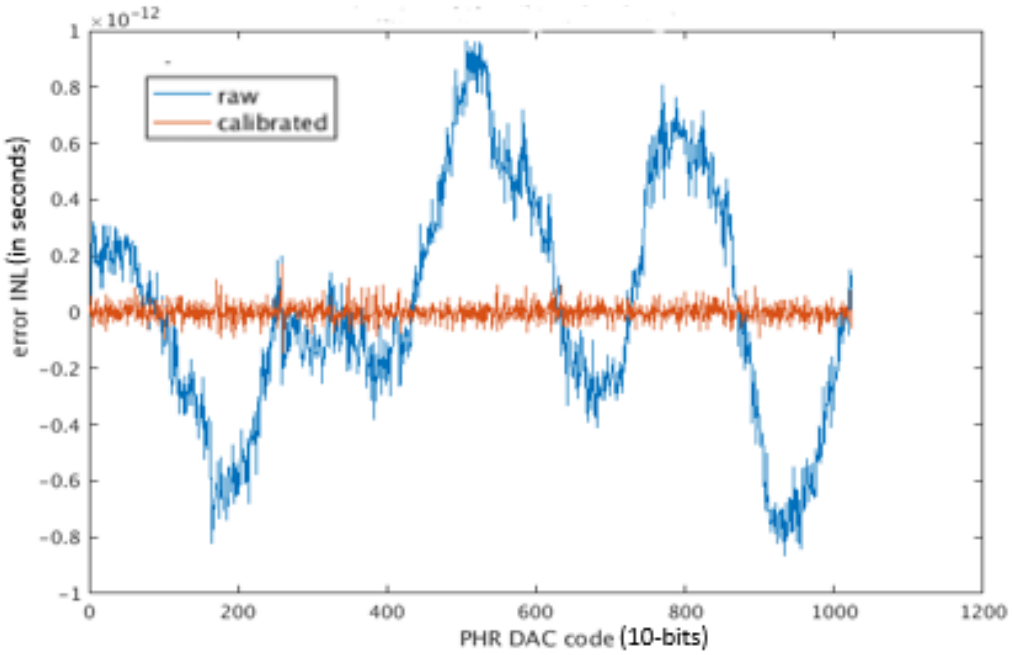

Figure 92: Measured uncompensated (blue) and compensated (red) phase interpolator error curve (x-axis: phase code, y-axis: Time placement error in seconds). Uncompensated phase rotator has rms error = 330 fs and compensated phase rotator has error of 30 fs.

8.5 - Conclusion

We introduced a novel low cost, low power and compact circuit so it can be built-into wireline transceivers. It is used to linearize PI used in high-speed clock recovery circuity such as DAC in an optical modem. The method can be used in calibration of wireline transceivers to improve system performance. We showed that a reduction of phase error, up to 10x, can be achieved.

Chapter 9 – Jitter Loading Built-In Circuit and Method to Characterize Optical Transceivers and Channels

"In the World through which I travel, I am endlessly creating myself." — Frantz Fanon

9.1 - Introduction & Literature Review

THE move from private optical networks (closed cables and transponders) to both interoperable transponders, such as white box [193] and 400G ZR [194], and open cables, as proposed for submarine applications [195], are current trends. An important aspect of optical network design is the area of network synchronization and timing, and specifically the control of jitter to ensure end-to-end reliability especially in networks that span great distances, such as those implemented for continent wide or transoceanic submarine applications. Due to the non-idealities of circuits and systems, synthesized clock has deviation [196]. The latter is manifested as phase and frequency drifting and variations. At the physical layer, to determine if a transmitted bit is 1 or 0, the recovered clock signal from data should occur at time where eye opening is maximum. Therefore, if the jitter in a system is not tracked, it can cause bit errors that degrades the performance of transmission system.

Based on ITU G810 standard, short-term timing variation, with frequency lesser than 10 Hz is called wander. For clock variations beyond 10 Hz, there are two main types of jitter: random and deterministic. As clock speed and communication channels run at higher frequencies, size of unit interval (UI, i.e. duration of each symbol) is getting smaller. For example, in 35 GBaud transmission system, the symbol duration is 28 ps while at 80 GBaud, it is 12.5 ps. Consequently, stringent specifications on jitter is unavoidable and ways to reduce the sources of jitter is a key part of nowadays' telecommunication systems. As well, it is becoming vital for network operators to have physical level tests to characterize both modems and channels. Such tests need to report information such as bit error rate (BER), noise tolerance and jitter tolerance.

In [5], due to the complexity of optical transponders, the authors described built-in functional blocks designed around the core Application-Specific Integrated Circuit (ASIC) to allow for fast system lab integration. The design for validation (DFV) methodology involves inserting test signals, probing mechanism to retrieve processed digital signals from within the ASIC and, with the help of software, post-process and visualize. The paper is generic and does not specify inserting any kind of tone to modulate clocks or how it will deal with characterizing jitter. In [197],

jitter injection at the output of charge pump of the phase locked loop (PLL) is described, where the amplitude of voltage driving the voltage-controlled oscillator (VCO) is being modulated. The drawbacks of this method are its analog nature. As well, how the charge pump is loaded which can only be high-pass since it is complementary to the main PLL loop; since the latter has a pole at DC.

As stated in [180], the majority of high-speed digital wireline transceivers have their digital to analog converters (DAC) timing is controlled by a PLL. While at the receiver (Rx) side, PLL and delay-locked loop (DLL) are used to extract the clock information from the data and correction is applied properly to analog to digital converters (ADC) or to digital interpolator within digital signal processor (DSP). For the Rx side, in [199] (and similar in [200], [201] & [202]), a circuit for on-chip measurement of period jitter and skew of clock distribution, with implementation showing 1 ps resolution, is described. Unlike in our method, it is an add-ons circuit that uses a single latch and a voltage-controlled delay element. In [203], a digital circuit implemented at the receiver to induce jitter and system tolerance is discussed. The circuit, allowing BER analysis as well with PRBS checking; however, it does not permit channel characterization.

We will describe a novel low-power circuit, implemented in 28 nm complementary metal-oxide-semiconductor (CMOS) technology, that can be used to characterize wireline transceivers and channels. The solution has three key elements: PLL with phase interpolator (PI) integrated in the feedback path used to inject a modulated eye, re-usage of existing clock recovery circuit (also called clock-data recovery circuity (CDR)) in coherent receivers for jitter reporting and a software algorithm automated to perform the measurements. This paper is organized as follow. Section 9.2 describes jitter characterization and related state of the art procedures. The new circuit and associated method are described in section 9.3. Finally, the experimental results are covered in section 9.4.

9.2 - Jitter & Its Characterization

As stated in [203], manufacturing cost of mixed-signal integrated circuits is dominated by testing. Both transmitter (Tx) and Rx have embedded PLLs to generate and synchronize clocks.

Root-mean-square (rms) jitter, phase noise integrated over interval defined by jitter mask, is typical figure of merit (FoM) for OTN and Ethernet applications. With most system using Forward Error Correction (FEC), the interval of tone frequencies over which we need to integrate in order

to estimate jitter, is driven by experiments. Rx PLLs can track variations within their designed bandwidths, while FEC frame scrambling helps at high frequencies. The out-of-band frequencies are critical that impact system performance. There is a trade-off between response time of PLLs and loop bandwidth, while the attenuation of jitter is related to bandwidth of the loop filter. PLL acts as low-pass filter upon reference clock and high-pass with respect to the VCO. Bandwidth is defined as the modulation frequency at which the PLL starts losing lock with respect to reference.

In the context of optical transponders, the design criteria for a receiver must be considered of all aspects: the transmit SerDes, digital phase locked loop (PLL), optic driver/receiver and the fiber channel, including switching nodes. Two levels of jitter characterization, node and system, exist. Jitter characterization at the system level (such as protocols SONET, OTN, SDH, …) looks at the total node to node contribution. Testing is required between telecom equipment in a network, difference in frequency in clock domain can be absorbed by first-input first output (FIFO) buffering. It is assumed that the individual cumulative contributions of the nodes (transponders and switches) are characterized as part of the node level characterization exercise. In transmission system, there are three jitter transfer behaviors that can be used to describe the effect of the transfer function on the clock:

- Jitter generation: is the amount of jitter added to signal sampled with clean clock. The source of jitter could be random or deterministic.
- Jitter transfer: is ratio of the output jitter over the input jitter, expressed in terms of dBc, gain using the carrier as the reference.
- Jitter tolerance: is a specification to indicate how much jitter the system can tolerate at the input while maintaining a desired performance at the specific BER.

On the testing side, “jitter tracking and tolerance” test is required. It characterizes the ability of the Rx clock recovery circuit to track jitter within its loop bandwidth. It generates a mask over frequency band of interest. The y-axis is the power level of the phase noise versus frequency offset (Δf) at x-axis, relative to power level of the carrier:

$$L(f)_{dBc} = 10 * log_{10}[\frac{power\ of\ 1\ Hz\ band\ @\ offset\ (\Delta f)}{power\ @\ carrier}] \qquad (9.1)$$

One key application for jitter characterization is evaluating multi-gigabits per second serializers/de-serializers (SerDes). performance. The two main related electrical parameters that go into datasheet are the jitter of the transmitter at giving BER and the ability of the receiver to track jitter at a given BER. Both serializer and DAC are driven by Tx clock generated by PLL, and

both de-serializer and ADC are driven by Rx clock generated by CDR which includes a PLL. In both modules, reference clock is used to synchronize clocking information extracted from incoming data. Within the PLL, in most cases, passive loop filter is used because it is low cost and easy to implement.

The phase noise comes from the thermal noises of the resistors. Modeling the phase noise of the different SerDes components, extracting the time jitter and decomposing it, would help designers to achieve desired Figure of Merit (FoM) for future SerDes. Generating white and colored noise synthetic jitter patterns would allow to better analyze the effect of jitter in a system for design verification. The jitter tolerance (used in SONET), used to derive jitter mask, test takes different names based on the standard, such as stressed eye in optical or sinusoidal interference in 10GbEthernet. The SONET specification does not currently define the split between the optics and the SerDes. The Jitter Mask defines two different areas: In-Band jitter (tracked by CDR at receiver but contains phase noise) and out-of-band jitter which is beyond the tracking loop and it is the critical portion that impacts BER. The total out-band jitter is composed of random and further deterministic content.

Both jitter generation and tolerance testing have to be performed over different temperature ranges. Due to thermal noise, random jitter (RJ) is always there and can be measured as noise floor in the phase noise plot. RJ can have both white and colored noise properties. In [203], it is found that RJ represents the noise in the clock signal; while Deterministic Jitter (DJ) is a result of circuit bandwidth effects and other sources such as interference, crosstalk, and impedance mismatch. In [205], a white noise generation approach was introduced. DJ is bounded because it has well defined minimum and maximum extends and is specified as peak-to-peak value. Total jitter (TJ) is a linear combination of RJ as a function of BER, and DJ, as described in [206].

The link model is a combination of Tx, channel and Rx. The stream of symbols is generated at the Tx and the receiver uses maximum-likelihood or minimum distance methods to decide on the received symbol. When looking at the eye-diagram, the width of the eye is determined by jitter while the heights is dominated by noise (defined within BER level). In high-end bit-error-ratio tester (BERT) testers (such as Agilent N4903A), allows all sort of composition of jitter (RJ, DJ, and Sinusoidal Jitter) to create both realistic and worse case stress condition. As well, it is expected that they have ultra-low intrinsic jitter. They do indeed come with automated jitter tolerance characterization that searches for the maximum jitter value the receiver tolerates by

sweeping SJ (that looks like electromagnetic interference) in modulation frequency and magnitude. Test equipment for creating eye diagrams requires a BERT that generates pseudo-random repeating test patterns. BERT testers usually have multiple trigger choices. For example, a “clock trigger” provides a classical eye diagram that implements all possible bit transitions in one display. In Fig. 93, we show the typical setup used to test jitter tolerance of a device under test (DUT).

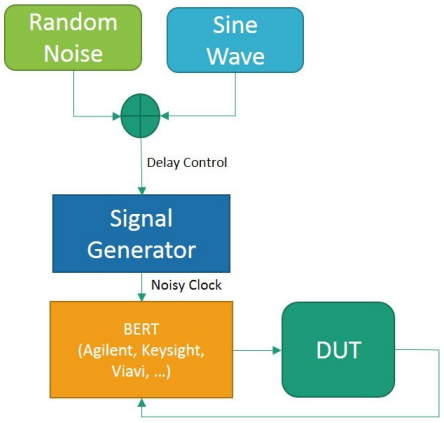

Figure 93: Typical BERT-based Jitter Testing Setup

Two categories for testing jitter methods exist:

- Time domain: measurement is done using high-frequency digital oscilloscopes that have the capability of high single-shot sampling bandwidth.
- Frequency domain: spectrum analyzer will display phase noise expressed as single-side noise-to-carrier ratio L(Δf), representing power-spectral density versus frequency offset Δf relative to the carrier. It illustrates both random noise level and spurs.

Therefore, the jitter tolerance mask is meant to test the CDR’s tracking ability (as described in Telcordia’s GR 253, section 5.6.2.2.2). In standards, such as in [207], the frequency intervals for different network protocols are defined:

- SONET OC-3/12/48: 12 KHz to 20 MHz
- SONET OC-192 : 50 KHz to 80 MHz
- Fiber Channel : 637 KHz to 10 MHz

Converting from Phase noise profile (*L*(f)), to rms jitter is done by integrating over the whole band of frequencies using formula presented in [208]:

$$RMS_{jiiter} = \frac{1}{2*\pi* F_c}\sqrt{2 * \int_0^{\bowtie} 10^{\frac{L(f)}{10}}\, df} \qquad (9.2)$$

9.3 - Circuit & Method

In this section, we present a circuit that is low cost, low power and low foot-print so it can be built-into wireline transceivers that can generate jitter with fine resolution. It is deterministic since it is programmed in a look-up table (LUT). However, it can have any distribution (Gaussian, sinusoidal …) and any power spectral density. It is limited by Tx PLL bandwidth. It provides control of jitter amplitude in seconds or unit intervals, waveform type (sine, square, or noise) and frequency. The system, with high-level description shown in Fig. 94, can be used to characterize one of the three components in optical links as follows:

Rx: using golden (i.e. either has low jitter or known jitter) Tx, back to back fiber (Application: any modem, as example 400GZR [2] – interoperability).

Tx: using golden (i.e. either has low jitter or known jitter) Rx, back to back fiber (Application: any modem, as example 400GZR [2] – interoperability).

Optical Channel: using both golden Tx and Rx (Application: Open Cables [194] where characterizing jitter tolerance of wet plant using golden Submarine Line Terminating Equipment (SLTE) can help setting requirement for plant, where our modems are installed, and eventually setting pricing/allowing to compare wet plants).

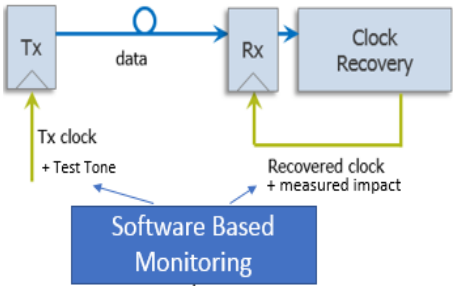

Figure 94: System-level view of method

The solution has three key elements: PLL with phase interpolator (PI), Fig. 95 (same as in Fig. 89), integrated in the feedback path used to inject a modulated eye, re-usage of existing clock recovery circuit (also called clock-data recovery circuity (CDR)) in coherent receivers for jitter

reporting and a software algorithm automated to perform the measurements.

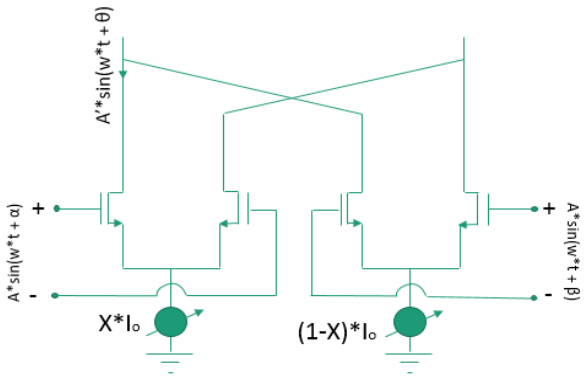

Figure 95: Differential controlled current-mode logic phase interpolator circuit

Phase interpolator is used to shift clock phase within data sampling window. The controlled current-mode logic-based topology is described in great details in [209]. The input consists of two clocks, having same frequency, but with 90° phase difference. The weight, X is set by digitally controlled by a DAC. Then the granularity is determined by the resolution of the DAC (number of controlled bits) and the frequency of the cross-coupled VCO. The phase modulator output is non-linear due to trigonometric element:

$$\Phi = tan^{-1}(\frac{X}{1-X}) \qquad (9.3)$$

The idea in the jitter injecting process is that, at the Tx, we are deliberately widening the transition areas in the eye-diagram. With original clock having the following model:

$$sig = \alpha * \cos(w_c * t) \qquad (9.4)$$

where α is the amplitude of the signal and $w_c = 2 * \pi * F_c$ (carrier frequency). The noisy signal, or phase modulated version, is the original signal with added phase noise. It takes the form of:

$$sig_{noisy} = \alpha * \cos(w_c * t + \beta * \cos(w_m * t)) \qquad (9.5)$$

where β is the amplitude of the jitter and $w_m = 2 * \pi * F_m$ (modulation frequency). The equivalent jitter is seconds, peak-to-peak is defined as:

$$Jitter_{pp,seconds} = \frac{2 * \beta}{2 * \pi * F_c} \qquad (9.6)$$

The second key component is the phase error detector at the Rx to estimate the jitter. It is worth noting that the method re-uses the circuits available in typical Rx for clock recovery (including jitter approximation) and BER/FER estimations. For the former method such as Gardener based detector [32] can be used, where the timing error detected for the kth symbol is given by:

$$e(k) = a_I(k) + a_Q(k) \qquad (9.7)$$

Where:

$$a_I(k) = \{y_I((k-1)T + d_{k-1}) - y_I(kT + d_k)\}y_I(kT - {}^{T}/_{2} + d_{k-1})$$

$$a_Q(k) = \{y_Q((k-1)T + d_{k-1}) - y_Q(kT + d_k)\}y_Q(kT - {}^{T}/_{2} + d_{k-1})$$

And T is the period of symbol, d_k is the estimate of the phase at kT and y_I and y_Q are the received in-phase and quadrature components.

Based on the above, the method can be viewed as a low cost and built-into transceivers as jitter-loading mechanism. Controlling the PI, with its small instantaneous phase deviation, makes it possible to inject jitter at high resolution. With the PI being part of the PLL feedback loop at Tx, any movement in phase is translated into a movement in the VCO clock feeding the DAC. In Fig. 96, we put all blocks together with more details. Most of the components are used in typical serial links as shown in [210]. In the case of optical link, the Electro-Optic (EO) converters are required after the DAC. We used an interleaved ADC as described in [169]. The state machine, in the control block, based on register settings allows different reading rate of the content of the look-up-table. Such methodology permits the modulation of the Tx clock with a large range of carrier frequency at different amplitude. Comparing to [211], we are able to generate any form of phase signal, and not just square wave. As well, the fact that the PI is in the feedback path of the PLL, the injection is clean.

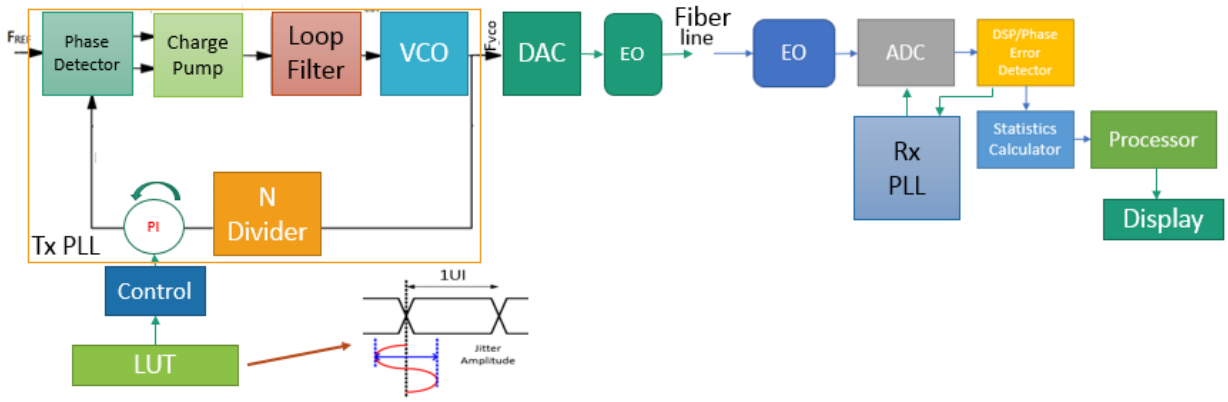

Figure 96: Detailed view of both Tx and Rx circuits

A proof of concept model, Fig. 97 & 98, was tested in Simulink © 2016a as part of the design activity. It is showing a s-domain behavior model of an analog PLL and phase delay element driven by a DAC to modulate the feedback signal going into the frequency divider. The stability of the whole PLL was studied rigorously as shown in chapter 7.

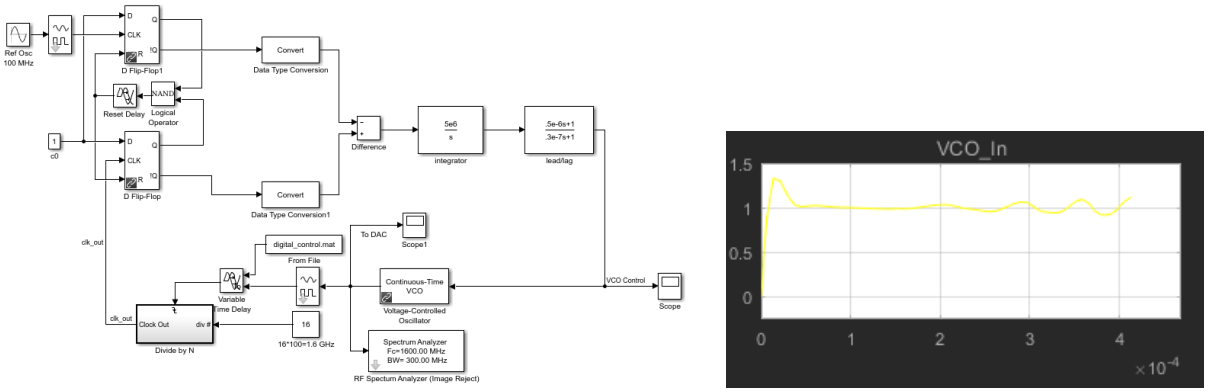

Figure 97: Simulink Model with Clocking Amplitude to Phase Modulation & VCO control ramping to achieve steady state

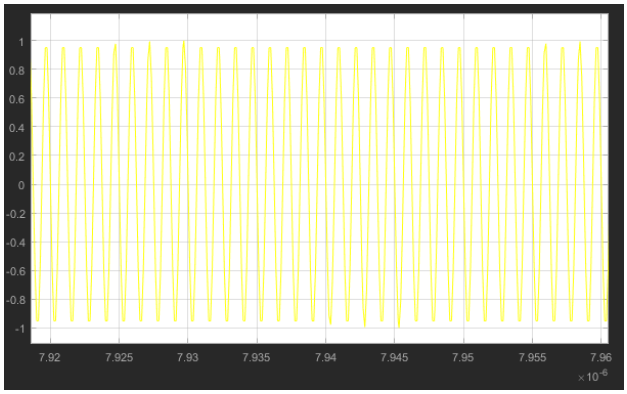

Figure 98: VCO output driving DAC clock

The method and circuit can program one tone or multi-tone on both the transmitter. Anything with jitter signature with link or transceiver can be characterized. And the automated tool is able to produce a jitter mask based on fixed jitter at the Tx, or until certain metric threshold is crossed at the Rx. The remaining functionality shown in Fig.99, automated in Matlab now, can be turned into software implementation. The following list of metrics can be used as reference for jitter characterization:

A. A target BER
B. Reach error level at FEC

C. Measured rms of jitter

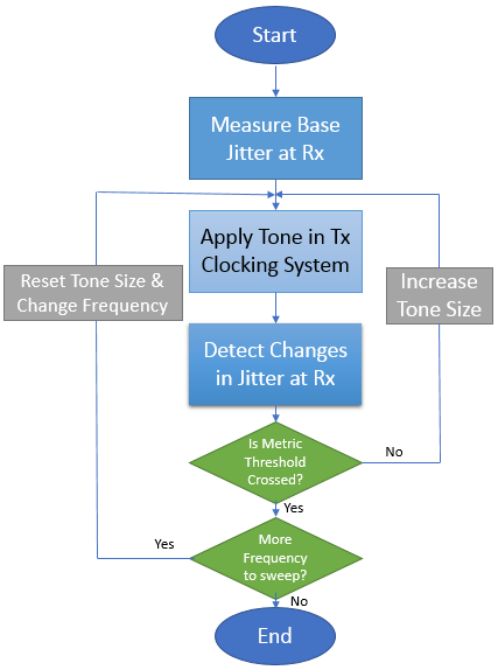

Figure 99: Flow chart of the automation method used

9.4 - Results

One of the major electrical parameter used to characterize integrated circuits and systems performance is, at a given BER, the Rx ability to track jitter. It can be characterized either as rms value in time domain, or spectral density over bandwidth (dB/Hz) in frequency domain. We used a back to back configuration, i.e. Tx output directly connected to Rx with patch fiber and a Tx with low intrinsic jitter. In Fig. 100, we are summing three sinusoidal waveforms, with same amplitude, at different frequencies. We show the time-domain waveform programmed into the 1024 entries of the on-chip LUT. The jitter resulting from the tone is calculated as follow:

$$Spurious\ Tonal\ Jitter = \frac{10^{Lspur/20}}{\pi f_0} \qquad (9.11)$$

And since it is independent of the exiting jitter sources, the total jitter is derived as follow:

$$Total\ Jitter\ = (Integrated\ Noise\ Jitter^2 + \ Spurious\ Tonal\ Jitter^2)^{1/2} \qquad (9.12)$$

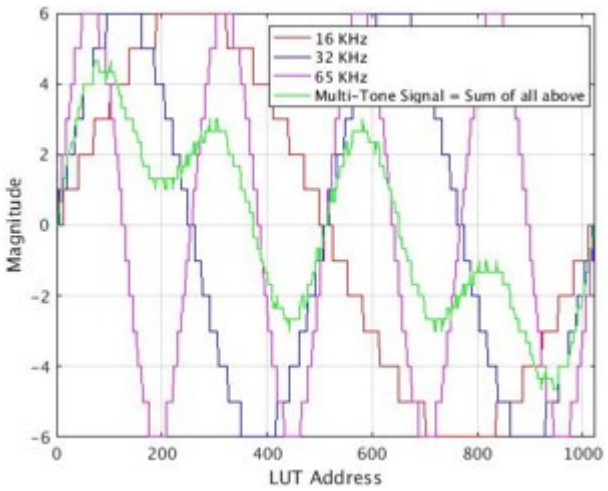

Figure 100: Example of multi-tone waveform programmed in LUT

Using spectrum analyzer, we probed clock signal at the VCO going into the DAC. In Fig. 101, the output of single sideband phase noise profile is shown with the tones appearing, in frequency domain, added on top of the existing phase noise spectrum (in red) versus the blue curve without jitter injection. Although jitter is not sinusoidal in nature in real systems, we inject sinusoidal tones because of the ability to reproduce same deterministic waveforms and comparing tolerance masks of different systems.

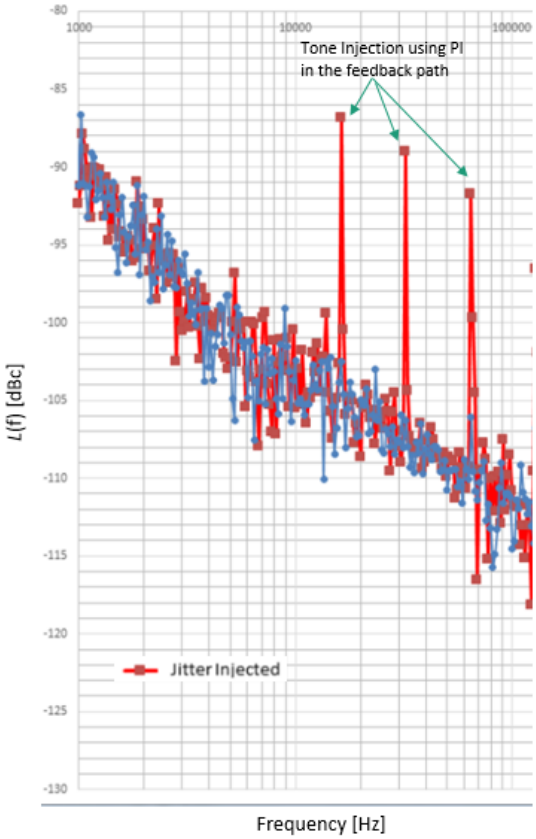

Figure 101: Measured phase noise with and without injected tones

In Fig. 102, we inject one sinusoidal tone at the time. The goal is to characterize the tolerance of the Rx to lock to the upstream PLL and track jitter. As you can see, due to the low-pass nature of the CDR circuit, the Rx is able to track high-amplitude tones at the low frequencies, then the tolerance gets smaller until it reaches a noise floor. At high frequencies, the variations are too fast for Rx to track, hence less tolerance and only small amplitude tones can be handled. Changing CDR bandwidth at the Rx will result in shift of the mask presented. The lower the bandwidth the less phase noise we are letting in, but at the price of less tracking capability.

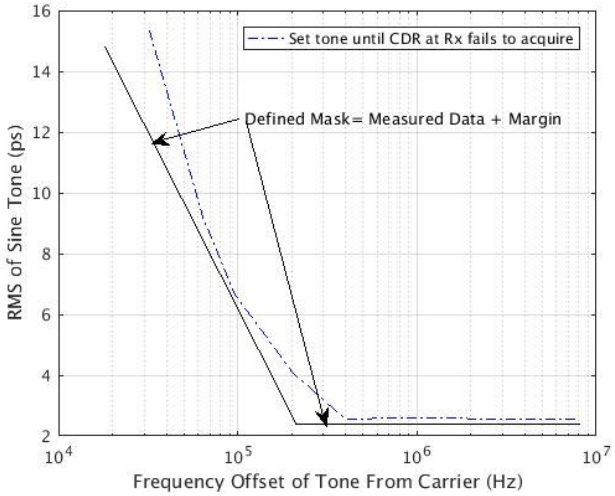

Figure 102: Jitter tolerance mask for a given CDR settings

9.5 - Conclusion

We presented a circuit and an associated method to induce jitter at clock recovery circuity in a wireline Tx and use it to characterize different modules in an end-to-end layer 0 optical transmission system. The novelty of the method is in introducing the phase interpolator at the Tx clock circuity to allow for jitter generator by providing control of jitter amplitude in seconds or unit intervals, waveform type (sine, square, or noise) and frequency.

Chapter 10 – Conclusion & Future Work

"I do not fear death. I had been dead for billions and billions of years before I was born, and had not suffered the slightest inconvenience from it." — Mark Twain

10.1 - Conclusion

In this thesis, we investigated three different aspects all related to high-speed coherent receiver technology in optical networks. Since the chapters are dealing with segregated problems, our conclusions for the work presented in each chapter separately:

Chapter 4: First, we studied the performance of LMS adaptive filter, in the context of dual-polarization coherent optical receivers, in presence of SOP transients, PDL and ROADMs. The trade-off between tracking capability and implementation noise when choosing the step size and forgetting factor is a key design decision, we showed how the higher the step size the more SOP tracking the adaptive filter will be handling but at the price of higher B2B/PDL ROSNR. The higher the order the modulation formats the less tracking can be done, a reduction of 30% expected for every extra bit per symbol. Error signal feedback delay is a key bottleneck for higher SOP tracking, we showed due to higher BER oscillatory behavior that a delay of 40 blocks of 512 symbols can reduce tracking by 50% compared to FD of 20 blocks. As well, for each one dB PDL increase in link, we lose 7.1 KHz and 8.6 KHz for SNR penalty of 1 and 2 dB respectively. Finally, we presented the impact of concatenating ROADMs on SOP tracking. The RLS algorithm, using a covariance matrix as an aggressive dynamic "step size", has an advantage over the LMS and NLMS algorithms in both convergence speed and tracking in steady state in presence of PDL (and other colored noise) in the fiber. Our simulation data showed that RLS is ~2.5x faster than LMS when comparing convergence speed at 6 dB PDL with fast and slow SOP rotations. NLMS, using the trace of the covariance matrix, is around 2x slower than RLS. For SOP tracking, all studied algorithms have similar performance without presence of colored noise. Otherwise, RLS outperforms MMA, NLMS and LMS. On the other hand, RLS complexity growth, as a function of filter length, is quadratic $O(L^2)$, unlike LMS family which increases in linear fashion. The length of the filter governs how much PMD the receiver is designed to compensate for. It is worth noting that choosing one of the algorithms depends on the application. For example, the case of Data Center Interconnect of 100 KMs will not have considerable PDL in the link and the requirement for low power consumption is rigid; therefore, LMS/MMA (or sign-LMS) can be a good choice.

Chapter 5: We presented a new method to perform an adaptive joint Tx/Rx compensation, of stringent filtering effected caused by CMDs and ROADMs in fixed-grid optical networks, while using typical HW blocks in coherent transponder. The only requirement is the availability of communication channel between Tx and Rx. When a Rx that is not matched to the Tx pulse shape and optical channel can result in insufficient electrical bandwidth and noise enhancement. Proposed method in Section V leverages Tx and Rx static filters compensation capability, of the channel frequency response, such that they effectively constitute a matched filter pair hence maximizing SNR at the input of the Rx adaptive filter. With filtering models representing real optical networks and components, and PDL, we showed an improvement in system performance. With 18xWSSs scenario, both simulation and lab measurements showed a gain of 0.6 and 0.33 dB, respectively, in ROSNR at BER of 2% versus doing post-compensation only. We showed for the first time, to the best of our knowledge, that splitting the compensation of heavy filtering in real deployment scenarios, is better than doing Tx pre-compensation. That is especially the case in presence of implementation noise at transmitter, limited ENOB of DAC, clipping of coefficients in transmitter filter and noise in Tx analog chain. With 18xWSSs scenario, both simulation and lab measurements showed a gain up to 0.5 and 0.15 dB, respectively, in ROSNR at BER of 2% versus doing pre-compensation only.

Chapter 6: We studied the impact of bandwidth loss of SiPh MZ modulators in coherent receivers. We showed that our proposed MMSE gradient-descent based method provides 0.5 dB of ROSNR reduction for 60GHz channel when decay of modulator TF is 6 dB at 30 GHz. We presented system benefits of not doing full pre-compensation at the Tx signal processor. As well, we showed that when squeezing channels in gridless networks, using joint compensation provides a reduction of 0.1 dB to the probe channel when squeezing both neighbors by 2 GHz.

Chapter 7: A methodology to allow for less spacing between channels travelling in same MC, by mitigating jitter more effectively even in presence of phase noise in PLL, was presented. The work was done using WaveLogic3 © coherent transponder at Ciena © Cooperation. Part of the work was studying, in-depth, the subject of clock recovery in coherent receiver. The theoretical concept was supported by simulation to get the fitting models and basic requirements to guide a high-level software application in the optimization process. Then, lab experiments showed that with available OSNR margin, up to 18 GHz of optical spectrum can be saved in each NMC consisting of 10 channels. Depending on the baud-rate, that can be translated to one extra channel running at 35 Gbaud for every two NMC. It is expected that network providers assume at least 3 to 4 dB OSNR

margin at early deployments to account for end-of-life degradation in modems and fiber aging. Hence, our approach allows operators to take advantage of the margin to increase the capacity of their links.

Chapter 8: We introduced a novel low cost, low power and compact circuit so it can be built-into wireline transceivers. It is used to linearize PI used in high-speed clock recovery circuity such as DAC in an optical modem. The method can be used in calibration of wireline transceivers to improve system performance. We showed that a reduction of phase error, up to 10x, can be achieved.

Chapter 9: We presented a circuit and an associated method to induce jitter at clock recovery circuity in a wireline transmitter and use it to characterize different modules in an end-to-end layer-0 optical transmission system. The novelty of the method is in introducing the phase interpolator at the transmitter clock circuity to allow for jitter generator by providing control of jitter amplitude in seconds or unit intervals, waveform type (sine, square, or noise) and frequency.

10.2 – Future Work

Same as above, we will present the potential future related research activities in a modular form:

Chapter 4: First and foremost, matching the simulations with lab experiments is always desirable to help gain more confidence on the validity of the channel and receiver simulated model. As well, such activity will involve stressing other blocks, such as carrier recovery, and checking the overall performance as part of the tracking process. Comparing tracking performance with Constant Modulus Algorithm (CMA), with and without colored noise, would complete the picture since CMA is widely used in coherent space. Mixing data-directed with pilot-directed and showing how much improvement we can get. Looking at LMS with (some kind of) whitening and testing that against RLS to see if we can improve the tracking capability in presence of PDL.

Chapter 5: We don't believe that the fiber type would make a difference while operating at low input power i.e. being in the linear transmission regime; however, since the spectrum of the signal transmitted is not flat with the pre-compensation part of the method, looking at the effect of non-linearity (both SPM with signal channel propagation and XPM in DWDM link) would be desired.

Chapter 6: A plan was discussed with Dr. David Plant, from McGill university, to use his laboratory for conducting experiments that mimic the simulations. We will compare the results to simulation in back to back configuration, as well, in fiber propagation scenarios for up to 120 km.

Chapter 7: Using the introduced method, it is desirable to perform some of the trials with high-input power where the receiver is experimenting some non-linearity is worth investigating; as well, using different fiber types with various dispersion mapping. Although for data-center interconnect and metro applications, this might not be required since the launch power is not typically high.

Chapter 8: The method was tested with only two PLLs having phase interpolators in the feedback path. Therefore, it is worth applying the method to circuits built with new technologies, where analog libraries are not mature, such as 7 nm. The latter is inherently noisier and prune to mis-match between components.

Chapter 9: A graphical user interface to ease the use of the method is of great interest. As well, testing different fibers with commercial cards, is beneficial for cases where interoperation between different vendors is required, as 400G ZR.

Appendix A: Matrices of Weiner-Hopf Equations

Let M be dimension of the vector:

$$r(n) = [r(n) \quad r(n-1) \quad \dots \quad r(n-(M-1)]$$

Then

$$\mathbf{R}_{rr} = E[\boldsymbol{r}\,\boldsymbol{r}^H]$$

$$= \begin{bmatrix} R_{rr}(0) & \cdots & R_{rr}{}^*(M-1) \\ \vdots & \ddots & \vdots \\ R_{rr}(M-1) & \cdots & R_{rr}(0) \end{bmatrix}$$

With

$$R_{rr}(0) = E[r(n)\,r(n)]$$

$$R_{rr}(1) = E[r(n)\,r(n-1)]$$

and so on …

Let's call $\boldsymbol{R}_{sr,i}$ the cross-correlation function between $s(n)$ and $r(n-i)$:

$$\boldsymbol{R}_{sr,i} = E[s(n)r(n-i)]$$

$$\mathbf{R}_{sr} = E[\boldsymbol{s}\,\boldsymbol{r}^H]$$

$$= (\boldsymbol{R}_{sr,0}, \boldsymbol{R}_{sr,1}, \dots, \boldsymbol{R}_{sr,M-1})^T$$

Appendix B: Impact of Jitter on SNR versus Frequency

The variation of a signal, s(t), over small deviation in time is defined as:

$$\frac{\Delta s}{\Delta t} = s(t)'$$

The error in amplitude due to jitter is derived as:

$$\Delta s = (s(t)')\,\Delta t$$

The resulting equivalent MSE is:

$$E[\Delta s^2] = E[(s(t)')^2 \Delta t^2]$$

$$= E[(s(t)')^2]\,E[\Delta t^2]$$

$$= E[(s(t)')^2]\,(Jitter_{rms})$$

SNR due to jitter is equal to:

$$SNR_{jitter} = \frac{E[(s(t)\ )^2]}{E[(s(t)')^2]\,(Jitter_{rms})}$$

In frequency domain, each bin is sinusoidal tone. Defining $s(t)$ as sine function:

$$s(t) = A\sin(2\pi f)$$

Then,

$$E[(s(t)\ )^2] = {}^{A^2}/_{2}$$

And the derivative is,

$$E[(s(t)')^2] = {}^{(2\pi A f)^2}/_{2}$$

Back to the SNR,

$$SNR_{jitter,linear} = \frac{{}^{A^2}/_{2}}{(Jitter_{rms})\ {}^{(2\pi A f)^2}/_{2}}$$

$$= \frac{1}{(Jitter_{rms})\,(2\pi f)^2}$$

The higher the frequency, the more the jitter would impact the SNR as shown in simulation below.

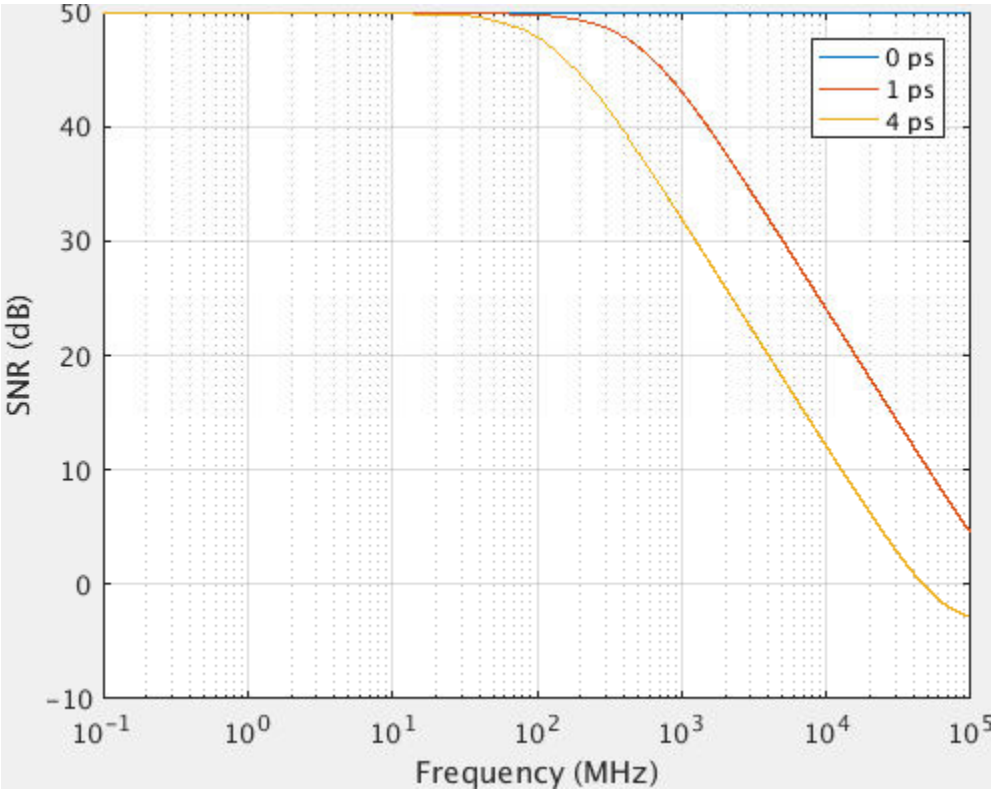

Bibliography

[1] Han Sun, et al., "Real-time measurements of a 40 Gb/s coherent system," Opt. Express16, 873-879 (2008)

[2] Kim Roberts and al, "Roadmap of optical communications", J. Opt. 18 (2016) 063002 (40pp) doi:10.1088/2040-8978/18/6/063002

[3] Cisco 2015 'The zettabyte era: Trends and analysis', white paper http://cisco.com/c/en/us/solutions/collateral/service-provider/visual-networking-index-vni/VNI_Hyperconnectivity_WP.html, Accessed: 11/August/2018

[4] "The Twentieth Century" http://www.fiber-optics.info/history/P2, Accessed: 11/August/2018

[5] "Only Connect: A guide to fiber optics", https://tinyurl.com/y7tgt6k4, Accessed: 11/August/2018

[6] E.Desurvide et al, "High gain erbium-doped traveling-wave fiber amplifier", Optics Letter, vol 12, No 11, November 1987.

[7] S.V. *Manakov et al., "*On the complete integrability of a nonlinear Schrödinger equation". Journal of Theoretical and Mathematical Physics. *19 (3): 551–559,* June 1974.

[8] D. Marcuse, "Application of the Manakov-PMD equation to studies of signal propagation in optical fibers with randomly varying birefringence", J. Lightwave Technol., vol. 15, no. 9, pp. 1735-1745

[9] Elie Awwad et al, "Polarization-time coding for PDL mitigation in long-haul PolMux OFDM systems", Optics Express**,** Vol. 21,, Issue 19, pp. 22773-22790, (2013).

[10] S. O. Arik, et al., "MIMO Signal Processing for Mode-Division Multiplexing: An overview of channel models and signal processing architectures," in *IEEE Signal Processing Magazine*, vol. 31, no. 2, pp. 25-34, March 2014.

[11] G.P. Agrawal, "Nonlinear Fiber Optics", Academic Press, 2001

[12] Galtarossa**,** Menyuk **(**Editors**),** "Polarization Mode Dispersion", Springer, 2005

[13] J.H. Winters, R.D. Gitlin, "Electrical signal processing techniques in long-haul fiber-optic systems", IEEE Transactions on Communications, Vol.38, No. 9, September 1990.

[14] J.C. Cartledge, R.G. McKay, M.C. Nowell, "Performance of smart lightwave receivers with linear equalization", Journal of Lightwave Technology, Vol. 10, No. 8, August 1992.

[15] J. Yu, “17 Tb/s (161 x 114 Gb/s) PolMux-RZ-8PSK transmission over 662 km of ultra-low loss ber using C-band EDFA ampli_cation and digital coherent detection", in Optical Communication, 2008. ECOC 2008. 34th European Conference on, Paper Th.3.E.2, sept. 2008.

[16] X. Zhou, et al., “32Tb/s (320x114Gb/s) PDM-RZ-8QAM transmission over 580km of SMF-28 ultra-low-loss ber", in Optical Fiber Communication, 2009. OFC 2009.

[17] T. Kobayashi, et al., “100x120-Gb/s PDM 64-QAM transmission over 160 km using linewidth-tolerant pilotless digital coherent detection", in Optical Communication (ECOC), 2010 36th European Conference and Exhibition , sept. 2010.

[18] D. Qian, et al., “101.7-Tb/s (370x294-Gb/s) PDM-128QAM-OFDM transmission over 3x55-km ssmf using pilot-based phase noise mitigation", in Optical Fiber Communication Conference and Exposition (OFC/NFOEC), 2011 and the National Fiber Optic Engineers Conference, Paper PDPB5, march 2011.

[19] A. Sano et al., “102.3-Tb/s (224 x 548-Gb/s) C- and extended L-band all-raman transmission over 240 km using PDM-64QAM single carrier FDM with digital pilot tone", in Optical Fiber Communication Conference and Exposition (OFC/NFOEC), 2012 and the National Fiber Optic Engineers Conference, Paper PDP5C.3,march. 2012.

[20] D. E. Crivelli *et al*., "Architecture of a Single-Chip 50 Gb/s DP-QPSK/BPSK Transceiver With Electronic Dispersion Compensation for Coherent Optical Channels," in *IEEE Transactions on Circuits and Systems I: Regular Papers*, vol. 61, no. 4, pp. 1012-1025, April 2014.

[21] Peter Schvan, et al., “A 24GS/s 6b ADC in 90nm CMOS”, *ISSCC Dig. Tech. Papers, pp. 544-545, February 2008.*

[22] C. Laperle, “Advances in high-speed ADCs, DACs, and DSP for optical transceivers,” in Optical Fiber Communication Conference and Exposition and the National Fiber Optic Engineers Conference (OFC/NFOEC), 2013. IEEE, 2013, p. OTh1F.5.

[23] J. G. Proakis and M. Salehi, Digital Communications, 5th ed. (McGraw Hill, 2007)

[24] A. Ghazisaeidi, et al., "System benefits of digital dispersion pre-compensation for non-dispersion-managed PDM-WDM transmission," Optical Communication (ECOC 2013), 39th European Conference and Exhibition on, London, 2013, pp. 1-3.

[25] J. C. Cartledge, et al. "Compensation of Polarization Dependent Loss by Optimizing the Transmitted State-of-Polarization for 140 Gbit/s DP-QPSK," SPPCom, OSA Technical Digest , SpM3E.4.

[26] Kim Roberts et al., “Electronic precompensation of optical nonlinearity”, IEEE photonics letter 18, 403-405, (2006)

[27] H. Bulow, et al., "Electronic Dispersion Compensation," in *Journal of Lightwave Technology*,

vol. 26, no. 1, pp. 158-167, Jan.1, 2008.

[28] D. McGhan *et al*., "Electronic dispersion compensation," *2006 Optical Fiber Communication Conference and the National Fiber Optic Engineers Conference*, Anaheim, CA, 2006.

[29] K. Roberts, "Electronic Dispersion Compensation Beyond 10 Gb/s," *2007 Digest of the IEEE/LEOS Summer Topical Meetings*, Portland, OR, 2007.

[30] S. J. Savory, "Digital filters for coherent optical receivers," Opt. Express 16(2), 804–817 (2008)

[31] M. Oerder and H. Meyr, "Digital filter and square timing recovery," IEEE Trans. Commun. 36(5), 605–612 (1988).

[32] F. Gardner, "A BPSK/QPSK timing-error detector for sampled receivers," IEEE Trans. Commun. 34(5), 423– 429 (1986).

[33] D. Godard, "Passband timing recovery in an all-digital modem receiver," IEEE Trans. Commun. 26(5), 517–523 (1978).

[34] J.H. Winter, "Equalization in Coherent Lightwave Systems Using a Fractionally Spaced Equalizer", Journal of Lightwave Technology, Vol.8, No. 10, October 1990.

[35] C. Zhu, A. V. Tran, C. C. Do, S. Chen, T. Anderson and E. Skafidas, "Digital Signal Processing for Training-Aided Coherent Optical Single-Carrier Frequency-Domain Equalization Systems," in *Journal of Lightwave Technology*, vol. 32, no. 24, pp. 4712-4722, 15 Dec.15, 2014.

[36] E. Ip, et al., "Feedforward Carrier Recovery for Coherent Optical Communications", Journal of Lightwave Technology 27, 2552-2553 (2009).

[37] I. Fatadin et aI., "Laser Linewidth Tolerance for 16-QAM Coherent Optical Systems Using QPSK Partitioning", IEEE Photonics Technology Letters 22, 631-633 (2010).

[38] Li et al., "Laser-Linewidth-Tolerant Feed-Forward Carrier Phase Estimator With Reduced Complexity for QAM", Journal of Lightwave Technology 29, 2358-2364 (2011).

[39] A. Mecozzi, et al. "Analysis of intrachannel nonlinear effects in highly dispersed optical pulse transmission," IEEE Photon. Technol. Lett., vol. 12, no. 4, pp. 392-394, 2000.

[40] P. J. Winzer, "Advanced Optical Modulation Formats",‖ Proceedings of the IEEE, vol. 94, no. 5, pp. 952-985, May 2006.

[41] S. Jansen et al., "16x52.5-Gb/s, 50-GHz spaced, POLMUX-CO-OFDM transmission over 4,160 km of SSMF enabled by MIMO processing", Post-Deadline Papers, ECOC, 2007.

[42] A. N. Kolmogorov, "Interpolation and Extrapolation of Stationary Random Sequences", 1941, the USSR Science Academic Bulletin.

[43] N. Wiener, "The Extrapolation, Interpolation and Smoothing of Stationary Time Series", OSRD 370, MIT, 1942.

[44] B. Widrow, et al., "The complex LMS algorithm," in Proceedings of the IEEE, vol. 63, no. 4, April 1975.

[45] A. J. van der Veen, et al., "An analytical constant modulus algorithm," in IEEE Transactions on Signal Processing, vol. 44, no. 5, May 1996.

[46] "IEEE Guide for Improving the Lightning Performance of Electric Power Overhead Distribution Lines", IEEE Standard 1410-1997 Report, 1997.

[47] Edward Collett, "Polarized Light: Fundamentals and Applications", (Optical Engineering, Vol 36), 1st Edition. ISBN-10: 0824787293.

[48] Thomas Brugière et al., "Polarization Activity Monitoring of an Aerial Fiber Link in a Live Network", OFC, Anaheim, CA, pp. 1-3, 2016.

[49] L. E. Nelson, et al., "Field Measurements of Polarization Transients on a Long-Haul Terrestrial Link," in IEEE Photonic Society 24th Annual Meeting, 2011, pp. 833–834.

[50] D. Charlton, et al., "Field measurements of SOP transients in OPGW, with time and location correlation to lightning strikes", Opt. Express 25, 9689-9696 (2017)

[51] S. Pietralunga, et al., "Fast Polarization Effects in Optical Aerial Cables Caused by Lightning and Impulse Current", Photonics Technology Letters, IEEE. 16. 2583 – 2585, 2004.

[52] F. Pittalà, et al., "Laboratory Measurements of SOP Transients due to Lightning Strikes on OPGW Cables", OFC, M4B.5, 2018.

[53] J. Wuttke et al., "Polarization oscillations in aerial fiber caused by wind and power-line current," IEEE Photon. Technol. Lett., vol. 15, pp. 882-884, 2003.

[54] Y. Namihira et al, "Dynamic Polarization Fluctuation Characteristics of Optical Fiber Submarine Cables Under Various Environmental Conditions", Journal of Lightwave Technology, Vol.6, No.5, pp.728-738, May 1988

[55] Y. Namihira et al, "Real-time measurements of Polarization Fluctuation in an Optical Fiber Submarine in a Deep-Sea using Electrooptic LiNbO3 Device", Journal of Lightwave Technology, Vol.6, No.5, pp.728-738, May 1988.

[56] M. Karlsson, et al., “Long-Term Measurement of PMD and Polarization Drift in Installed Fibers”, Journal of Lightwave Technology, Vol. 18, No. 7, pp.941-951, July 2000.

[57] T. Geisler and P. Kristensen, “Polarization properties of DCMs: Thermal variations,” in Proc. OFC Conf., San Diego, CA, USA, Mar. 2009, pp. 1–3, paper OWD3.

[58] T. Geisler, et al., "Reduction of fast SOP changes in DSCMs under influence of shock and vibrations," 2010 Conference on Optical Fiber Communication, San Diego, CA, 2010, pp. 1-3.

[59] Han Sun, et al., “System Penalty in Coherent Receiver Considering Distributed PMD, PDL, and ASE”, IEEE Photonics Technology Letters, Vol. 25, No. 9, 2013.

[60] T. Pfau, et al., “32-krad/s polarization and 3-dB PDL tracking in a real-time digital coherent polarization-multiplexed QPSK receiver,” presented at the Proc. IEEE/LEOS Summer Topical Meetings, Acapulco, Mexico, Jul. 21–23, 2008, Paper MC2.4.

[61] Q. Guo, et al., “Studies on effects of feedback delay on the convergence performance of adaptive time-domain equalizers for fiber dispersive channels”, Optical Engineering 55(4):046110 · April 2016.

[62] P. K. Meher, et al., "Low adaptation-delay LMS adaptive filter part-I: Introducing a novel multiplication cell," 2011 IEEE 54th International Midwest Symposium on Circuits and Systems (MWSCAS), Seoul, 2011, pp. 1-4.

[63]. P. K. Meher, et al., “Low adaptation-delay LMS adaptive filter part-II: An optimized architecture,” in Proc. IEEE Int. Midwest Symp. Circuits Syst., Aug. 2011, pp. 1–4.

[64] Yiqiao Feng, Linqian Li, Jiachuan Lin, Hengying Xu, Wenbo Zhang, Xianfeng Tang, Lixia Xi, and Xiaoguang Zhang, "Joint tracking and equalization scheme for multi-polarization effects in coherent optical communication systems," Opt. Express 24, 25491-25501 (2016)

[65] M. Noelle, et al., "Performance of CAZAC Training Sequences in Data-Aided Single-Carrier Optical Transmission Systems," Photonic Networks; 16. ITG Symposium, Leipzig, Germany, 2015, pp. 1-6.

[66] F. Pittalà, et al., "Training-Aided Frequency-Domain Channel Estimation and Equalization for Single-Carrier Coherent Optical Transmission Systems," in Journal of Lightwave Technology, vol. 32, no. 24, pp. 4849-4863, 2014.

[67] M. Kuschnerov et al., "Data-Aided Versus Blind Single-Carrier Coherent Receivers," in IEEE Photonics Journal, vol. 2, no. 3, pp. 387-403, June 2010.

[68] O. Gerstel, et al., "Elastic optical networking: new dawn for the optical layer", IEEE Communications Magazine, vol. 50, no. 2, pp. s12-s20, 2012.

[69] A. Mitra, et al., "Effect of link margin and frequency granularity on the performance of a Flexgrid

optical network," 39th European Conference and Exhibition on Optical Communication. 2013.

[70] F. Buchali, et al., “Implementation of 64QAM at 42.66 GBaud Using 1.5 Samples per Symbol DAC and Demonstration of up to 300 km Fiber Transmission,” in Optical Fiber Communication Conference, 2014, paper M2A.1.

[71] A. Souari, et al., "Performance evaluation of time and frequency domain equalizers", Canadian Conference for Electrical and Computer Engineering, Toronto, ON, 2014, pp. 1-6.

[72] A. Mecozzi, et al., "The statistics of polarization-dependent loss in optical communication systems," in IEEE Photonics Technology Letters, vol. 14, no. 3, pp. 313-315, 2002.

[73] X. Zhou, C. Xie, Enabling Technologies for High Spectral-Efficiency Coherent Optical Communication Networks, Wiley, pp. 1-648, 2016.

[74] T. Kimijima, et al., "A pipelined architecture for DLMS algorithm considering both hardware complexity and output latency," 9th European Signal Processing Conference, Rhodes, 1998, pp. 1-4.

[75] E. P. da Silva, et al., "Widely Linear Equalization for IQ Imbalance and Skew Compensation in Optical Coherent Receivers", *in* Journal of Lightwave Technology, vol. 34, no. 15, pp. 3577-3586, Aug.1, 1 2016.

[76] M. Paskov, et al., "Blind Equalization of Receiver In-Phase/Quadrature Skew in the Presence of Nyquist Filtering," in IEEE Photonics Technology Letters, vol. 25, no. 24, pp. 2446-2449, Dec.15, 2013.

[77] T. A. Strasser, et al., "Wavelength-Selective Switches for ROADM Applications," in IEEE Journal of Selected Topics in Quantum Electronics, vol. 16, no. 5, pp. 1150-1157, Sept.-Oct. 2010.

[78] C. C. Chan, “Optical Performance Monitoring: Advanced Techniques for Next-Generation Photonic Networks”, New York, NY, USA: Elsevier, 2010.

[79] M. Zamani, et al., "PDL compensation using whitening matrix in polarization division multiplexed coherent optical transmission," OFC, Anaheim, CA, 2013.

[80] F. N. Hauske, et al., "Impact of optical channel distortions to digital timing recovery in digital coherent transmission systems," 12th International Conference on Transparent Optical Networks, Munich, pp. 1-4, 2010.

[81] Mark Hawryluck, “Automatic gain control in a coherent optical receiver”, US Patent 7936999 B1.

[82] Simon Haykin, Adaptive Filter Theory, fourth edition, Prentice Hall, 2002.

[83] G. Long et al., “The LMS algorithm with delayed coefficient adaptation”, IEEE Transactions on Acoustic, Vol, 37, no. 9, 1971.

[84] O. Ishida, et al., "Power efficient DSP implementation for 100G-and-beyond multi-haul coherent fiber-optic communications," 2016 Optical Fiber Communications Conference, Anaheim, CA, 2016, pp. 1-3.

[85] Socionext, “100g to 400g adc and dac for ultra-high-speed optical networks,” available at http://socionextus.com/products/networking-asic/adc-dac/. Accessed 11/August 2018.

[86] C. Schmidt et al., “Digital-to-analog converters for high-speed optical communications using frequency interleaving: Impairments and characteristics”, Optics Express, 2018. 26. 6758. 10.1364/OE.26.006758.

[87] W. C. Ng, et al., "Reduction of MIMO-FIR taps via SOP-estimation in stokes space for 100 Gbps short reach applications", ECOC, Cannes, 2014, pp. 1-3.

[88] R. H. Kwong, et al, "A variable step size LMS algorithm", in IEEE Transactions on Signal Processing, vol. 40, no. 7, pp. 1633-1642, Jul 1992.

[89] R. Harris, et al., "A variable step (VS) adaptive filter algorithm", IEEE Transactions on Acoustics, Speech, and Signal Processing, vol. 34, no. 2, pp. 309-316, April 1986.

[90] Cisco Transport Planner DWDM Operations Guide Release 9.0, Cisco Systems. Online Documentation (2015).

[91] A. Ghosh, “Fundamentals of LTE”, Prentice Hall Press, Upper Saddle River, NJ, 2010

[92] E. Eweda, “Comparison of RLS, LMS, and Sign Algorithms for Tracking Randomly Time-Varying Channels”, IEEE Transactions on Signal Processing, VOL. 42, no. 2,1994.

[93] P. C. Wei, et al., "Comparative tracking performance of the LMS and RLS algorithms for chirped narrowband signal recovery," in IEEE Transactions on Signal Processing, vol. 50, no. 7, pp. 1602-1609, Jul 2002.

[94] O. Macchi, et al., "Steady-state superiority of LMS over LS for time-varying line enhancer in noisy environment", *in* IEE Proceedings F - Radar and Signal Processing, vol. 138, no. 4, pp. 354-360, Aug. 1991.

[95] Pei Lin, et al., "On the tracking performance of LMS and RLS algorithms in an adaptive MMSE CDMA receiver", ACTW, Brisbane, Qld., 2005, pp. 175-178.

[96] K. F. Wan, et al., "A fast convergence median LMS algorithm", ISCAS, London, 1994, pp. 377-380 vol. 2.

[97] F. Pittalà et al., "PDL Monitoring based on the Eigenvalues Spread of a Data-Aided Zero-Forcing Frequency Domain Equalizer", SPPCOM Advanced Photonics Congress, OSA Technical Digest, paper SpTh2B.5, 2012.

[98] Ali H. Sayed, Fundamentals of Adaptive Filtering, 1st Edition (pg. 383).

[99] I. Parvez, et al., “A Survey on Low Latency Towards 5G: RAN, Core Network and Caching Solutions”, submitted to IEEE Communications Surveys and Tutorials, 2017.

[100] Xiang Zhou and Martin Birk, "Performance Comparison of an 80-km-per-Span EDFA System and a 160-km Hut-Skipped All-Raman System Over Standard Single-Mode Fiber," J. Lightwave Technol. 24, 1218- (2006)

[101] G. Baxter, S. Frisken, D. Abakoumov, H. Zhou, I. Clarke, A. Bartos, and S. Poole, “Highly programmable wavelength selective switch based on liquid crystal on silicon switching elements,” in *Optical Fiber Communication Conf. (OFC)*, 2006, paper OTuF2.

[102] D. M. Marom, D. T. Neilson, D. S. Greywall, C. S. Pai, N. R. Basavanhally, V. A. Aksyuk, D. O. López, F. Pardo, M. E. Simon, Y. Low, P. Kolodner, and C. A. Bolle, “Wavelength-selective 1 × *K* switches using free-space optics and MEMS micromirrors: Theory, design, and implementation,” J. Lightwave Technol., vol. 23, no. 4, pp. 1620–1630, 2005.

[103] M. Filer and S. Tibuleac, "N-degree ROADM Architecture Comparison: Broadcast-and-Select Versus Route-and-Select in 120 Gb/s DP-QPSK Transmission Systems," Conference on Optical Fiber Communication, San Francisco, CA, 2014, Th1I.2.

[104] L. Zong, J. Veselka, H. Sardesai, M. Frankel, “Influence of filter shape and bandwidth on 44 Gb/s DQPSK systems,” OFC 2009.

[105] A. Ghazisaeidi *et al.*, “Impact of tight optical filtering on the performance of 28 Gbaud nyquist-WDM PDM-8QAM over 37.5 GHz grid,” in *Proc. Conf. Commun. Nat. Fiber Opt. Eng.,* 2013, Paper OTu3B.6

[106] S. Tibuleac, "ROADM network design issues," 2009 Conference on Optical Fiber Communication - incudes post deadline papers, San Diego, CA, 2009, pp. 1-48.

[107] ROADMs & Wavelength Management, 1x9 / 1x20 Flexgrid Wavelength Selective Switch (avaiblable at https://www.finisar.com/roadms-wavelength-management/10wsaaxxfll)... Accessed 11/August/2018.

[108] D. J. Krause, et al., "Pre-compensation for Narrow Optical Filtering of 10-Gb/s Intensity Modulated Signals," in IEEE Photonics Technology Letters, vol. 20, no. 9, pp. 706-708, May1, 2008.

[109] Y. Jiang, X. Tang, J. C. Cartledge and K. Roberts, "Pre-compensation for the effects of cascaded optical filtering on 10 Gsymbol/s DPSK and DQPSK signals," 2009 35th European Conference on Optical Communication, Vienna, 2009, pp. 1-2.

[110] J. Pan and S Tibuleac, “Real-time ROADM filtering penalty characterization and generalized precompensation for flexible grid networks,” *IEEE Photon. J.*, vol. 9, no. 3, Jun. 2017, Art. no. 7202210.

[111] J. Pan and S. Tibuleac, “Real-time pre-compensation of ROADM filtering using a generalized pre-emphasis filter,” in *Proc. IEEE Photon. Conf.*, 2016, pp. 548–549.

[112] T. Foggi, et al., "Overcoming filtering penalties in flexi-grid long-haul optical systems," 2015 IEEE International Conference on Communications (ICC), London, 2015, pp. 5168-5173.

[113] T. Rahman et al., "On the Mitigation of Optical Filtering Penalties Originating from ROADM Cascade," in IEEE Photonics Technology Letters, vol. 26, no. 2, pp. 154-157, Jan.15, 2014.

[114] A. H. Gnauck, L. D. Garrett, Y. Danziger, U. Levy and M. Tur, "Dispersion and dispersion-slope compensation of NZDSF over the entire C band using higher-order-mode fibre," in Electronics Letters, vol. 36, no. 23, pp. 1946-1947, 9 Nov. 2000.

[115] W. Idler, F. Buchali, L. Schmalen, K. Schuh, and H. Buelow, “Hybrid Modulation formats outperforming 16QAM and 8QAM in transmission distance and filtering with cascaded WSS,” in *Proc. Conf. Opt. Fiber Commun.*, 2015, Paper M3G.4.

[116] R. -. Braun, D. Fritzsche, A. Ehrhardt, L. Schürer, P. Wagner, M. Schneiders, S. Vorbeck, C. Xie, Z. Zhao, W. Wan, P. Liu, Q. Zhou, and P. Hostalka, "112 GBit/s PDM-CSRZ-DQPSK Field Trial Over 1730 km Deployed DWDM-Link," in Optical Transmission Systems, Switching, and Subsystems VIII, Y. Su, E. Ciaramella, X. Liu, and N. Wada, eds., Vol. 7988 of Proceedings of SPIE-OSA (Optical Society of America, 2010), paper 79880G.

[117] P. L. Ventre et al., "Deploying SDN in GÉANT production network," 2017 IEEE Conference on Network Function Virtualization and Software Defined Networks (NFV-SDN), Berlin, 2017, pp. 1-2.

[118] Yongcheng Li, Li Gao, Gangxiang Shen, and Limei Peng, "Impact of ROADM Colorless, Directionless, and Contentionless (CDC) Features on Optical Network Performance [Invited]," J. Opt. Commun. Netw. 4, B58-B67 (2012)

[119] B. Pal, L. Zong, E. Burmeister and H. P. Sardesai, "Statistical method for ROADM cascade penalty," 2010 Conference on Optical Fiber Communication (OFC/NFOEC), collocated National Fiber Optic Engineers Conference, San Diego, CA, 2010, pp. 1-3.

[120] Yohei Sakamaki, Takeshi Kawai, Tetsuro Komukai, Mitsunori Fukutoku, Tomoyoshi Kataoka, Toshio Watanabe, and Yuzo Ishii, "Experimental demonstration of multi-degree colorless, directionless, contentionless ROADM for 127-Gbit/s PDM-QPSK transmission system," Opt. Express 19, B1-B11 (2011)

[121] L. Chen, X. Tang, A. Sanyal, Y. Yoon, J. Cong and N. Sun, "A 10.5-b ENOB 645 nW 100kS/s SAR ADC with statistical estimation-based noise reduction," 2015 IEEE Custom Integrated Circuits Conference (CICC), San Jose, CA, 2015, pp. 1-4.

[122] M. Y. S. Sowailem et al., "770-Gb/s PDM-32QAM Coherent Transmission Using InP Dual Polarization IQ Modulator," in IEEE Photonics Technology Letters, vol. 29, no. 5, pp. 442-445, 1 March1,

2017.

[123] I. Roudas, N. Antoniades, T. Otani, T. E. Stern, R. E. Wagner and D. Q. Chowdhury, "Accurate modeling of optical multiplexer/demultiplexer concatenation in transparent multiwavelength optical networks," in Journal of Lightwave Technology, vol. 20, no. 6, pp. 921-936, June 2002.

[124] Cibby Pulikkaseril, et al, "Spectral modeling of channel band shapes in wavelength selective switches," Opt. Express 19, 8458-8470, 2011.
[125] Y. Fan, X. Chen, W. Zhou, X. Zhou and H. Zhu, "The Comparison of CMA and LMS Equalization Algorithms in Optical Coherent Receivers," 2010 6th International Conference on Wireless Communications Networking and Mobile Computing (WiCOM), Chengdu, 2010, pp. 1-4.

[126] C. Xie et al., "Increasing Polarization-Mode Dispersion Tolerance of Coherent Receivers by Joint Optimization of Chromatic Dispersion and Butterfly Equalizers," in Advanced Photonics 2013, SPM2E.5.

[127] A. Viterbi, "Nonlinear estimation of PSK-modulated carrier phase with application to burst digital transmission," in IEEE Transactions on Information Theory, vol. 29, no. 4, pp. 543-551, July 1983.

[128] T. Mizuochi et al., "Forward error correction based on block turbo code with 3-bit soft decision for 10-Gb/s optical communication systems," in IEEE Journal of Selected Topics in Quantum Electronics, vol. 10, no. 2, pp. 376-386, March-April 2004.

[129] W. Yang et al., "A 3-V 340-mW 14-b 75-Msample/s CMOS ADC with 85-dB SFDR at Nyquist input," *IEEE J. of Solid-State Circuits,* Dec. 2001.

[130] “Equalizing Techniques Flatten DAC Frequency Response”, Maxim Integrated Application Note (accessed August 2018, available at https://www.maximintegrated.com/en/app-notes/index.mvp/id/3853)

[131] Brent L. Bachim and Thomas K. Gaylord, "Polarization-dependent loss and birefringence in long-period fiber gratings," Appl. Opt. 42, 6816-6823 (2003)

[132] Sorin Tibuleac and Mark Filer, "Transmission Impairments in DWDM Networks With Reconfigurable Optical Add-Drop Multiplexers," J. Lightwave Technol. 28, 557-568 (2010)

[133] Saeed V. Vaseghi, "Advanced Digital Signal Processing and Noise Reduction”, Second Adition, ISBN: 978-0-470-09495-2.

[134] Gengchen Liu, Kaiqi Zhang, Rui Zhang, Roberto Proietti, Hongbo Lu, and S. J. Ben Yoo, "Demonstration of a carrier frequency offset estimator for 16-/32-QAM coherent receivers: a hardware perspective," Opt. Express 26, 4853-4862 (2018)

[135] H. Wymeersch and P. Johannisson, "Maximum-Likelihood-Based Blind Dispersion Estimation for Coherent Optical Communication," in Journal of Lightwave Technology, vol. 30, no. 18, pp. 2976-2982, Sept.15, 2012.

[136] A. Mecozzi and M. Shtaif, “The Statistics of Polarization-Dependent Loss in Optical Communication Systems,” IEEE Photonics Technol. Lett. 14, 313–315 (2002).

[137] P. Delesques, E. Awwad, S. Mumtaz, G. Froc, P. Ciblat, Y. Jaou¨en, G. Rekaya, and C. Ware, “Mitigation of PDL in coherent optical communications: How close to the fundamental limit?,” in proc. of ECOC’12, paper P4.13.

[138] J. Tuqan, "Global optimization of orthogonal FIR Tx and Rx filters for data transmission over noisy channels," Conference Record of the Thirty-Third Asilomar Conference on Signals, Systems, and Computers (Cat. No.CH37020), Pacific Grove, CA, USA, 1999, pp. 202-206 vol.1.

[139] WaveShaper User Manual, Finisar Corporation, Sunnyvale, CA. 2016.

[140] A. Fraine, O. Minaeva, D. S. Simon, R. Egorov, and A. V. Sergienko, "Evaluation of polarization mode dispersion in a telecommunication wavelength selective switch using quantum interferometry," Opt. Express 20, 2025-2033 (2012)

[141] Viavi MAP-200/mHROSA-A1, data sheet, available at: https://www.viavisolutions.com/de-de/literature/mhrosa-a1-map-200-integrated-multi-wavelength-wavemeter-and-high-resolution-osa-data-sheets-en.pdf , Accessed: 14/August/2018.

[142] O. Bertran-Pardo, T. Zami, B. Lavigne and M. Le Monnier, "Spectral engineering technique to mitigate 37.5-GHz filter-cascade penalty with real-time 32-GBaud PDM-16QAM," 2015 Optical Fiber Communications Conference and Exhibition (OFC), Los Angeles, CA, 2015, pp. 1-3.

[143] Agilent Technology, “Measuring Polarization Dependent Loss of Passive Optical Components”, Application Note .Available at: https://pdfs.semanticscholar.org/9435/014db3b8af48acffc3d1188006a427794573.pdf. Accessed on 12/August/2018.

[144] Viavi MAP-200/PCX-1, data sheet. available at https://www.viavisolutions.com/pt-br/literature/map-200-polarization-scrambler-controller-data-sheet-en.pdf. Accessed on 12/August/2018.

[145] P. Dong, L. Chen, and Y.-K. Chen, “High-speed low-voltage single-drive push-pull silicon Mach-Zehnder modulators,” Opt. Express 20, 6163–6169 (2012).

[146] D. Patel et al., “Design, analysis, and transmission system performance of a 41 GHz silicon photonic modulator,” Opt. Express 23, 14263-14287 (2015).

[147] A. Samani et al., “A Low-Voltage 35-GHz Silicon Photonic Modulator-Enabled 112-Gb/s Transmission System,” in IEEE Photon. J. 7, 3 (2015).

[148] X. Tu et al., “Silicon optical modulator with shield coplanar waveguide electrodes,” Opt. Express 22,

23724–23731 (2014).

[149] S. Frisken, et al., “Flexible and Grid-less Wavelength Selective Switch using LCO S Technology”, OTuM3, OFC, 2011.

[150] ITU G.694.1, “Spectral grids for WDM applications: DWDM frequency grid”

[151] Y. Kai et al., “130-Gbps DMT Transmission using Silicon Mach-Zehnder Modulator with Chirp Control at 1.55-um,” OFC 2015, Th4A.1.

[152] M. Traverso, “25GBaud PAM-4 Error Free Transmission over both Single Mode Fiber and Multimode Fiber in a QSFP form factor based on Silicon Photonics,” OFC 2015, Th5B.3.

[153] C. Doerr et al., “Single-chip silicon photonics 100-Gb/s coherent transceiver,” OFC 2014, Th5C.1.

[154] M. Chagnon et al., “Experimental parametric study of a silicon photonic modulator enabled 112-Gbit/s PAM transmission system with a DAC and ADC”, J. lightwave technol., vol.33, no.7, p.1380, (2014).

[155] C. E. Png, "Silicon-on-insulator phase modulators," PhD thesis, University of Surrey, 2004.

[156] S. Manipatruni, et al., "High Speed Carrier Injection 18 Gb/s Silicon Micro-ring Electro-optic Modulator," in Lasers and Electro-Optics Society, 2007. LEOS 2007. The 20th Annual Meeting of the IEEE, 2007, pp. 537-538.

[157] J. Teng, et al., "A thermal Silicon on-insulator ring resonators by overlaying a polymer cladding on narrowed waveguides," Opt. Express, vol. 17, pp. 14627 - 14633, 2009.

[158] J. Tabares, A. Napoli, V. Polo, S. Calabrò, B. Sommerkorn-Krombholz, B. Spinnler, and J. Prat, "Digital Pre-emphasis for 10Gb/s with Low-cost Directly Phase-Modulated Lasers for PONs," in *Advanced Photonics 2018 (BGPP, IPR, NP, NOMA, Sensors, Networks, SPPCom, SOF)*, OSA Technical Digest (online) (Optical Society of America, 2018), paper SpTh3G.2.

[159] G. Khanna, et al., "Joint Adaptive Pre-Compensation of Transmitter I/Q Skew and Frequency Response for High Order Modulation Formats and High Baud Rates," in **Optical Fiber Communication Conference, 2015***,* paper M2G.4.

[160] A. Yekani, et al., "Experimental comparison of PAM vs. DMT using an O-band silicon photonic modulator at different propagation distances," 2015 European Conference on Optical Communication (ECOC), Valencia, 2015, pp. 1-3.

[161] Mestdagh, D., Spruyt, P., “A method to reduce the probability of clipping in DMT-based transceivers,” IEEE Trans. On Comm., Vol.44, No.10, pp. 1234-1238, 1996.

[162] T. Jiang, et al., “An Overview: Peak to Average Power Ratio Reduction Techniques for OFDM Signals,” IEEE Transactions on Broadcasting, Vol. 54, Issue: 2, pp. 257-268, 2008

[163] M. Park, “PAPR Reduction in OFDM Transmission Using Hadamard Transform”, IEEE International Conference on Communications, Vol. 1, pp. 430-433, 2000

[164] Arne Josten, et al., “Digital Post-Distortion for Cost-Efficient Driverless Optical Transmitter”s, Advanced Photonics Congress, SpTu4G.3, 2018

[165] D Patel, et al., “Frequency response of dual-drive silicon photonic modulators with coupling between electrodes”, Optics express 26 (7), 8904-8915

[166] “Implementation Agreement for CFP2-Analogue Coherent Optics Module”, Optical Inter-Networking Forum, IA # OIF-CFP2-ACO-01.0
Published January 2016.

[167] F. Lipscomb**,** “What Is 400ZR and Why Is It Important?”, **November 2017**, available at https://www.neophotonics.com/what-is-400-zr/. Accessed on 14/August/2018.

[168] T. Okoshi and K. Kikuchi, Coherent Optical Communication Systems. Tokyo, Japan: KTK Scientific Publisher, 1988, ch. 1.

[169] N. Ben-Hamida et al., "Clock recovery for a 40 Gb/s QPSK optical receiver," 16th IEEE International Conference on Electronics, Circuits and Systems**,** 2009, pp. 695-698.

[170] K. Schuh et al**.,** "100 GSa/s BiCMOS DAC Supporting 400 Gb/s Dual Channel Transmission," 42nd European Conference on Optical Communication, Dusseldorf, Germany, 2016, pp. 1-3.

[171] N. Stojanovic, et al., "Feed-forward and feedback timing recovery for Nyquist and faster than Nyquist systems," OFC 2014, San Francisco, CA, 2014.

[172] V. S. Grigoryan, et al., "Calculation of Timing and Amplitude Jitter in Dispersion-Managed Optical Fiber Communications Using Linearization," J. Lightwave Technol. 17, 1347- (1999)

[173] M. Eiselt, et al., "Contribution of timing jitter and amplitude distortion to XPM system penalty in WDM systems," in IEEE Photonics Technology Letters, vol. 11, no. 6, pp. 748-750, June 1999.

[174] M. Eiselt, "The impact of non-linear fiber effects on fiber choice for ultimate transmission capacity", Optical Fiber Communication Conference 2000, vol. 1, pp. 58-60 vol.1, 2000.

[175] S. Oda et al., "Interplay between local oscillator phase noise and electrical chromatic dispersion compensation in digital coherent transmission system," 36th European Conference and Exhibition on Optical Communication, Torino, 2010, pp. 1-3.

[176] Leeson, D. B. "A Simple Model of Feedback Oscillator Noise Spectrum", Proceedings of the IEEE, 54 (2): 329–330, 1996

[177] A. Mehrotra, "Noise analysis of phase-locked loops", IEEE Transactions on Circuits and Systems I, vol. 49, no. 9, pp. 1309-1316, Sep 2002.

[178] Lingchen Huang, Dawei Wang, Alan Pak Tao Lau, Chao Lu, and Sailing He, "Performance analysis of blind timing phase estimators for digital coherent receivers," Opt. Express 22, 6749-6763 (2014)

[179] D. Wang, K. Lu, P. O. Rasmussen and Z. Yang, "Comparative study of low-pass filter and phase-locked loop type speed filters for sensorless control of AC drives," in CES Transactions on Electrical Machines and Systems**,** vol. 1, no. 2, pp. 207-215, 2017.

[180] Yi Cai, et al., "Jitter testing for gigabit serial communication transceivers," in IEEE Design & Test of Computers, vol. 19, no. 1, pp. 66-74, Jan/Feb 2002.

[181] Mark Horowitz, Chih-Kong Ken Yang, and Stefanos Sidiropoulos, “High-speed electrical signaling: overview and limitations”. IEEE Micro, 18(1):21{24, January-February 1998.

[182] Yueming Jiang and A. Piovaccari, "A compact phase interpolator for 3.125G Serdes application," Southwest Symposium on Mixed-Signal Design, 2003., 2003, pp. 249-252.

[183] Sidiropoulos, S. and Horowitz, M., "A Semi-Digital Dual Delay Locked Loop," IEEE Journal of Solid-State Circuits, V. 32, No. 11, November 1997.

[184] Enam, S. and Abidi, A. "NMOS IC's for Clock and Data Regeneration in Gigabit-per-Second Optical-Fiber Receivers," IEEE Journal of Solid State Circuits, vol. 27, no. 12, Dec. 1992.

[185] Taesung Kim, et al., “Phase Interpolator Using Delay Locked Loop”, SSMSD, 2003

[186] L. Rodoni, G. von Buren, A. Huber, M. Schmatz, H. Jackel, "A 5.75 to 44 Gb/s quarter rate CDR with data rate selection in 90 nm bulk CMOS", IEEE J. Solid-State Circuits, vol. 44, no. 7, pp. 1927-1941, Jul. 2009.

[187] Y. Jiang, A. Piovaccan, “A compact phase interpolator for 3.1256G Serdes application”, Proceedings of Southwest Symposium Mixed-Signal Design, 249-252, 2003.

[188] George Souliotis, et al., “Phase Interpolator with Improved Linearity”, Circuits, Systems, and Signal Processing Volume 35 Issue 2, Pages 367-383, 2016.

[189] A. Joshi and M. Sarkar, "Nonlinearity Estimation for Compensation of Phase Interpolator in Bang–Bang CDRs," in IEEE Transactions on Very Large-Scale Integration (VLSI) Systems, vol. 25, no. 1, pp. 388-392, Jan. 2017.

[190] G. R. Gangasani et al**.,** "A 16-Gb/s Backplane Transceiver With 12-Tap Current Integrating DFE and Dynamic Adaptation of Voltage Offset and Timing Drifts in 45-nm SOI CMOS Technology," in IEEE Journal of Solid-State Circuits, vol. 47, no. 8, pp. 1828-1841, Aug. 2012.

[191] L. Rodoni, G. von Buren, A. Huber, M. Schmatz and H. Jackel, "A 5.75 to 44 Gb/s Quarter Rate CDR With Data Rate Selection in 90 nm Bulk CMOS," in IEEE Journal of Solid-State Circuits, vol. 44, no. 7, pp. 1927-1941, July 2009.

[192] R.G. Lyons, "Sum of Two Sinusoids", For Free Publication by Iowegian, 2011.

[193] Maxim Kuschnerov, "100G at the dawn of white box DSPs", available at https://www.fibre-systems.com/news/analysis-opinion/100g-dawn-white-box-dsps. Accessed on 11/August/2018.

[194] Logan Armendone-Mowbray, "400G-ZR Standard Revs Up Optical Network Speeds". Available at https://tinyurl.com/yac4kxn6. Accessed on 11/August/2018.

[195] Mark Enright, et al., "Open Cables and Integration with Terrestrial Networks", SubOptics 2016, available at https://tinyurl.com/yc3syb7p

[196] Michael Schnecker, "Jitter Measurements in Serial Data Signals", LeCroy Corporation Whitepaper.

[197] Y. Wu, et al., "Built-in functional tests for fast validation of a 40Gbps coherent optical receiver SoC ASIC," IEEE International SOC Conference, Newport Beach, CA, 2008, pp. 55-58.

[198] Ik-Hwan Kim, "An On-Chip Jitter Tolerance Test Circuit for Mobile and Video Interfaces", IEEE International Conference on Consumer Electronics-Asia, 2016.

[199] K. A Jenkins, "On-Chip Circuit for Measuring Period Jitter and Skew of Clock Distribution Networks", IEEE Custom Intergrated Circuits Conference (CICC), 2007.

[200] R. DiCecco, R. Pahuta, C. Holdenried and S. Sadr, "Test considerations for jitter tolerance of wireline receivers," IEEE 27th Canadian Conference on Electrical and Computer Engineering (CCECE), Toronto, ON, 2014, pp. 1-5.

[201] J. M. Cazeaux, M. Omana and C. Metra, "Novel on-chip circuit for jitter testing in high-speed PLLs," in IEEE Transactions on Instrumentation and Measurement, vol. 54, no. 5, pp. 1779-1788, Oct. 2005.

[202] K. A Jenkins, "On-Chip Circuit for Measuring Period Jitter and Skew of Clock Distribution Networks", IEEE Custom Intergrated Circuits Conference (CICC), 2007.

[203] MJ Park, "A Built-In Self-Test Circuit for Jitter Tolerance Measurement in High-Speed Wireline Receivers", International Test Conference, 2014.

[204] G. W. Roberts et al., "Mixed-Signal Production Test: A Measurement Principle Perspective," in IEEE Design & Test of Computers, vol. 26, no. 5, pp. 48-62, Sept.-Oct. 2009.

[205] T. Endo and J. Yokota, "Generation of White Noise by Using Chaos in Practical Phase-Locked Loop Integrated Circuit Module," Circuits and Systems, 2007. ISCAS 2007. IEEE International Symposium on, New Orleans, LA, 2007, pp. 201-204. doi: 10.1109/ISCAS.2007.378311

[206] Dennis Peterich, et al., "Fibre Channel - Methodologies for Jitter and Signal Quality Specification-MJSQ"., T11.2 / Project 1316-DT/ Rev 12.1, December 7, 2003.

[207] Specification report, “Telcordia’s SONET”, GR-253-CORE, Issue 3, September 2000.

[208] Feng Tan, et al., "Analysis of Phase Noise and Timing Jitter in Crystal Oscillator," International Conference Communications, Circuits and Systems, pp.1103-1106, 11-13 July 2007.

[209] Taesung Kim and Beomsup Kim, "Phase interpolator using delay locked loop [multiphase clock generation]," Southwest Symposium on Mixed-Signal Design, Las Vegas, NV, USA, 2003, pp. 76-80.

[210] P. K. Hanumolu, et al, "Jitter in high-speed serial and parallel links," Circuits and Systems, 2004. ISCAS '04. Proceedings of the 2004 International Symposium on, 2004

[211] J. Liang, A. Sheikholeslami, H. Tamura and H. Yamaguchi, "Jitter injection for on-chip jitter measurement in PI-based CDRs," IEEE Custom Integrated Circuits Conference (CICC), Austin, TX, 2017, pp. 1-4.